

UPPSALA
UNIVERSITET

Digital Comprehensive Summaries of Uppsala Dissertations from the Faculty of Science and Technology 1434

Searches for Higgs bosons with hadronically decaying τ-leptons

Using Grid and Cloud computing techniques

HENRIK ÖHMAN



ACTA
UNIVERSITATIS
UPSALIENSIS
UPPSALA
2016

ISSN 1651-6214
ISBN 978-91-554-9706-4
urn:nbn:se:uu:diva-304291

Dissertation presented at Uppsala University to be publicly examined in Polhemsalen, 10134, Ångströmlaboratoriet, Lägerhyddsvägen 1, Uppsala, Monday, 21 November 2016 at 20:19 for the degree of Doctor of Philosophy. The examination will be conducted in English. Faculty examiner: Professor Paula Eerola (Helsinki Institute of Physics (HIP)).

Abstract
Öhman, H. 2016. Searches for Higgs bosons with hadronically decaying τ-leptons. Using Grid and Cloud computing techniques. *Digital Comprehensive Summaries of Uppsala Dissertations from the Faculty of Science and Technology* 1434. 111 pp. Uppsala: Acta Universitatis Upsaliensis. ISBN 978-91-554-9706-4.

This thesis describes a measurement of the Standard Model Higgs boson coupling to fermions in decays to two τ-leptons, a search for charged Higgs bosons in decays to a τ-lepton and a neutrino, as well as the reconstruction, identification and triggering of hadronically decaying τ-leptons. The data considered are collected by the ATLAS experiment at the Large Hadron Collider.

The reconstruction and identification of hadronically decaying τ-leptons in the ATLAS experiment during Run 2 of the Large Hadron Collider are described, and the performance of the τ trigger is measured in events with top–antitop-quark pairs using data from 13 TeV proton–proton collisions, corresponding to an integrated luminosity of 3.2 fb^{-1}, collected in 2015, and 11.5 fb^{-1}, collected in 2016.

Hadronically decaying τ-leptons are of importance to many physical processes involving Higgs bosons. The coupling of the Standard Model Higgs boson to fermions is measured in decays to two τ-leptons using 7 TeV data corresponding to an integrated luminosity of 4.5 fb^{-1}, collected in 2011, and 8 TeV data corresponding to an integrated luminosity of 20.3 fb^{-1}, collected in 2012. The signal strength is measured to be $\mu = 1.4$, corresponding to an excess over the background-only model of 4.5σ.

Charged Higgs bosons are searched for in decays to a τ-lepton and a neutrino, where the τ-lepton decays hadronically. 13 TeV data corresponding to an integrated luminosity of 14.7 fb^{-1}, collected in 2015 and 2016, are used. No excess over the Standard Model background is observed, and the 95 % confidence-level exclusion limits on $\sigma(pp \rightarrow [b]tH^{+}) \times (H^{+} \rightarrow \tau\nu)$ are set to 2.0 pb–8 fb in the range 200–2000 GeV.

Keywords: LHC, ATLAS, Higgs, Charged Higgs, Tau lepton, 2HDM, MSSM

Henrik Öhman, , Department of Physics and Astronomy, High Energy Physics, Box 516, Uppsala University, SE-751 20 Uppsala, Sweden.

© Henrik Öhman 2016

ISSN 1651-6214
ISBN 978-91-554-9706-4
urn:nbn:se:uu:diva-304291 (http://urn.kb.se/resolve?urn=urn:nbn:se:uu:diva-304291)

To Louise, my soulmate
To Lova and Elsa
To Alexandra

List of papers

This thesis is based on the following papers, which are referred to in the text by their Roman numerals.

I Henrik Öhman *et al.*,
Using Puppet to contextualize computing resources for ATLAS analysis on Google Compute Engine,
J. Phys. Conf. Ser. **513** (2014) 032073

II ATLAS Collaboration,
Evidence for the Higgs-boson Yukawa coupling to tau leptons with the ATLAS detector,
JHEP **04** (2015) 117

III ATLAS Collaboration,
Commissioning of the reconstruction of hadronic tau lepton decays in ATLAS using pp collisions at $\sqrt{s} = 13$ *TeV,*
ATL-PHYS-PUB-2015-025

IV ATLAS Collaboration,
Search for charged Higgs bosons produced in association with a top quark and decaying via $H^{\pm} \to \tau\nu$ *using pp collision data recorded at* $\sqrt{s} = 13$ *TeV by the ATLAS detector,*
Phys. Lett. B **759** (2016) 555

V Henrik Öhman,
Reconstruction and identification of hadronically decaying tau leptons with the ATLAS experiment,
PoS(LHCP2016)211

VI Henrik Öhman,
Charged Higgs boson searches in ATLAS and CMS,
PoS(LHCP2016)085

VII ATLAS Collaboration,
Search for charged Higgs bosons in the τ*+jets final state using* $14.7\,fb^{-1}$ *of pp collision data recorded at* $\sqrt{s} = 13$ *TeV with the ATLAS experiment,*
ATLAS-CONF-2016-088

Reprints were made with permission from the publishers.

List of papers not included in this thesis

VIII ATLAS Collaboration,
Evidence for Higgs Boson Decays to the $\tau^+\tau^-$ Final State with the ATLAS Detector,
ATLAS-CONF-2013-108

IX Eric Baussan *et al.*,
A very intense neutrino super beam experiment for leptonic CP violation discovery based on the European spallation source linac,
Nucl. Phys. B **885**, 127 (2014),
arXiv:1309.7022 [hep-ex]

X Sergey Panitkin *et al.*,
ATLAS Cloud R&D,
J. Phys. Conf. Ser. **513** (2014) 062037

XI ATLAS Collaboration,
Evidence for Higgs boson Yukawa couplings in the $H \to \tau\tau$ decay mode with the ATLAS detector,
ATLAS-CONF-2014-061

Contents

1 Introduction 11

2 Theoretical background 13
2.1 The Standard Model 13
2.1.1 The Brout-Englert-Higgs mechanism 15
2.1.2 Higgs boson production and decay 18
2.2 Beyond the Standard Model 19
2.2.1 The Minimal Supersymmetric Standard Model 20
2.2.2 Two-Higgs Doublet Models 21
2.2.3 MSSM benchmark scenarios 22
2.3 Charged Higgs bosons 22
2.3.1 Production of charged Higgs bosons 22
2.3.2 Decays of charged Higgs bosons 24
2.3.3 Charged Higgs boson searches 24

3 CERN and the Large Hadron Collider 27
3.1 CERN 27
3.2 Past accelerators and experiments 27
3.3 The Large Hadron Collider 28
3.4 The LHC experiments 29
3.5 Other experiments at CERN 31

4 The ATLAS experiment 33
4.1 Description of the ATLAS detector 33
4.1.1 Overview 33
4.1.2 Inner detector 35
4.1.3 Calorimeters 38
4.1.4 Muon spectrometer 41
4.1.5 Forward detectors 43
4.1.6 Magnet system 43
4.2 Particle reconstruction and identification 44
4.2.1 Electrons 44
4.2.2 Photons 45
4.2.3 Muons 46
4.2.4 Jets 46
4.2.5 τ-leptons 47
4.2.6 Flavour tagging 47

4.2.7 Overlapping objects ... 48
4.2.8 Missing transverse energy ... 48
4.3 Trigger and data acquisition ... 49
4.3.1 Level-1 trigger ... 49
4.3.2 High-Level Trigger ... 51
4.3.3 Data acquisition ... 52
4.4 Computing and data model ... 52
4.4.1 The LHC computing model ... 52
4.4.2 The ATLAS data model ... 52
4.4.3 ATLAS computing model ... 54
4.4.4 Cloud computing R&D ... 55

5 Reconstruction, identification, and triggering of hadronically decaying τ-leptons ... 57
5.1 Introduction ... 57
5.2 Detection, reconstruction, and identification ... 58
5.2.1 Reconstructing hadronicly decaying τ-leptons ... 58
5.2.2 Identification of hadronically decaying τ-leptons ... 60
5.2.3 τ energy calibration ... 62
5.2.4 Performance measurement in data ... 63
5.3 The τ trigger ... 63
5.3.1 τ trigger performance analyses ... 65
5.3.2 Data and simulation samples ... 67
5.3.3 Object and event selection ... 67
5.3.4 Background strategies ... 68
5.3.5 $Z \to \tau\tau$ tag-and-probe analysis ... 69
5.3.6 $t\bar{t}$ tag-and-probe analysis ... 70

6 Higgs boson analyses with hadronically decaying τ-leptons ... 76
6.1 Analysis techniques ... 76
6.1.1 Signal and control regions ... 76
6.1.2 Modelling of backgrounds ... 76
6.1.3 Signal-to-background discrimination ... 77
6.1.4 Statistical analysis ... 78
6.2 $H \to \tau\tau$ analyses ... 80
6.2.1 Analysis overview ... 80
6.2.2 Mass reconstruction techniques ... 82
6.2.3 Validation of ATLFAST-II simulation ... 83
6.2.4 Estimation of misidentified τ-leptons ... 84
6.2.5 Results ... 84
6.3 $H^+ \to \tau\nu$ analyses ... 85
6.3.1 Analysis overview ... 87
6.3.2 $E_{\mathrm{T}}^{\mathrm{miss}}$ trigger efficiency measurement ... 88
6.3.3 Estimation of misidentified τ-leptons ... 89

6.3.4 Results 89
7 Summary of Papers 92
8 Conclusion 94
9 Sammanfattning på svenska 96
10 Acknowledgements 100
References 102

1. Introduction

> Sacrifice these crutches to the crackling flames
> Stand as silhouettes against the dawn
> It's far too late to try to sleep now
> Seems I'm never tired any more
>
> New Model Army
> *Ballad of Bodmin Pill*

In 2012 the Standard Model (SM) [1–4] of particle physics was completed when the last piece of the puzzle, the Higgs boson, was discovered by the ATLAS and CMS experiments at the Large Hadron Collider (LHC) [5, 6]. The couplings of the Higgs boson to vector bosons and to photons via loops of top quarks were measured as part of the discovery, but more work was required to measure the coupling to fermions. This coupling is arguably best measured in decays to pairs of τ-leptons, because they have a large mass and can be identified relatively well in the detector.

Despite the remarkable predictive power of the SM, it fails to be a complete theory of nature. It predicts that the neutral leptons, the neutrinos, are massless, which is known to be false from measurements of neutrino oscillations. It also fails to present a good candidate for dark matter, and it does not include a description of gravity or an explanation for dark energy. Supersymmetry is a theory that attempts to recover many of the shortcomings of the SM by effectively doubling the particle content. The minimal supersymmetric theory predicts that the number of Higgs bosons are five, rather than just one, and that two of them are charged. This expanded Higgs sector can also be realized as an extension to the SM without supersymmetry, giving rise to a set of models called Two-Higgs Doublet Models (2HDM). Also when considering the fermionic couplings in this class of models, signatures with τ-leptons in the final state are favourable.

This thesis has a focus on the reconstruction of and triggering by τ-leptons that decay into hadrons, and their use in measurements and searches in ATLAS. It describes a measurement of the SM Higgs boson coupling to fermions through decays to two τ-leptons, and a search for the charged Higgs boson predicted by 2HDM in decays to a τ-lepton and a neutrino. The analyses are performed using data from proton–proton collisions at 7 TeV collected by the ATLAS experiment in 2011, at 8 TeV

collected in 2012, and at 13 TeV collected in 2015–2016. The feasibility of using computing resources in the *cloud* as a tool to perform these analyses is also discussed.

A review of the SM, the motivation to look for theories beyond the SM, as well as an introduction to supersymmetry and 2HDM are given in Chapter 2. Chapter 3 describes CERN, the LHC, and the associated experiments, while Chapter 4 gives a more detailed description of the ATLAS detector. Reconstruction and identification of, as well as triggering by, hadronically decaying τ-leptons are treated in Chapter 5, where a measurement of the performance of the τ trigger is also presented. Chapter 6 reviews the analysis techniques used in the ATLAS experiment, and continues with presenting the measurement of the SM Higgs boson coupling to fermions, and the search for charged Higgs bosons. A summary of the papers included in this thesis is given in Chapter 7, detailing the author's contributions. The thesis is concluded in Chapter 8 and a summary in Swedish can be found in Chapter 9.

2. Theoretical background

– Three quarks for Muster Mark!
Sure he hasn't got much of a bark
And sure any he has it's all beside the mark.
But O, Wreneagle Almighty, wouldn't un be a sky of a lark
To see that old buzzard whooping about for uns shirt in the dark
And he hunting round for uns speckled trousers around by Palmerstown Park?
Hohohoho, moulty Mark!
You're the rummest old rooster ever flopped out of a Noah's ark
And you think you're cock of the wark.
Fowls, up! Tristy's the spry young spark
That'll tread her and wed her and bed her and red her
Without ever winking the tail of a feather
And that's how that chap's going to make his money and mark!

James Joyce
Finnegan's Wake

2.1 The Standard Model

The SM [1–4] describes the fundamental constituents of matter and their interactions. It is a quantum field theory which combines the states of matter with three of the fundamental interactions. Figure 2.1 is an illustration of the particle content of the SM[1].

Quarks and leptons are the two families of matter particles. They are fermions (spin $\frac{1}{2}$), and come in three generations and two types. The quark family consists of the up, charm, and top quarks with charge $+\frac{1}{3}$, and of the down, strange, and bottom quarks with charge $-\frac{2}{3}$. The members of the lepton family are the electron (e), muon (μ), and tau lepton (τ) with charge -1, and the corresponding neutrinos: ν_e, ν_μ, and ν_τ, which are neutral. The τ-lepton is a major subject in this thesis, the properties and decays of which are described in detail in Chapter 5. Quarks and charged leptons have corresponding anti-matter variants with opposite charge[2], and they become increasingly massive with each generation.

[1] Quantities in particle physics are usually given in *natural* units, that is $e = \hbar = c = 1$. Masses are given in electronvolt (eV), meaning that $c = 1$ for this unit.
[2] Throughout this thesis, whenever a process is given with the matter particle, the inclusion of the charge conjugate processes is implied.

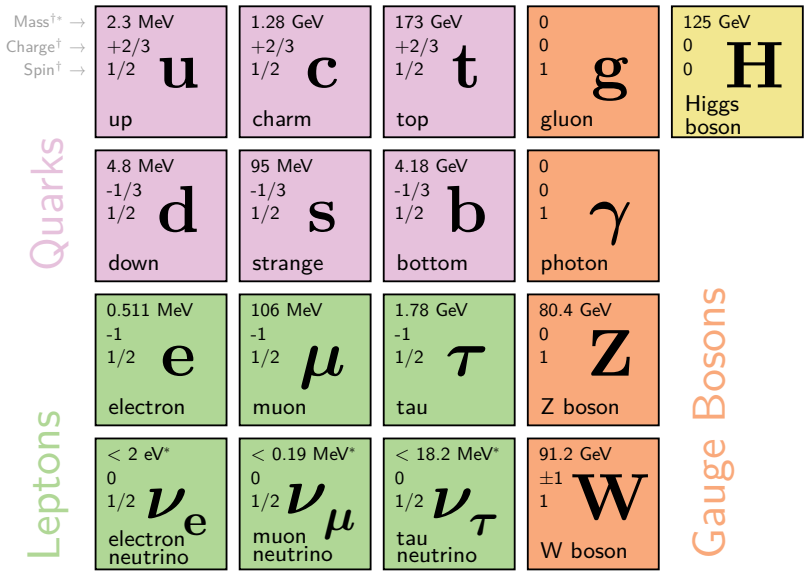


Figure 2.1. The particle content of the SM. The masses are obtained from experimental data [7]. The neutrinos are massless in the SM.

Whether the neutrinos are their own anti-particles (Majorana particles), or Dirac particles as the charged leptons and their anti-particles have not yet been observed, is an area of active research.

The SM also contains four vector bosons (spin 1) carrying three of the four fundamental forces of nature. The electromagnetic interaction is mediated by the massless photon, and acts on the electric charge. It is explained by quantum electrodynamics (QED), the theory of physics which maintains the highest verification precision from experimental measurements. Since the photon is massless, the electromagnetic force is active over an infinite range. The quarks, the charged leptons, and the W bosons all carry electric charge, and are affected by the electromagnetic interaction.

Two massive vector bosons (W and Z) are the force carriers of the weak interaction, which acts on the *weak isospin*. Due to their large masses, the weak interaction only operates at short distances. Weak isospin is carried by all fermions, and the exchange of a W boson transforms a fermion to the second type in the same family and generation, e.g. an electron to an electron neutrino. Quarks can also change generation via the weak interaction, according to the off-diagonal elements of the Cabibbo-Kobayashi-Maskawa (CKM) matrix. The CKM matrix can be parametrized by three mixing angles and the charge–parity (CP)-violating phase, where the latter is responsible for all processes violating CP conservation in the SM.

The electromagnetic and weak interactions are unified in the electroweak interaction.

The gluon is the mediator of the strong force, and it acts on *colour*. Colour comes in three varieties (red, green, blue), and their opposites (anti-red, anti-green, anti-blue), and is carried by the quarks and the gluons themselves. The theory of quark and gluon interactions is called quantum chromodynamics (QCD). The gluon is massless, but its colour gives rise to a self-interaction among gluons which polarizes the vacuum, and strengthens the force with increasing distance. This phenomenon causes quarks to only appear as colour neutral bound states of multiplicity two or more, and is called *colour confinement*. The vacuum polarization of colour has many implications for hadron colliders. Due to its presence, the momentum carried by each of the three bound quarks (valence quarks) do not add up to the total momentum of the hadron. Some fraction is instead distributed among the so-called sea-quarks being constantly created and annihilated inside the hadron, or to the gluons responsible for the polarization. At short distances, the strength of the strong interaction is diminished and the bound quarks experience what is known as *asymptotic freedom*. Despite being an accidental symmetry, hence not forbidden by construction, CP-violation is not observed in QCD.

The SM handles all the symmetries of a relativistic quantum field theory: *translational* (including time) and *rotational* symmetries, as well as symmetry under *boosts*. These symmetries are collectively known as the Poincaré symmetry, and are global symmetries giving rise to the conservation of energy, momentum, and angular momentum. The SM exhibits four accidental global U(1) symmetries, which, by Noether's theorem [8], give rise to baryon, electron, muon, and τ-lepton number conservation.

The SM also has several local (gauge) symmetries. QCD is governed by a $\mathrm{SU}(3)_C$ symmetry, resulting in colour conservation. Similarly, the combined $\mathrm{SU}(2)_L \times \mathrm{U}(1)_Y$ symmetry describes the electroweak interaction, and conserves weak isospin (generated by SU(2)), and weak hypercharge (generated by $\mathrm{U}(1)_Y$). The $\mathrm{SU}(2)_L \times \mathrm{U}(1)_Y$ symmetry is *spontaneously broken* in the SM by the Brout-Englert-Higgs mechanism into a new symmetry $\mathrm{U}(1)_{\mathrm{em}}$, causing conservation of electric charge.

2.1.1 The Brout-Englert-Higgs mechanism

The $\mathrm{SU}(2)_L \times \mathrm{U}(1)_Y$ symmetry of the electroweak interaction has four corresponding gauge fields. The three gauge fields carrying weak isospin are W^a_μ ($a = 1, 2, 3$), and the gauge field carrying weak hypercharge is B_μ. The presumed gauge invariance of the theory requires that the bosons of the gauge fields be massless, in contrast to what is observed for the W and

Z bosons. Direct introduction of a mass term in the Lagrangian breaks the *renormalizability* of the theory, and it is instead introduced via the Brout-Englert-Higgs (or Englert–Brout–Higgs–Guralnik–Hagen–Kibble) mechanism [9–14].

The most economic choice, in terms of additional fields, to provide masses to the W and Z bosons is through a complex scalar doublet field

$$\Phi(x) = \begin{pmatrix} \phi^+(x) \\ \phi^0(x) \end{pmatrix}, \tag{2.1}$$

called the Higgs field. The Lagrangian for this field is

$$\mathcal{L} = (D_\mu \Phi)^\dagger (D^\mu \Phi) - V(\Phi), \tag{2.2}$$

where D_μ is the covariant derivative connecting the Higgs field with the W_μ^a and B_μ fields

$$D_\mu \Phi = (\partial_\mu - igW_\mu^a \sigma^a/2 - ig'YB_\mu/2)\Phi. \tag{2.3}$$

Here, σ^a are the Pauli matrices, g and g' the couplings for $\mathrm{SU}(2)_L$ and $\mathrm{U}(1)_Y$, respectively, and Y the weak hypercharge quantum number.

Through this connection, the Nambu-Goldstone bosons that would normally result from a complex scalar doublet field, are *eaten* while giving mass to the W and Z bosons. These masses are generated by breaking the gauge symmetry of the vacuum state, which happens if, at the minimum of the potential $V(\Phi)$, Φ has a non-zero value (the vacuum expectation value, v). By the requirements of renormalizability and gauge invariance, only terms of order 2 or 4 are allowed in the potential. It is thus parametrized by

$$V(\Phi) = -\mu^2(\Phi^\dagger \Phi) + \lambda(\Phi^\dagger \Phi)^2, \tag{2.4}$$

where $\lambda > 0$ is a requirement for the vacuum to remain stable. With $\mu^2 < 0$, two degenerate minima of the potential emerge for $\Phi^\dagger \Phi = -\mu^2/(2\lambda) \equiv v^2/2$.

To conserve electric charge, the non-zero expectation value must enter via the neutral field component of Eq. (2.1), thus

$$\langle \Phi \rangle = \frac{1}{\sqrt{2}} \begin{pmatrix} 0 \\ v \end{pmatrix}. \tag{2.5}$$

Expanding Eq. (2.2) around this minimum results in a parametrization for the physical fields of the weak interaction as follows:

$$W_\mu^\pm = (W_\mu^1 \mp W_\mu^2)/\sqrt{2}, \qquad m_W^2 = \frac{g^2 v^2}{4}, \tag{2.6}$$

$$Z_\mu = \cos\theta_W W_\mu^3 - \sin\theta_W B_\mu, \qquad m_Z^2 = \frac{(g'^2 + g^2)v^2}{4}, \tag{2.7}$$

where:

$$\cos\theta_W = \frac{g}{\sqrt{g^2 + g'^2}}, \qquad \sin\theta_W = \frac{g'}{\sqrt{g^2 + g'^2}}, \tag{2.8}$$

and with this relation between the W and Z mass

$$m_Z^2 = \frac{m_Z^2}{\cos^2\theta_W}. \tag{2.9}$$

The relation between m_W and m_Z fixes the vacuum expectation value, which has also been measured via the Fermi coupling constant (G_F) in muon decays with a high accuracy [15]:

$$v = \frac{2m_W}{g} = \left(\frac{1}{\sqrt{2}G_F}\right)^{1/2} \approx 246\,\text{GeV}. \tag{2.10}$$

The degree of freedom that remains after the W and Z bosons have acquired their masses manifests itself in the SM as the Higgs boson. The mass of the Higgs boson is a free parameter of the SM, and the Higgs field exhibits self-interactions that contribute to its mass. The Higgs boson was discovered in 2012 by the CMS and ATLAS experiments [5, 6], making the SM a complete theory.

To be a satisfactory solution, the Higgs field must also be able to generate masses for the fermions. The fermion fields in the SM are *chiral* eigenstates formed by left-handed doublet and right-handed singlet representations of $\text{SU}(2)_L$. The left- and right-handed fields have different transformation properties, and the naive fermion mass term

$$\mathcal{L}_{m_f} = -m_f(\bar{\psi}_L\psi_R + \bar{\psi}_R\psi_L) \tag{2.11}$$

does not preserve gauge symmetry. Instead, a *Yukawa* coupling to the Higgs field is responsible for generating the masses of the quarks and the charged leptons [2, 16, 17]. The Lagrangian for the Yukawa coupling in the mass eigenstate basis, and for the first generation of particles, is

$$\mathcal{L}_{\text{Yukawa}} = y_d\bar{q}_L\Phi d_R + y_u\bar{q}_L(i\sigma^2\Phi)u_R + y_l\bar{l}_L\Phi e_R + h.c., \tag{2.12}$$

The neutrinos do not have a right-handed representation, and are massless in the SM. y_{d_i} and y_{u_i} $(i = 1, 2, 3)$ are the Yukawa coupling constants for the quarks, and are used to form the CKM matrix, while y_{l_i} are the coupling constants for the charged leptons. Expanding Eq. (2.12) around the vacuum expectation value gives this expression for the fermion masses

$$m_f = y_f\frac{v}{\sqrt{2}}. \tag{2.13}$$

2.1.2 Higgs boson production and decay

At the LHC, the SM Higgs boson is predominantly produced in the merging of two gluons (*gluon-gluon fusion*). Other production modes are, in order of decreasing production cross-section, *vector boson fusion* (VBF), production in association with a vector boson (VH), and in association with a top-quark pair (ttH). The Feynman diagrams for three of these modes are shown in Figure 2.2, while the production cross-sections are given in Table 2.1.

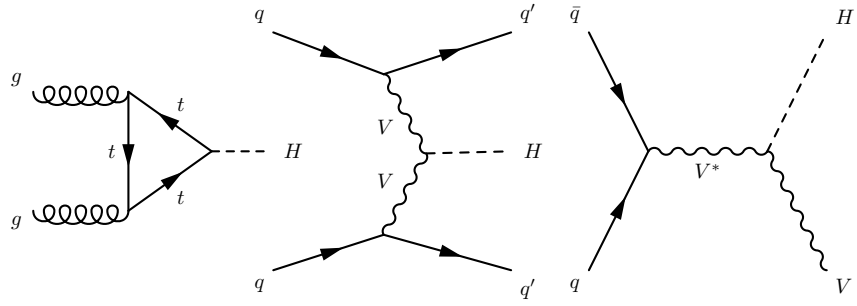


Figure 2.2. Feynman diagrams of the three main production modes for the Higgs boson: gluon-gluon fusion (left), VBF (middle), and VH (right).

Table 2.1. *Production cross-section for a Higgs boson with a mass of* 125.1 *GeV in pp collisions at the LHC with a centre-of-mass energy of* $\sqrt{s} = 8$ *TeV [18]. The cross-sections are calculated at different orders of pertubation theory.*

Production mode	**Cross-section**
Gluon-gluon fusion	19 pb
VBF	1.6 pb
WH	0.70 pb
ZH	0.41 pb
ttH	0.13 pb

The Higgs boson in the SM can decay into pairs of vector bosons (W^+W^-, ZZ^*) or pairs of fermions (bb, $\tau^-\tau^+$, etc.) at tree-level. For the Higgs boson to decay to two photons ($\gamma\gamma$), it must do so via a next-to-leading-order (NLO) loop involving predominantly top or bottom quarks. Figure 2.3 shows the Higgs boson branching fractions to the different decays. Section 6.2 describes a measurement of the Higgs boson branching fraction in decays to two τ-leptons.

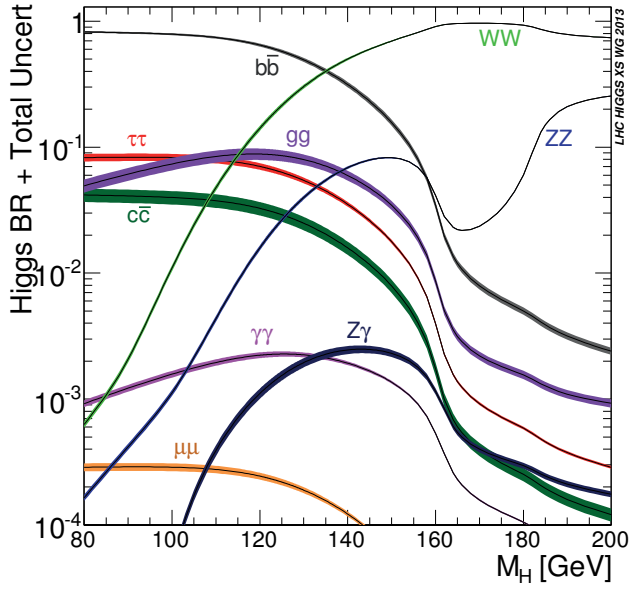


Figure 2.3. Branching fractions of the decays of the SM Higgs boson, as a function of its mass [18].

2.2 Beyond the Standard Model

Despite its successes, the SM can not be a complete theory of nature. Most prominently, it lacks a description of gravity, and is incompatible with general relativity. It does not provide a credible particle candidate for Dark Matter (DM), and no explanation for dark energy or *inflation*.

It is also incomplete with respect to the particles and interactions that it does cover. It predicts that neutrinos should be massless, which is incompatible with the observation of neutrino oscillations [19]. Further, if the neutrino masses are generated by Yukawa couplings, it would require the existence of right-handed neutrinos and that the corresponding couplings are *unnaturally* small. While CP-violation of quarks is allowed via the CKM matrix of the weak interaction, no occurrence of lepton flavour or CP-violation has been observed, hence the SM can not explain the *matter–anti-matter asymmetry* in the Universe.

Other aspects of the SM are more æsthetic in nature. It does not explain why the number of particle generations is restricted to three, nor why there is no CP-violation in QCD. Further, there is no scale at which the strengths of the strong, weak, and electromagnetic interactions unify, there is no explanation for the apparently arbitrary values of the free parameters of the SM, and the observed mass of the Higgs bosons requires a remarkable *fine-tuning* of the contributions from loop corrections.

2.2.1 The Minimal Supersymmetric Standard Model

Since symmetry has been such a successful principle in guiding the development of theories for particle physics, it is natural to try to resolve the problems that the SM exhibits with one more symmetry.

The fine-tuning problem would essentially disappear if loop corrections from particles were cancelled out by partners with similar properties. One way to do this is to postulate that for every fermion field, there is a corresponding bosonic field, and vice versa. Supersymmetry (SUSY) doubles the particle content of the SM by introducing superpartners (*sparticles*) for each particle type, thus bosonic *sleptons* and *squarks*, and fermionic *gauginos* and *higgsinos*. Since these sparticles are not observed, their masses must be at a higher scale than the SM particles, and SUSY must be broken at the SM scale.

The gauginos and the higgsinos of SUSY mix into six different mass eigenstates. These are the four *neutralinos* ($\tilde{X}_i^0$) and the two *charginos* ($\tilde{X}^{\pm}$). To resolve problems with baryon and lepton number conservation in SUSY, a discrete parity called R-parity is introduced, given by

$$R = (-1)^{3B+L+2S}, \tag{2.14}$$

where B is the baryon number (1/3 for quarks), L the lepton number, and S the spin. Thus, SM particles have $R = +1$, and sparticles $R = -1$. If this parity is exactly conserved, SUSY particles can only be produced in pairs, and the $\tilde{X}_1^0$ with the lowest mass is stable. A stable $\tilde{X}_1^0$ may manifest itself as missing energy signatures at colliders, and is an excellent candidate for cold DM.

A single Higgs field is incompatible with SUSY, because it would lead to the theory being non-renormalizable. An additional Higgs field is introduced to resolve these problems. The new set of Higgs fields are given by:

$$H_d = \begin{pmatrix} H_d^0 \\ H_d^- \end{pmatrix}, \qquad H_u = \begin{pmatrix} H_u^+ \\ H_u^0 \end{pmatrix}, \tag{2.15}$$

with vacuum expectation values:

$$\langle H_d \rangle = \frac{1}{\sqrt{2}} \begin{pmatrix} v_d \\ 0 \end{pmatrix}, \qquad \langle H_u \rangle = \frac{1}{\sqrt{2}} \begin{pmatrix} 0 \\ v_u \end{pmatrix}, \tag{2.16}$$

and where the overall scale is fixed to $v^2 = (v_d^2 + v_u^2)$. The ratio of the two vacuum expectation values has a large impact on the parameters of this expanded Higgs sector, and it is defined as

$$\tan\beta \equiv \frac{v_u}{v_d}. \tag{2.17}$$

Of the eight degrees of freedom of the two Higgs fields, three are again used to give mass to the W and Z bosons, while the remaining form five Higgs boson eigenstates. These are the CP-even Higgs bosons h and H, the latter of which has higher mass, the CP-odd Higgs boson A, and two charged Higgs bosons $H^{\pm}$. One of h or H takes the role of the Higgs boson in the SM, while the A and the $H^{\pm}$ are completely new types of particles. The charged Higgs boson is one of the focuses of this thesis, and its properties and phenomenology are covered in Section 2.3, while a search in ATLAS is presented in Section 6.3.

The Higgs boson masses are not independent of each other, and one of them, along with $\tan\beta$, is sufficient to describe all masses at tree-level. Selecting m_A as the free parameter, the other masses are:

$$m^2_{h,H} = \frac{1}{2}\left(m^2_A + m^2_Z \mp \sqrt{(m^2_A + m^2_Z)^2 - 4m^2_A m^2_Z \cos^2 2\beta}\right), \tag{2.18}$$

$$m_{H^{\pm}} = m^2_A + m^2_Z. \tag{2.19}$$

The neutral h and H are formed from mixing the real parts of H^0_d and H^0_u with an angle α. It is given by

$$\tan 2\alpha = \frac{m^2_A + m^2_Z}{m^2_A - m^2_Z}\tan 2\beta, \tag{2.20}$$

such that α and $\tan\beta$ determine the couplings of the neutral Higgs bosons to the fermions and the gauge bosons.

Beyond tree-level, the mass of the lightest neutral Higgs boson is influenced via radiative corrections by the average of the *stop* particle masses $m_{\text{SUSY}} = \sqrt{m_{\tilde{t_1}} m_{\tilde{t_2}}}$, as well the stop mixing parameter $X_t = A_t - \mu\cot\beta$. Here A_t is is the Higgs-stop coupling which is responsible for the soft SUSY-breaking, and μ is the higgsino mass.

2.2.2 Two-Higgs Doublet Models

The Higgs sector of the MSSM is an example of a larger class of models for an expanded Higgs sector: the 2HDM [20]. These are characterized by the presence of two Higgs fields, but do not require SUSY. To avoid flavour-changing neutral currents, which have not been observed in nature, it is necessary that all quarks and leptons with the same charge couple to the same Higgs field according to the Paschos-Glashow-Weinberg theorem [21, 22]. Thus, the 2HDM are classified depending on which Higgs field up-type quarks, down-type quarks, and leptons couple to. The four classes of 2HDM and their couplings are given in Table 2.2.

Table 2.2. *The different types of 2HDM and which Higgs field each type of charged particle couple to, where u_R are up-type quarks, d_R down-type quarks, and l_R the charged leptons.*

Type	u_R	d_R	l_R
Type I	Φ_2	Φ_2	Φ_2
Type II	Φ_2	Φ_1	Φ_1
Lepton specific	Φ_2	Φ_2	Φ_1
Flipped	Φ_2	Φ_1	Φ_2

2.2.3 MSSM benchmark scenarios

Several benchmarking scenarios have been devised to place conservative upper bounds on the exclusion limits of the MSSM Higgs sector. The m_h^{max} scenario maximizes the mass of the lightest neutral Higgs boson to provide conservative upper bounds on $\tan\beta$ from searches [23]. In light of the discovered Higgs boson with $m_h = 125\,\text{GeV}$, only a very small region of the m_A–$\tan\beta$ plane is still available in this scenario. Modified scenarios ($m_h^{\text{mod}\pm}$) have been suggested to allow for a larger parameter space [24], where X_t is adjusted to reduce the contribution to m_h from radiative corrections, and the $\pm$ refers to its sign.

The hMSSM scenario uses a different approach to assert that when one considers $m_h = 126 \pm 3\,\text{GeV}$ (where the uncertainty includes the expected theoretical and experimental components) the radiative corrections to the Higgs sector masses are already fixed to a good approximation [25, 26]. It does so by varying μ, m_{SUSY}, and X_t and observing that the changes to the other Higgs boson masses are small. Figure 2.4 shows the exclusion limits from direct searches and measurements of the couplings of the observed Higgs boson in the hMSSM scenario.

With the increasing lower bounds on SUSY particles (in particular for the stops) from direct searches, low m_{SUSY} and high $\tan\beta$ values become less compatible with the observed results. Ref. [27] discusses the hMSSM scenario at low $\tan\beta$, and suggests the *low-tb-high* scenario which takes additional logarithmic corrections into account.

2.3 Charged Higgs bosons

2.3.1 Production of charged Higgs bosons

Because of their coupling to mass, the charged Higgs bosons predicted by 2HDM are produced in decays of or association with top quarks at the LHC. In the SM, the top-quark decays to a b-quark and a W boson. The charged Higgs boson is called light or heavy if its mass (m_{H^+}) is lower or higher than the top-quark mass (m_t), respectively. For light charged Higgs bosons, it can substitute the W in top-quark decays. Production

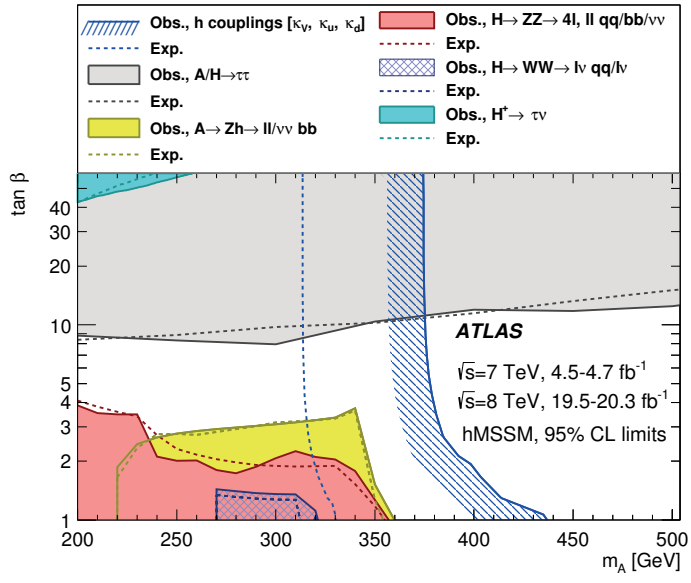


Figure 2.4. Excluded regions in the $\tan\beta$–m_A plane in the hMSSM scenario from direct searches of neutral and charged Higgs bosons, and from constraints on fits to the Higgs boson couplings to up- and down-type quarks, and to vector bosons.

of heavy charged Higgs bosons can be described with the five-flavour scheme (5FS) where the b-quark is considered as one of the partons, or the four-flavour scheme (4FS) where the charged Higgs boson is produced via gluon-gluon fusion. The descriptions are theoretically equivalent, but present different computational challenges. They are usually averaged according to the Santander matching [28] to produce the most reliable estimate of the production cross-section. Figure 2.5 shows the Feynman diagrams of the main production modes of the charged Higgs boson.

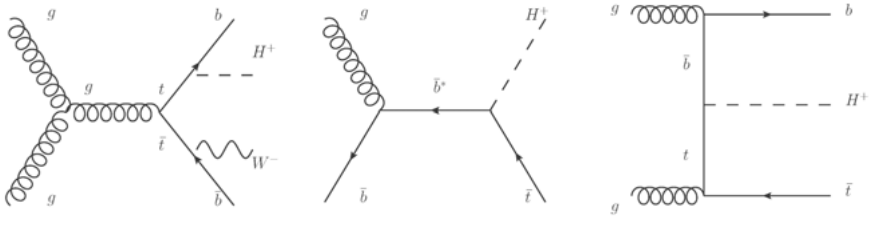


Figure 2.5. The main production modes of the charged Higgs boson in 2HDM for $m_{H^+} < m_t$ (left), and for $m_{H^+} > m_t$ in the 5FS (middle) and 4FS (right).

2.3.2 Decays of charged Higgs bosons

The charged Higgs boson decays almost exclusively to $\tau\nu$ for $m_{H^+} < m_t$ in most of the $\tan\beta$ range, while cs becomes increasingly important at low $\tan\beta$ values. Above m_t, it predominantly decays to tb, and, in the MSSM, to heavier sparticles. Figure 2.6 shows the branching fractions for charged Higgs boson decays in the $m_h^{\text{mod+}}$ MSSM scenario.

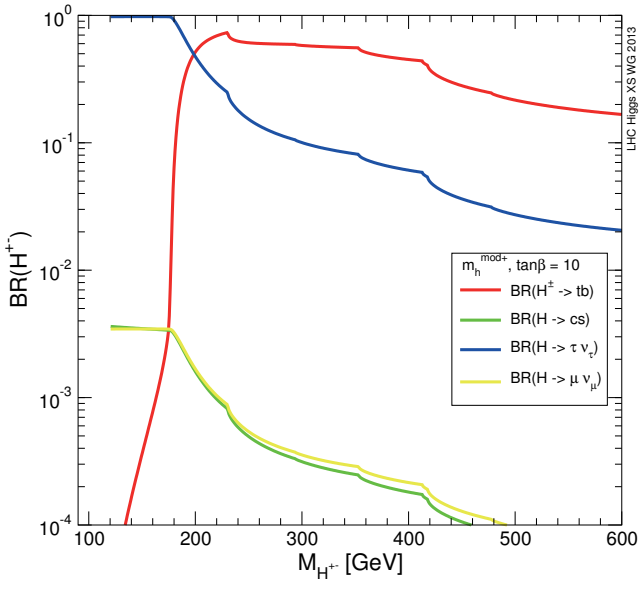


Figure 2.6. Branching fractions of charged Higgs boson decays in the $m_h^{\text{mod+}}$ MSSM scenario for $\tan\beta = 10$ as a function of m_{H^+} [18]. Branching fractions to sparticles are not shown.

2.3.3 Charged Higgs boson searches

Charged Higgs boson searches have been performed by the ATLAS and CMS experiments with collision data at 7 TeV and 8 TeV collected in 2011–2012. They cover the $H^+ \to cs$ [29, 30], $H^+ \to \tau\nu$ [31, 32], and $H^+ \to tb$ decays [32, 33], for masses both below and above m_t. No excess above the SM expectation is found in any of the searches. 95 % confidence-level (CL) exclusion limits are shown in Figure 2.7 for searches in $H^+ \to cs$ and $H^+ \to \tau\nu$ decays with ATLAS and CMS. For heavy charged Higgs bosons, the exclusion limit is shown in Figure 2.8 for the searches in $H^+ \to tb$ as well as $H^+ \to WZ$ decays with ATLAS. Exclusion limits are further discussed in Section 6.1.4. The search for heavy charged Higgs bosons in $H^+ \to \tau\nu$ decays, using 13 TeV data with ATLAS is described in more detail in Section 6.3. Exclusion limits on charged Higgs bosons from searches using data from the Large Electron Positron

(LEP) collider, as well as from from B-physics and other measurements, are not presented in this thesis.

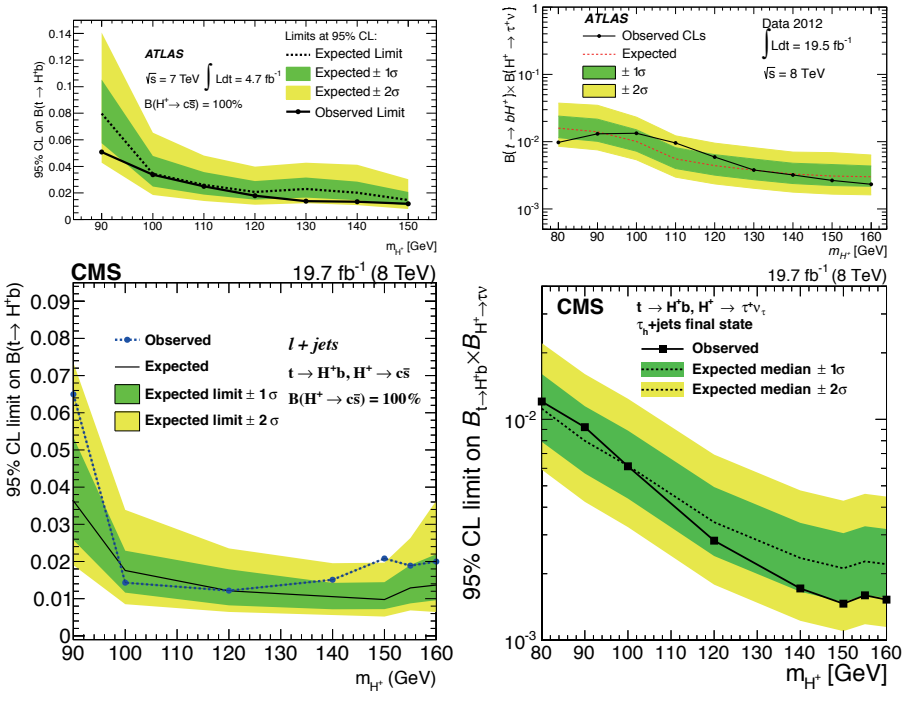


Figure 2.7. 95 % CL exclusion limit on the branching fraction $\mathcal{B}(t \to H^+b)$ (assuming $\mathcal{B}(H^+ \to cs) = 100\,\%$) (left) and on $\mathcal{B}(t \to H^+b) \times \mathcal{B}(H^+ \to \tau\nu)$ (right), as a function of m_{H^+} with ATLAS (top) and CMS (bottom).

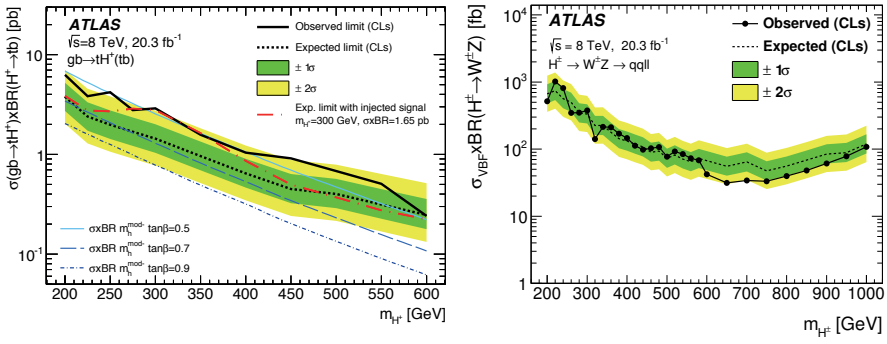


Figure 2.8. 95 % CL exclusion limits on $\sigma(gb \to tH^+) \times \mathcal{B}(H^+ \to tb)$ (left) and of $\sigma_{\mathrm{VBF}} \times \mathcal{B}(H^+ \to WZ)$ (right) as a function of m_{H^+} with ATLAS. In the left plot, the expected limit from an injected signal of $\sigma = 1.65\,\mathrm{pb}$ with $m_{H^+} = 300\,\mathrm{GeV}$ is included for comparison.

3. CERN and the Large Hadron Collider

3.1 CERN

The European Organization for Nuclear Research (CERN) is an international laboratory situated on the border between Switzerland and France near Geneva. Founded in 1952, it is governed by an international collaboration with 23 member states. Many more states and organizations have co-operation agreements and scientific contact with CERN. Its facilities are used by over 600 universities and institutes, corresponding to about 12000 scientists from over 70 countries and of 120 different nationalities visiting CERN to conduct their research.

The CERN laboratory hosts particle accelerators and experiments designed to examine the constituents of matter and the fundamental forces of nature. CERN itself is mainly responsible for providing the particle accelerators and infrastructure used by the experiments, and most of its funding goes toward designing, building, and operating machines such as the LHC (see Section 3.3). For this purpose, CERN employs about 2500 scientific and technical staff.

3.2 Past accelerators and experiments

CERN has a very successful history of building and running particle accelerators and their corresponding experiments. In 1976, the Super Proton Synchrotron started up, accelerating protons to about 400 GeV. It was converted into a proton–antiproton ($p\bar{p}$) collider in 1979, and was used to discover the W [34, 35] and Z [36, 37] bosons in 1983 together with the attached experiments UA1 and UA2. This discovery awarded two CERN scientists, Carlo Rubbia and Simon van der Meer, the Nobel Prize the following year.

The 27 km underground tunnel which was to host the Large Electron-Positron (LEP) Collider [38, 39] was completed in 1988. The machine was commissioned the following year and proceeded to deliver e^+e^- collisions until it was shut down in 2000, reaching a maximum centre-of-mass energy of 209 GeV. Data from LEP's four detectors (ALEPH, DELPHI, L3, and OPAL) provide precision measurements of the electroweak theory, for instance by proving that there are only three generations of light neutrinos (with a mass lighter than half the Z boson mass) [40].

3.3 The Large Hadron Collider

The Large Hadron Collider (LHC) [41] is the largest and most powerful accelerator ever built. A schematic of the LHC ring, its accelerator infrastructure, and the locations of its four main experiments is shown in Figure 3.1.

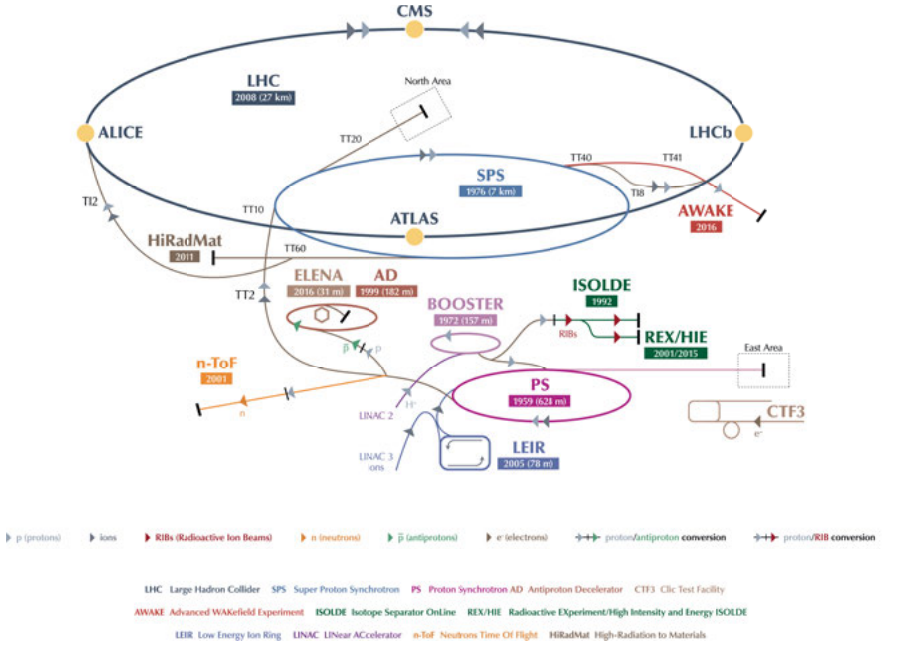


Figure 3.1. Schematic of the LHC ring with its accelerator infrastructure, and the locations of the main and auxiliary experiments shown.

The main operating mode of the LHC is *pp* collisions, but it is also used to collide lead ions with protons (p–Pb) and with other lead ions (Pb–Pb). It was approved in 1994, and started operation in November 2009 (following an incident during its initial startup in September 2008). It was successfully commissioned in 2010, and delivered collisions during 2011 and 2012. After the first long shutdown (LS1) in 2013–2014, the LHC started up again in June 2015 and has continued to deliver collisions in 2016.

The LHC is constructed in the same tunnel that housed LEP. The ring is divided into octants, where four of the points between two consecutive octants are interaction points for the different experiments, two are used for beam cleaning and focusing, and one is used to dump the beam. The LHC uses superconducting NbTi/Cu dipole magnets creating an 8 T magnetic field to keep the protons in their almost circular orbit. The operating temperature of the magnets is 1.9 K, and this is achieved with a liquid helium cryogenic system. The eight accelerating cavities

per beam accelerate the protons to the operating energy. The cavities are also responsible for keeping the bunches tight along the beam axis, while quadrupole magnets are used to focus the beams in transverse directions. The beam pipe operates under *ultra-high vacuum*, of the order of 10^{-10} mbar.

The journey of the protons begins at a bottle of hydrogen gas. The hydrogen atoms are stripped of their electrons and are accelerated in a linear accelerator (Linac) from 2 MeV to 50 MeV. They are then accelerated by, in sequence, the Proton Synchrotron Booster (PSB) to 1.4 GeV, the Proton Synchrotron (PS) to 25 GeV, and finally the Super Proton Synchrotron (SPS) to 450 GeV, before being eventually injected into the LHC.

Two figures of merit are used when designing an accelerator. The centre-of-mass energy is defined as the total energy of two colliding particles in the centre-of-mass reference frame. The LHC was originally designed to accelerate protons to 7 TeV, resulting in a 14 TeV centre-of-mass energy. The second figure is the instantaneous luminosity, which is a measure of the surface density of collisions per unit time. With a 25 ns spacing between bunches (40 MHz bunch-crossing rate), and with about 2800 bunches and 10^{11} protons per bunch, the designed instantaneous luminosity is $10^{34}\,\mathrm{cm}^{-2}\,\mathrm{s}^{-1}$. The integrated luminosity states the number of interactions over a time period relative to a given cross-section. For instance, $1\,\mathrm{pb}^{-1}$ is the integrated luminosity that corresponds to, on average, one interaction for a process with a cross-section of 1 pb.

The LHC delivered collisions corresponding to an integrated luminosity of $5.5\,\mathrm{fb}^{-1}$ at 7 TeV in 2011 and $22.8\,\mathrm{fb}^{-1}$ at 8 TeV in 2012. In 2015, the LHC started operating at 6.5 TeV per beam, and has in 2016 exceeded the design instantaneous luminosity with $1.32 \times 10^{34}\,\mathrm{cm}^{-2}\,\mathrm{s}^{-1}$. It has delivered collisions at 13 TeV corresponding to an integrated luminosity of $4.2\,\mathrm{fb}^{-1}$ in 2015 and, at the time of writing, to $31.9\,\mathrm{fb}^{-1}$ in 2016.

3.4 The LHC experiments

At opposite sides of the LHC sit its two largest experiments: ATLAS (A Toroidal LHC ApparatuS) [42] and CMS (Compact Muon Solenoid) [43]. These general-purpose experiments were built to study the SM (including finding the Higgs boson) and to search for signs of physics beyond the SM, e.g. signatures of extra dimensions, new gauge bosons, additional Higgs bosons, dark matter candidates, and SUSY particles.

In the ATLAS experiment, tracking of charged particles is provided by the inner detector, which consists of the pixel and silicon microstrip (SCT) detectors, as well as the Transition Radiation Tracker (TRT). A 2 T magnetic field generated by a superconducting solenoid enables charge

and momentum measurements. Surrounding the inner detector is the electromagnetic and hadronic calorimeters, which record energy deposits mainly from electrons, photons, and hadrons, and are also used for particle identification and triggering. The calorimeters are subdivided into *barrel* and *end-cap* components, allowing near-hermetic enclosure of the collisions. Outside the calorimeters sits the muon spectrometer, which provides tracking, momentum measurement, identification, and triggering for muons. The muon spectrometer is supported by a 4 T magnetic field provided by superconducting toroids in both the barrel and end-caps. The ATLAS experiment is described in more detail in Chapter 4.

The CMS experiment is similar to the ATLAS experiment in many aspects. It relies on pixel and microstrip silicon detectors for tracking, electromagnetic and hadronic calorimeters that completely enclose the collisions, and a muon spectrometer. Where it differs from ATLAS is the lack of a TRT, the choice of material in the calorimeters, and that CMS has a homogenous electromagnetic calorimeter, while a sampling technique is used in ATLAS. Most importantly, CMS relies on a single superconducting solenoid to provide a 3.8 T magnetic field to the tracker, and uses the returning magnetic field for the muon spectrometer.

The ATLAS and CMS experiments proved the existence of the Higgs boson in 2012 [5, 6]. The mass of the Higgs boson has been measured to be $125.09 \pm 0.21(\text{stat.}) \pm 0.11(\text{syst.})$ GeV [44], and Figure 3.2 shows the individual and combined results of the different mass measurements.

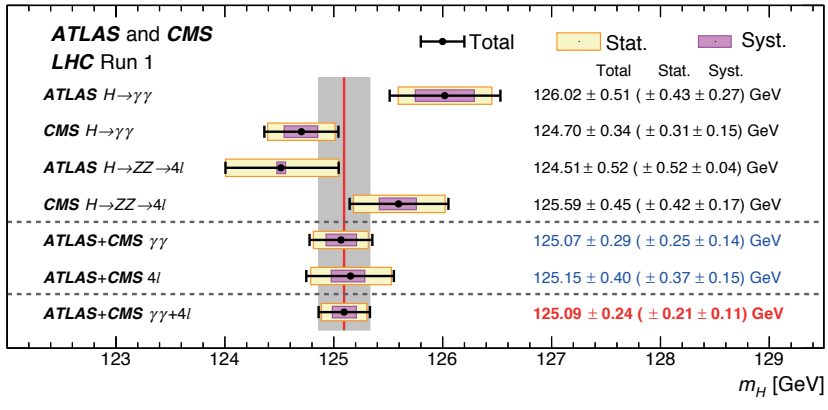


Figure 3.2. Summary of the Higgs boson mass measurements of the individual analyses with ATLAS and CMS, and their combination. Both experiments use the $H \to \gamma\gamma$ and $H \to ZZ^* \to 4l$ channels for their measurements.

In the nearest clockwise octant from ATLAS sits ALICE (A Large Ion Collider Experiment) [45]. This detector is designed to study the quark-gluon plasma, a state of matter where the energy density is so large that

quarks and gluons are not bound into hadrons (colour confinement) [46]. ALICE provides experimental data that are fundamental for improving the understanding of QCD and for solving the problem of chiral symmetry restoration.

In the nearest octant on the opposite side from ATLAS is the LHCb (Large Hadron Collider Beauty) experiment [47]. Contrary to ATLAS, CMS, and ALICE, the LHCb only covers one *forward* region, i.e. the region nearest the beam axis in one direction. It specializes in b-physics, and studies asymmetries in decays of b- and $\bar{b}$-quarks with the aim of unveiling the reason for the matter-antimatter asymmetry in the universe. The LHCb experiment is also searching for *exotic* composite particles that cannot be described in a model where only hadrons with two (mesons) or three (baryons) quarks exist.

The TOTEM [48] experiment covers almost half a kilometre around the CMS experiment and makes precise measurements of particles escaping the detector at small angles. It is designed to measure the pp cross-section, and to improve the knowledge about the proton structure.

The LHCf (Large Hadron Collider forward) experiment [49] consists of two detectors situated on either side of ATLAS. Similarly to TOTEM, it uses particles escaping the detector in the forward direction, and these are used to simulate how cosmic rays cause cascades of particles when colliding with nuclei in the atmosphere.

The latest experiment to be added to the LHC is the Monopole and Exotics Detector at the LHC (MoEDAL) [50]. Its main task is to search for magnetic monopoles and highly ionizing stable massive particles.

3.5 Other experiments at CERN

Many other experiments are housed at CERN covering a wide range of topics in particle physics. Several of these use the SPS as their source of beam particles:

- the COMPASS (Common Muon and Proton Apparatus for Structure and Spectroscopy) [51], which uses muons from pion and kaon decays, produced by firing protons at a target, to examine how spin is produced in protons and neutrons,
- the NA61/SHINE (SPS Heavy Ion and Neutrino Experiment) [52], which studies hadron production in collisions of beam particles with fixed targets,
- the NA62 and NA48/2 [53] experiments, which study rates of rare kaon decays to determine the $|V_{td}|$ element of the CKM matrix.

The DIRAC (Dimeson Relativistic Atom Complex) [54] uses the PS to study the behaviour of the strong force at relatively low energies. The Antiproton Decelerator (AD) [55] provides antiprotons to:

- ACE (Antiproton Cell Experiment), which studies the suitability of antiprotons for cancer treatment,
- AEGIS (Antihydrogen Experiment: Gravity, Interferometry, Spectroscopy), which measures the Earth's gravitational acceleration (g) on antihydrogen atoms,
- ALPHA, which produces and studies the properties of antihydrogen atoms,
- ASACUSA (Atomic Spectroscopy And Collisions Using Slow Antiprotons), which probes matter-antimatter symmetries using atoms containing antiprotons,
- ATRAP (Antihydrogen trap), which compares the properties of hydrogen and antihydrogen atoms.

ISOLDE (Isotope mass Separator On-Line facility) [56] provides low energy beams of unstable radioactive nuclides, and the nTOF (neutron time-of-flight facility) provides beams of neutrons over a large range of energies. The CLOUD (Cosmics Leaving Outdoor Droplets) [57] experiment uses a cloud chamber to investigate a possible link between cosmic rays and cloud formation in the atmosphere, and the CAST (CERN Axion Solar Telescope) [58] experiment searches for axion particles originating from the Sun.

4. The ATLAS experiment

The ATLAS experiment is an international collaboration consisting of about 5000 scientists from nearly 180 institutions in 38 countries. It is a general-purpose experiment which uses collisions from the LHC to make precise measurements of the predictions of the SM, and to search for new particles and phenomena.

4.1 Description of the ATLAS detector

The ATLAS detector [42] is constructed as a 46 m long and 25 m diameter cylinder weighing about 7000 tonnes. It consists of many sub-systems: the inner detector provides tracking of charged particles, and is described in Section 4.1.2; the calorimeter system measures the energy of all particles except muons and neutrinos, as described in Section 4.1.3; the muon spectrometer is responsible for measuring momenta and charges of muons (which punch through the calorimeter system), as well as triggering events where muons are present, and is described in Section 4.1.4. Finally, the magnet system *bends* the trajectories of charged particles in the inner detector and the muon spectrometer and is described in Section 4.1.6. Figure 4.1 shows a cut-away drawing of the ATLAS detector and its sub-systems.

A multi-level trigger [59], involving different parts of the detector, is responsible for selecting events that are interesting for physics analyses. The trigger system, the electronics for read-out of the event information, and the system for initial storage of the data are collectively called the Trigger and Data Acquisition System (TDAQ), and are described in Section 4.3.

To store, process, and analyze the huge amounts of data produced by the detector, as well as to produce simulation of known and hypothesized physical processes, ATLAS employs the Grid, a large computing system distributed over 130 computing centres worldwide. The ATLAS computing system is described in Section 4.4.

4.1.1 Overview

The ATLAS detector is symmetric around the beam axis and in the forward-backward direction with respect to the collision point. It uses

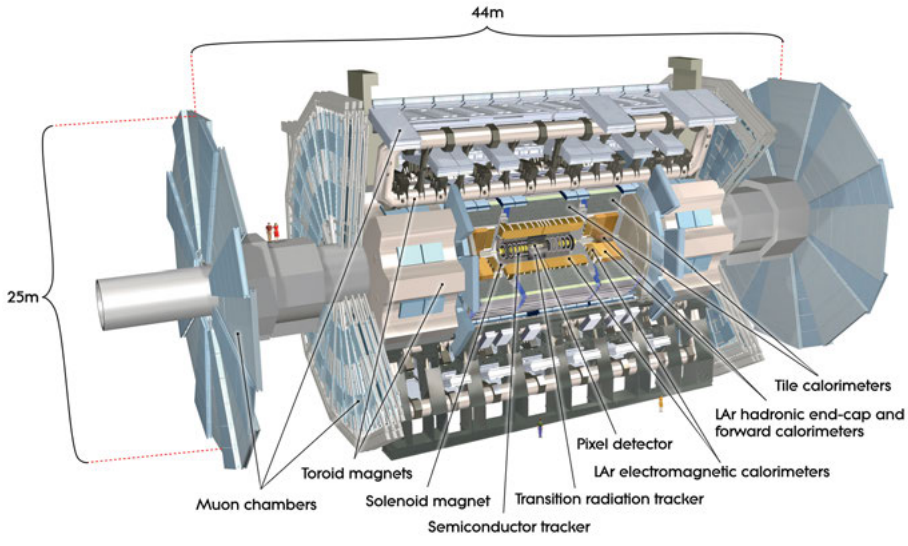


Figure 4.1. Schematic of the ATLAS detector at the LHC.

a right-handed coordinate system, where the z axis is directed along the beam, the y axis points upwards, and the x axis towards the centre of the LHC ring, with the origin at the interaction point. In spherical coordinates, θ describes the direction in the y–z plane and is called the polar angle, while the azimuthal angle ϕ represents the direction in the x–y (transverse) plane.

Rapidity is a measure of relativistic velocity and is defined as

$$y = \frac{1}{2} \ln \frac{E + p_z}{E - p_z}.$$

Differences in rapidity are invariant under Lorentz boosts along the z axis, which makes it a convenient substitute for the polar angle. In the low-mass limit, it can be approximated by the *pseudorapidity*

$$\eta = -\ln \tan \frac{\theta}{2}.$$

The quantity used to measure angular distances in the η–ϕ plane is

$$\Delta R = \sqrt{(\Delta\eta)^2 + (\Delta\phi)^2}.$$

The ATLAS detector is constructed to cover the whole azimuthal range, and almost the entire pseudorapidity range. The LHC collides hadrons and the longitudinal momentum fractions of their constituents remain unknown, thus the total energy going into an individual interaction is

also unknown. Full coverage in η and ϕ enables measurement of the total energy of the event, and to determine the energy balance in the transverse plane. This is important to be able to analyze events that contain undetectable neutrinos or other weakly interacting particles.

The ATLAS detector is divided into several regions in $|\eta|$. The high-precision region covers the range $|\eta| < 2.5$ and corresponds to the barrel and parts of the end-cap. Here the trackers, calorimeters, and the muon spectrometer have the highest precision. The muon spectrometer has coverage up to $|\eta| = 2.7$, while the calorimeters in the end-cap extend up to $|\eta| = 3.2$, and the forward calorimeters extend even further, up to $|\eta| = 4.9$.

With the high instantaneous and integrated luminosities of the LHC come two significant challenges for the detector. Firstly, as the instantaneous luminosity increases, so does the occupancy in the inner detector, calorimeters, and muon spectrometer, due to additional interactions in the same or neighbouring bunch crossings (*pile-up*). This requires that the sub-systems have short response times, hence the read-out electronics must be fast, and the granularity sufficiently fine to avoid degradation in resolution. Another challenge that comes with high luminosity is the large amount of radiation; both primary radiation from the interactions of the beam particles, and secondary radiation from the materials in the detector. The inner detector and the forward regions are particularly exposed, and radiation can damage the silicon detectors (pixel and silicon microstrip sub-detectors) and read-out electronics, cause ageing in wire detectors (such as the transition radiation tracker and the muon chambers), and change the logical state of electronic signals. To tackle these problems, a combination of shielding and materials robust to radiation are used. The design lifetime of the experiment is limited to ten years due to the effects of radiation damage.

4.1.2 Inner detector

The inner detector provides pattern recognition and momentum measurements for tracks from charged particles, where the transverse momentum (p_{T}) threshold for individual tracks can be as low as 0.1 GeV [60]; determination of the primary interaction vertex (defined as the vertex with the highest $\sum p_{\mathrm{T}}^2$ of all associated tracks), as well as vertices from pile-up [61] and secondary vertices from τ-lepton and b-quark decays. The tracking resolution is designed to be $\sigma_{p_{\mathrm{T}}}/p_{\mathrm{T}} = 0.05\,\%/p_{\mathrm{T}} \oplus 1\,\%$.

The inner detector is shaped as a cylinder with a length of about 3.5 m and a radius of about 1.2 m, and is immersed in a 2 T magnetic field from the superconducting solenoid (see Section 4.1.6). It consists of three independent sub-detectors. Closest to the beam pipe sits the pixel sub-

detector, which is arranged in four layers in the barrel and three disks in each of the end-caps. The barrel layer closest to the beam pipe is the insertable *b*-layer (IBL) [62, 63], which is part of the detector upgrade for Run 2. Further away from the beam pipe is the silicon microstrip (SCT) sub-detector, which is arranged in four cylindrical layers in the barrel and nine disks in each end-cap. The transition radiation tracker (TRT) contains *straw tube detectors* in up to 73 layers in the barrel, and 160 planes in each end-cap. Figure 4.2 shows a cut-away drawing of the inner detector.

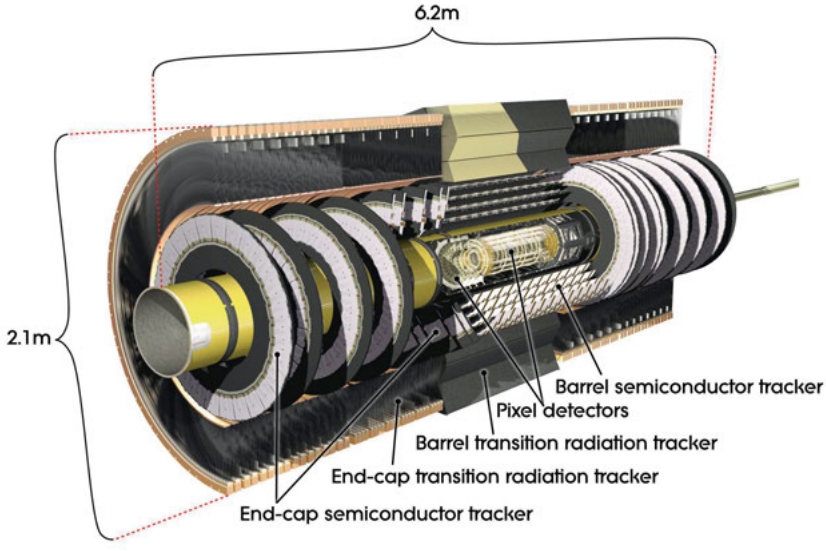


Figure 4.2. Cut-away drawing of the ATLAS inner detector.

The construction of the inner detector is tightly constrained to minimize the material budget. Spatially it must fit inside the solenoid and considerations must also be given to the placement and size of the calorimeters and the muon spectrometer. A power (or temperature) budget must also be respected. As the silicon sensor modules deteriorate from radiation damage, their leakage currents increase. The heat dissipated inside the entire inner detector is projected to be at least 40 kW, and requires a stable and sufficient cooling system. Against the minimizing constraints on the budget stand the requirement for mechanical stability and the requirement of high tracking granularity to compensate for the extreme pile-up conditions. The inner detector weighs about 4.5 tonnes in total, and the distribution of material is expected to have a large impact on some particles: electrons losing some of their energy through bremsstrahlung; photons undergoing e^-e^+ conversions before reaching the electromagnetic

calorimeter (see Section 4.1.3); and low-energy charged pions undergoing inelastic hadronic scattering.

The mechanical support, cooling, and electronics of the inner detector are only briefly mentioned in the following. More information about these topics can be found in Ref. [42].

Pixel

The pixel sensors are double-sided n-type silicon detectors with a thickness of 250 µm. To reduce the leakage current, the sensors are operated at temperatures between −5 °C and −10 °C. The sensor material is highly oxygenated as this has proven to yield better robustness against radiation of charged hadrons.

There are 1744 identical pixel sensors of dimension 19 mm × 63 mm. Each module has 46080 read-out channels, for a total of approximately 40.8 million channels. The pixel size is 50 µm × 400 µm, except in the interchip regions (50 µm × 600 µm). The modules in the innermost layer as well as the IBL must be replaced after about three years of operation under the design luminosity, while modules in the two outer layers are expected to last for the lifetime of the experiment.

SCT

The SCT sensors are single-sided n-type silicon detectors with p-type implants and a thickness of about 285 µm. Each SCT module consists of two pairs of sensors of strips radially rotated by 40 mrad to provide stereoscopic information. The strips in the barrel are parallel with a 80 µm pitch, while in the end-cap disks, they are radially distributed with a constant azimuthal angle and a mean pitch of about 80 µm. Each SCT module has 768 active strips. There are 2112 SCT modules in the barrel, and 1976 divided between the two end-caps. The number of read-out channels in the SCT is approximately 6.3 million.

TRT

The TRT straw tubes are 4 mm thick and 144 cm (37 cm) long drift tubes in the barrel (end-caps) made of polyimide, with a 31 µm gold plated tungsten wire as the anode, and filled with a $XeCO_2O_2$ gas mixture. The total number of read-out channels for the TRT is approximately 351 000.

Low-energy photons from transition radiation are absorbed by the xenon, and therefore yield a much larger signal in the straw tube than the minimum-ionizing signal from charged particles traversing the detector. By using different thresholds in the front-end electronics for each straw, it is possible to identify transition radiation from electrons.

Charged particles with $p_{\mathrm{T}} > 0.5\,\mathrm{GeV}$ produce hits in at least 22 straws in the transition region between the barrel and end-cap TRT detectors

$(0.8 < |\eta| < 1.0)$, while in the majority of the $|\eta| < 2.0$ region, the minimum number of hits is 36. The continuous tracking offered by the TRT thus improves the pattern recognition capabilities and the momentum resolution of the inner detector. Electrons with energies above 2 GeV typically yield 7-10 transition radiation hits, providing electron identification information complementary to that from the calorimeters (see Section 4.2).

4.1.3 Calorimeters

The calorimeters are constructed using different materials and use various techniques optimized to cover a wide range of physical processes over the range $|\eta| < 4.9$. They are sampling calorimeters, meaning that they consist of both passive (absorbers) and active material, where the energy deposited in the active material yields a signal that is representative for the total deposited energy. Nearest the inner detector, a calorimeter using liquid argon (LAr) as the active material and lead as the absorber provides electromagnetic calorimetry in the barrel. Around it as well as in the *extended barrel*, scintillating tiles are used as the active material for hadronic calorimetry, with steel plate absorbers. In the end-caps and the forward region $(3.2 < |\eta| < 4.9)$, LAr is used as the active material for both electromagnetic and hadronic calorimetry, while copper or tungsten are used as absorbers. Figure 4.3 shows a cut-away drawing of the barrel and end-cap calorimeters.

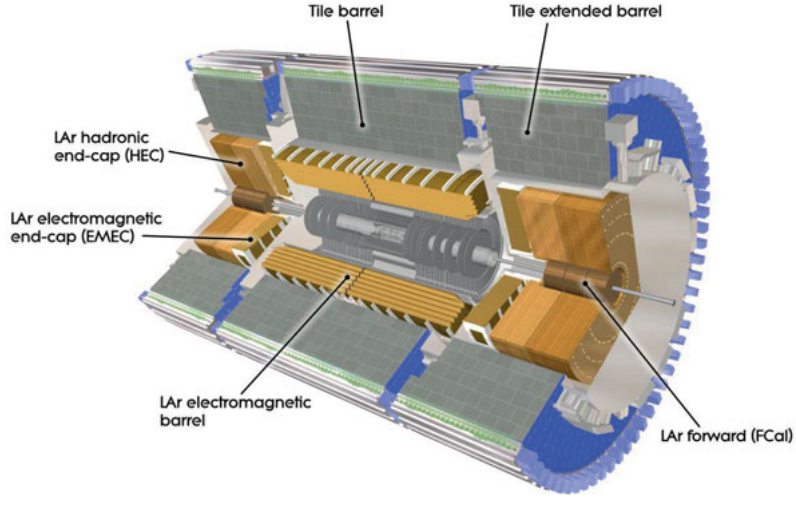


Figure 4.3. Cut-away drawing of the ATLAS barrel and end-cap calorimeters.

The main purposes of the calorimeters are to provide identification and energy measurements for electrons, photons, hadronic jets from b-, c-, and light quarks, as well as from hadronically decaying τ-leptons, and to provide triggering on these objects. The almost-full coverage in η is essential to capture the full energy of a collision, and in turn to correctly reconstruct the missing transverse energy ($E_{\mathrm{T}}^{\mathrm{miss}}$) in the events. For a detailed overview of particle identification and reconstruction in the ATLAS detector, see Section 4.2, while triggering is treated in Section 4.3.

Contrary to the inner detector, the main requirement on the calorimeters is that they must be sufficienty thick to completely capture the energy of electrons, photons, and hadrons, and prevent particles from punching through into the muon spectrometer. The thickness of the calorimeters corresponds to at least 22 radiation lengths (X_0) for the electromagnetic calorimeters and approximately 10 interaction lengths (λ) in the hadronic calorimeters[1].

Electromagnetic calorimeters

The electromagnetic calorimeters consist of a barrel part with three layers, covering $|\eta| < 1.475$, and two end-caps covering $1.375 < |\eta| < 3.2$. The end-cap calorimeters are further divided into two wheels, where the innermost wheel covers the range $2.5 < |\eta| < 3.2$ and has two layers, while the outermost wheel covers the high-precision part of the end-cap ($1.375 < |\eta| < 2.5$). The calorimeter parts in the high-precision region have the finest granularity. A presampler is installed closest to the inner detector, in the range $|\eta| < 1.8$, to correct for energy losses by electrons and photons in the material upstream (the inner detector and the solenoid).

The electromagnetic calorimeter in the barrel has an accordion geometry, which allows full coverage in ϕ without cracks as illustrated by the left-hand plot of Figure 4.4. The first layer has the finest segmentation in η to precisely determine the location of the head of the electromagnetic shower. The largest amount of energy is absorbed by the middle layer, and the third layer captures the tails of the electromagnetic shower and has a coarser segmentation. The barrel is made of two halves, each 3.2 m long and weighing 57 tonnes. The inner and outer diameters of the electromagnetic barrel are, respectively, 2.8 m and 4 m. Each half is made out of 1024 absorbers, interleaved with gaps for the LAr active medium and the electrodes. The presampler is a separate 11 mm thick LAr layer that sits inside the barrel.

[1] The radiation length (X_0) is the average distance over which a high-energy electron looses all energy but $1/e$, and, simultaneously, 5/9 of the mean free path for e^+e^- pair-production by a high-energy photon. The nuclear interaction length (λ) is the mean free path between nuclear interactions by high-energy hadrons.

The end-cap electromagnetic calorimeters are approximately 2 m in diameter and 0.6 m thick, each weighing 27 tonnes. The amount of material in front of the calorimeter is largest in the region $1.5 < |\eta| < 1.8$, and here also the end-cap calorimeter is supplemented by a presampler.

The number of read-out channels are around 102 000 (8000) for the electromagnetic calorimeter (pre-sampler) in the barrel, while for both end-caps they amount to 62 000 (1500).

The energy resolution (σ_E/E) is measured to be $10\,\%/\sqrt{E} \oplus 0.17\,\%$, in the range 10–245 GeV. The position resolution is measured to be 1.5×10^{-4}–3.3×10^{-4} in η.

Hadronic calorimeters

The hadronic calorimeters consist of the tile calorimeter, covering $|\eta| < 1.7$, and two hadronic end-cap calorimeters, covering $1.5 < |\eta| < 3.2$.

The tile calorimeter consists of a 5.8 m long central barrel, and two 2.6 m long extended barrels. It is located outside the barrel electromagnetic calorimeter, and has an inner radius of 2.28 m and an outer radius of 4.25 m. Each barrel consists of 64 wedge shaped modules of size 5.625° in ϕ, as illustrated by right-hand plot of Figure 4.4. Between each module, at the inner radius, is a 1.5 mm gap in the azimuthal direction. The support structure at the outer radius of each module is a steel girder, which also contains the photo-multiplier tubes and read-out electronics, as well as the flux return for the magnetic field in the inner detector (see Section 4.1.6). The absorber structure consists of 5 mm steel plates that form the shell of the module, and 4 mm steel plates used as spacing between each pair of scintillating tiles.

The active medium of the tile calorimeter is scintillating polystyrene tiles of 3 mm thickness, 97–187 mm radial length, and 200–400 mm azimuthal length. Optical fibres transmit the scintillation light to the photo-multiplier tubes located in the girder, where it is transformed to electrical signals. Each tile has two edges, connected to two different photo-multiplier tubes to normalize signals depending on where in the tile a particle has hit, and for redundancy.

The tiles are organized into cells in three radial layers, where the cells have the dimensions 0.1×0.1 and 0.2×0.1 in $\eta \times \phi$ for the first two and the third layers, respectively. The number of read-out channels is 5760 in the central barrel, and 4092 in total in the two extended barrels. The energy resolution has a significant dependence on η due to the difference in interaction lengths. For $|\eta| = 0.35$, the fractional energy resolution has been measured with a test beam of pions to be $50\,\%/\sqrt{E} \oplus 5.5\,\%$, in the energy range 20–350 GeV.

The hadronic end-cap calorimeters consist of two wheels of radius 2 m each. The active medium is LAr, with lead as the absorbing material. They are partitioned into read-out cells of size 0.1×0.1 in $\eta \times \phi$ for

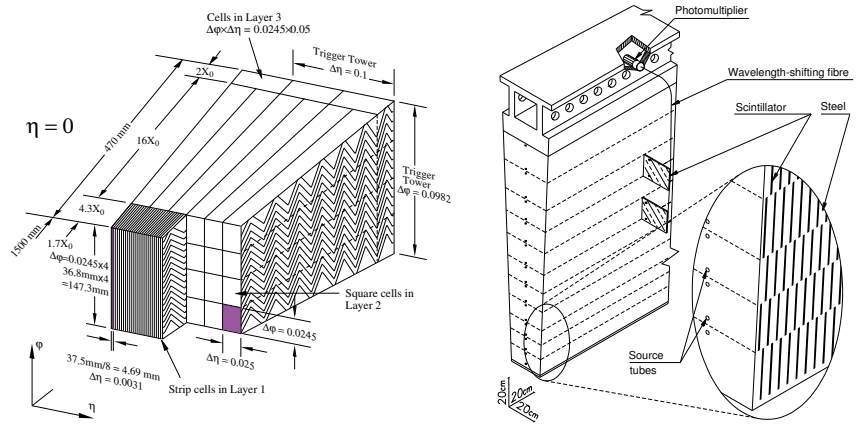


Figure 4.4. Drawing of a barrel module of the electromagnetic LAr calorimeter, showing the three layers and the accordion shape (left) and schematic of a barrel module in the tile calorimeter (right). The schematic of the tile calorimeter module shows the relative placement of the scintillating tiles and the absorber plates, as well as wavelength-shifting fibres, the photo-multiplier tubes, and the girder.

$|\eta| < 2.5$, and 0.2×0.2 up to $|\eta| = 3.2$, with a total of 5632 cells. The energy resolution was measured to be $71\,\%/\sqrt{E} \oplus 6\,\%$.

Forward calorimeter

The forward calorimeters cover the region $3.1 < |\eta| < 4.9$, and their fronts are placed about 1.2 m beyond the fronts of the hadronic end-cap calorimeters. They thus have a limited depth and therefore more stringent requirements on density. The forward calorimeters consist of three layers, each made out of a 0.45 m long module. The first layer uses copper for the absorber and is optimized for electromagnetic interactions, while the last two use tungsten and are optimized for hadronic interactions. The forward calorimeters on both sides have a total of 3524 read-out channels. Their energy resolution has been measured with test beams of electrons and pions to be $29\,\%/\sqrt{E} \oplus 3.5\,\%$ and $70\,\%/\sqrt{E} \oplus 3\,\%$, respectively.

4.1.4 Muon spectrometer

The muon spectrometer is designed for tracking of and triggering by (see Section 4.3) charged particles that are not stopped by the calorimeters. The tracking operates in the region $|\eta| < 2.7$ and triggering in the region $|\eta| < 2.4$. The muon spectrometer consists of four sub-detectors. The Monitored Drift Tubes (MDT) provide precision tracking in the bending plane in the range $|\eta| < 2.7$. The first layer of the MDT is replaced by

Cathode Strip Chambers (CSC) in the region $2.0 < |\eta| < 2.7$. Triggering and measurement of the ϕ-coordinate is provided by Resistive Plate Chambers (RPC) in the region $|\eta| < 1.05$, and Thin Gap Chambers (TGC) in $1.05 < |\eta| < 2.7$ ($|\eta| < 2.4$ for triggering). Figure 4.5 shows a cut-away drawing of the muon spectrometer.

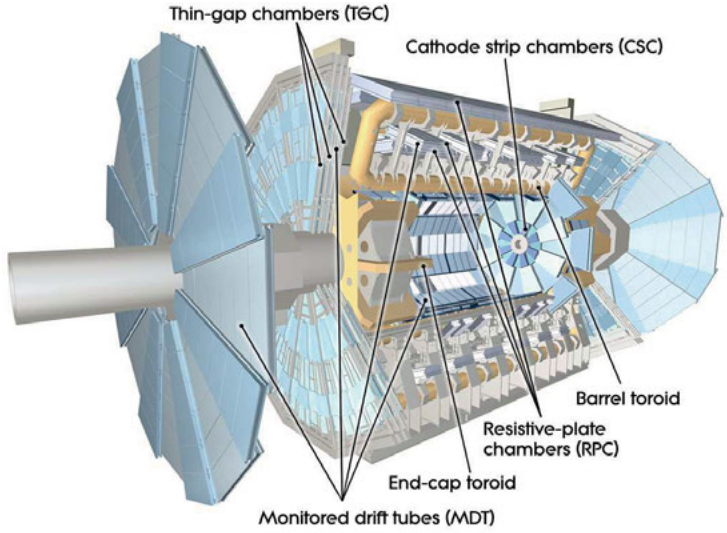


Figure 4.5. Cut-away drawing of the ATLAS muon spectrometer.

The resolution for a measurement where only the muon spectrometer is involved is about 10 % for a track with a p_{T} of 1 TeV. This translates into a resolution requirement along the z-axis of about 50 µm. The muon spectrometer provides momentum measurement and charge identification from about 3 GeV up to about 3 TeV, which means that the the relative alignment of the tracking chambers must be known to an accuracy of about 30 µm.

By matching the hits in the bending plane between the precision chambers (MDT and CSC) and trigger chambers (RPC and TGC), the measurement of η from the precision chambers can be combined with the measurement of ϕ from the trigger chambers.

The magnetic field for the muon spectrometer is provided by eight superconducting toroid coils in the barrel, and two end-cap toroids (see Section 4.1.6). To correctly and precisely determine the momentum of muons through the bending of their tracks, it is necessary to know the magnetic field down to the per mille level. This is achieved through about 1800 Hall sensors that are distributed throughout the spectrometer.

4.1.5 Forward detectors

There are three detectors in the forward region of ATLAS. LUCID (LUminosity measurement using Cherenkov Integrating Detector) is a relative luminosity detector, which measures inelastic pp scattering in the forward direction. It is used to measure the integrated as well as instantaneous luminosity, and acts as an online monitor of beam conditions. The ALFA (Absolute Luminosity For ATLAS) detector measures elastic Coulomb scattering at very small angles (3 µrad). It requires special beam conditions (high β^* and reduced beam emittance), and results from ALFA can be used to calibrate LUCID. Finally, the ZDC (Zero-Degree Calorimeters) are used to detect neutrons in the forward region with $|\eta| > 8.3$ in heavy-ion collisions, in order to determine the centrality of such collisions.

4.1.6 Magnet system

The ATLAS magnet system consists of two parts: a central solenoid placed between the electromagnetic calorimeter and the inner detector, and a system of eight barrel and two end-cap toroids housed inside the muon spectrometer.

The superconducting solenoid provides bending of charged particles in the inner detector through an axial magnetic field of 2 T. The magnetic flux is returned through the steel girder of the barrel hadronic calorimeter. The support structure for the central solenoid consists of a 12 mm thick aluminium cylinder. The coil is made of NbTi/Cu and strengthened with aluminium, and it is wound in a single layer inside the support cylinder. The LAr calorimeters share the vacuum vessel with the solenoid, in order to minimize the amount of material in front of them. The solenoid contributes to about 0.66 X_0 at an incidence normal to the beam axis. The length of the solenoid is 5.4 m, its inner diameter is 2.46 m, its thickness is 0.1 m, and it weighs 5.4 tonnes. The peak magnetic field of the solenoid is 2.6 T, and the stored energy is 40 MJ.

The barrel toroid is a system of eight superconducting coils that provide bending of charged particles in the volume of the muon spectrometer through a toroidal magnetic field of approximately 0.5 T. It extends over 25.3 m in length, has inner and outer diameters of 9.4 m and 20.1 m respectively, and weighs about 830 tonnes. The coils are made of the same material as the solenoid coil. They have a core of air and are contained in vacuum vessels of stainless steel. The operating temperature of the barrel toroid is 4.6 K. The peak magnetic field of the barrel toroid is 3.9 T, and the stored energy is 1.1 GJ.

The end-cap toroids complement the barrel toroid in the high-η region by providing extra bending power through a magnetic field of about 1 T. Each end-cap toroid consists of eight flat, square coils and eight wedges,

in order to support the structure against the considerable Lorentz force which the toroid is subject to under operation. The end-cap toroids are made of the same superconducting material as the barrel toroids, and they share the operating temperature. Each end-cap toroid weighs 239 tonnes, is 5 m in length, and has inner and outer diameters of 1.65 m and 10.7 m respectively. The peak magnetic field is 4.1 T, and the stored energy is 0.25 GJ per toroid.

4.2 Particle reconstruction and identification

Particles arising from *pp* collisions yield different responses in the various sub-detectors depending on their type. Figure 4.6 shows a representation of how particles of different types interact with the ATLAS detector. The particle reconstruction and identification is described here with respect to the ATLAS detector in Run 2.

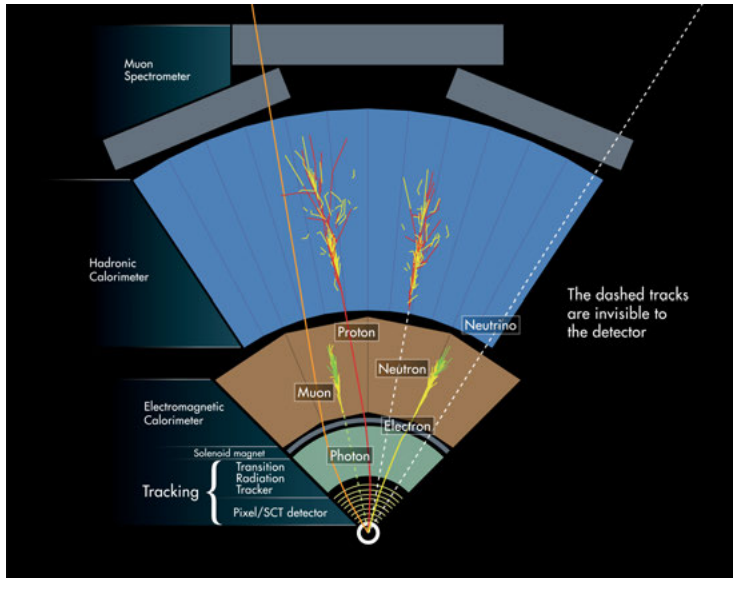


Figure 4.6. Representation of how particles of different types are detected in the ATLAS detector.

4.2.1 Electrons

Electrons are *seeded* by projective regions in η and ϕ (*towers*) in the electromagnetic calorimeter [64]. A clustering algorithm [65] is used to form clusters of towers in the electromagnetic calorimeter around the seed, and to remove duplicate clusters.

Track seeds are formed by hits in the silicon detectors, and are fitted to tracks using pattern recognition algorithms [66, 67]. The track fitting algorithms take the effects from bremsstrahlung into account. The tracks are matched to the electromagnetic clusters based on the distance in η and ϕ. If multiple tracks can be matched to a cluster, the one closest in ΔR is considered as the primary track. Electromagnetic clusters without a matched track are considered as photons (see Section 4.2.2). The acceptance is restricted to the range $|\eta| < 2.37$, with the transition region between the barrel and end-cap electromagnetic calorimeters ($1.37 < |\eta| < 1.52$) excluded.

The energy of the cluster is calibrated to the true electron energy using multi-variate analysis (MVA) techniques based on simulation [68]. Electron isolation is measured for both tracks and clusters, and is based on the sum of energies from tracks or clusters, respectively, in a cone around the electron direction.

An MVA technique called the likelihood-based (LH) method is used to distinguish electrons from converted photons or charged pions [64]. It uses the probability density functions (PDF) of variables that have different shape for electrons and backgrounds. Electrons are more likely to deposit all of their energy in the electromagnetic calorimeter as compared to hadrons, which makes *leakage* into the hadronic calorimeters a powerful discriminator. The number of hits in the IBL discriminates against photon conversions, and the amount of transition radiation detected by the TRT discriminates electrons from charged hadrons. Other variables are related to the shape of the cluster in the different layers of the electromagnetic calorimeter, and to the associated tracks. Three working points (*loose*, *medium*, and *tight*) define different pairs of values of signal efficiency and background rejection power.

4.2.2 Photons

A cluster of energy (formed as in Section 4.2.1) is considered as an *unconverted* photon if it has no associated track, and as a *converted* photon if it has two oppositely charged tracks that are collinear and compatible with electrons based on information from the TRT [69]. A cluster with only one associated track can also be considered as a converted photon if it has no hit in the IBL.

The acceptance is restricted to the range $|\eta| < 2.37$ (with $1.37 < |\eta| < 1.52$ excluded) where the first high-granularity (strip) layer of the electromagnetic calorimeter has fine enough segmentation to reject neutral hadrons (e.g. $\pi^0 \to \gamma\gamma$ decays). The photon identification algorithm employs cuts on discriminating variables to select signal photons, and reject

backgrounds. Among them are variable describing the cluster shape, and leakage into the hadronic calorimeters.

Track- and cluster-based isolation variables similar to those described in Section 4.2.1 can be used to discriminate photons originating from the hard interaction from background photons.

4.2.3 Muons

Muon reconstruction is done separately in the inner detector and the muon spectrometer. Then, information from the two reconstructions is combined to form muon candidates for physics analyses [70].

Tracks in the inner detector are formed from hits in its sub-detectors, with a similar procedure as that described in Section 4.2.1. In the muon spectrometer, track segments are formed from hits in each sub-detector layer. A combinatorial algorithm forms track candidates with segments in the middle MDT layer as seeds, and then adding segments from the inner and outer layers. In the case of overlapping tracks, the candidate with the best segment alignment is selected.

The information from the inner detector, muon spectrometer, and the calorimeters are used to reconstruct four types of muons. Combined and extrapolated muons are the default for physics analyses, and are described here, while the other two types are segment-tagged and calorimeter-tagged muons. Combined muons are reconstructed from a refit of the hits the inner detector and the muon spectrometer. Extrapolated muons are reconstructed from a track in the muon spectrometer that is compatible with the interaction point, and are used to extend the muon coverage outside the inner detector ($2.5 < |\eta| < 2.7$). If several types of muons overlap, priority is given in the order combined, segment-tagged, calorimeter-tagged, and extrapolated.

Identification criteria for muons are aimed at suppressing backgrounds mainly from decays of pions and kaons. Muons originating from charged-hadron decays in the inner detector result in a poorer track fit quality. Incompatibilities between the momentum measurements of inner detector and muon spectrometer tracks can also be used.

4.2.4 Jets

Jets are usually reconstructed [71] using the anti-k_t [72] algorithm with a distance parameter of $R = 0.4$. Topological clusters are formed from groups of calorimeter cells that follow the evolution of the shower as a jet enters the calorimeters, and are used as inputs to the reconstruction. The energy of a topological cluster is defined as the sum of energies of each cell belonging to that cluster, and the direction is calculated from

weighted averages of η and ϕ of these cells. Energy calibration is performed by removing the average contribution from pile-up interactions, and then applying an energy- and η-dependent response function derived from simulation [73].

Timing variables are used to separate jets from the collision from those originating from beam gas, beam halo events, or cosmic rays. Pulse-shape variables are used to effectively reject jets due to calorimeter noise. An MVA technique called the jet vertex tagger (JVT) [74] is used to distinguish jets from the hard interaction from pile-up jets.

4.2.5 τ-leptons

The τ-leptons have a short decay time, and can only be detected through their decay products. Leptonic decays of τ-leptons are reconstructed in the same way as prompt electrons (Section 4.2.1) or muons (Section 4.2.3). Hadronic decays of τ-leptons are the main focus of this thesis, and are used to measure the performance of the τ trigger (Section 5.3.6), to determine the Higgs boson coupling to fermions in the $H \to \tau\tau$ analysis (Section 6.2), and to search for charged Higgs bosons in $H^+ \to \tau\nu$ decays (Section 6.3). The descriptions of the reconstruction, identification, and energy calibration of hadronically decaying τ-lepton candidates (τ_{had}) are deferred to Chapter 5.

4.2.6 Flavour tagging

Identification of jets originating from hadrons containing b- or c-quarks is important in many analyses, including the τ trigger performance measurement using top–antitop-quark pairs ($t\bar{t}$) events in Section 5.3.6 and the charged Higgs boson search in Section 6.3. Flavour tagging, or $b(c)$-tagging, depends on specific properties of $b(c)$-hadrons. They include the long lifetime, high mass, and decay particle multiplicity in b-hadrons, as well as the difference in fragmentation of the b-quark compared to its lighter counterparts.

The output of three algorithms are used as input to a boosted decision tree (BDT) algorithm [75, 76]. The first algorithm is based on the impact parameter of the tracks associated with the jet. The second algorithm tries to reconstruct a secondary vertex, which is displaced from the primary vertex. The third algorithm, called the JetFitter algorithm, tries to exploit the topology of weak decays of $b(c)$-hadrons by reconstructing the full decay chain.

The multi-variate algorithm MV2 uses the outputs from the three basic algorithms as input to discriminate b-jets from light and c-jets. The MV2 algorithm is trained with $t\bar{t}$ simulated events, where true b-jets are defined

as a signal while a mixture of light/c-jets constitute the background. The default training for the 2016 data taking is called MV2c10, and uses a mixture of 90 % b-jets and 10 % c-jets. Four working points with different b-tagging efficiencies are defined: 60 %, 70 %, 77 %, and 85 %.

4.2.7 Overlapping objects

Object reconstruction allows for multiple objects to be reconstructed from the same signals in the detector. Such objects will have a geometrical overlap within some distance ΔR. The most prominent examples of overlapping objects are between electrons, τ_{had} candidates, and jets, because they produce similar signatures in the calorimeters. Despite efforts to correctly identify from what object a signature comes, different requirements in different analyses might not allow for a unique decision. To resolve ambiguities between overlapping objects, after a selection has been made on the quality of the reconstructed objects, a procedure called *overlap removal* is used.

Overlap removal is done by removing geometrically overlapping objects in a defined priority. Two objects are said to overlap if they are separated by a distance ΔR less than a given cut value, typically 0.1–0.4 depending on the object. A common priority for analyses is to:

1. keep all selected muons,
2. iteratively remove selected electrons that overlap with muons,
3. iteratively remove selected τ_{had} candidates that overlap with muons or electrons,
4. iteratively remove selected jets that overlap with muons, electrons, or τ_{had} candidates.

A looser selection is commonly used for the objects against which overlap is checked. For instance, an analysis using medium electrons and medium muons might require that the electrons do not overlap with loose muons.

4.2.8 Missing transverse energy

By construction of the coordinate system of the detector, colliding particles only have momentum in the longitudinal direction. Hence, the momenta of all particles from a collision must sum up to zero in the transverse direction. Deviations occur either when there are undetectable particles in the event, such as neutrinos or other weakly interacting particles, or when normally detectable particles escape detection or are incorrectly measured. The overall imbalance in p_{T} is called missing transverse momentum, and is described by its magnitude ($E_{\text{T}}^{\text{miss}}$) and its direction in the transverse plane (ϕ^{miss}).

$E_{\mathrm{T}}^{\mathrm{miss}}$ is a key component in the searches for both the charged Higgs boson and the Higgs boson decaying into two τ-leptons that are described in Chapter 6. $E_{\mathrm{T}}^{\mathrm{miss}}$ is a significant part of the signature of the $H^+ \to \tau\nu$ process, and it is used to trigger these events. In $H \to \tau\tau$ events, $E_{\mathrm{T}}^{\mathrm{miss}}$ is used to reconstruct the Higgs boson mass using the missing mass-calculator (MMC) technique [77].

Undetectable particles coming from the hard interaction cause *true* $E_{\mathrm{T}}^{\mathrm{miss}}$, while pile-up interactions can cause real imbalances from undetectable particles, and apparent imbalances through reconstruction inefficiencies. Apparent imbalances can also occur if particles from the hard interaction fail to deposit all their energy in the calorimeters, are not efficiently reconstructed by the inner detector and the muon spectrometer, or when they pass through areas where the detector has no or limited coverage.

The $E_{\mathrm{T}}^{\mathrm{miss}}$ is calculated from the negative of the summed p_{T} of all reconstructed objects in the event [78, 79]. It is computed separately for each object and for each cartesian component:

$$\begin{aligned} E_{x(y)}^{\mathrm{miss}} = {} & E_{x(y)}^{\mathrm{miss},e} + E_{x(y)}^{\mathrm{miss},\gamma} + E_{x(y)}^{\mathrm{miss},\tau} + E_{x(y)}^{\mathrm{miss},\mu} + \\ & E_{x(y)}^{\mathrm{miss,jets}} + E_{x(y)}^{\mathrm{miss,soft}}. \end{aligned} \tag{4.1}$$

The soft term ($E_{x(y)}^{\mathrm{miss,soft}}$) can be computed either from tracks or calorimeter deposits not associated with reconstructed objects. The default is the track-based soft term, which uses tracks associated with the primary vertex and is robust against contributions from pile-up [80].

4.3 Trigger and data acquisition

The ATLAS TDAQ system is responsible for selecting events that are potentially interesting for physics analyses, reading event data from the detector electronics, and permanently storing selected events. It is described in detail in Refs. [59, 81]. The trigger system consists of a Level-1 (L1) trigger, which is implemented in hardware and closely integrated with the detector read-out electronics, capable of making a decision within 2.5 µs, and a High-Level Trigger (HLT), which is implemented in software and runs on a computer farm with more than 30 000 cores.

4.3.1 Level-1 trigger

The L1 trigger selects events with signatures from muons, electrons, photons, jets, and hadronically decaying τ-leptons with high p_{T}, and, optionally, isolation criteria. The L1 trigger also selects events which contain large amounts of energy, or have a large $E_{\mathrm{T}}^{\mathrm{miss}}$.

Information from the calorimeters and the trigger chambers of the muon spectrometer are used for the L1 trigger decision. This information is at a lower granularity than what is eventually read out if the event is selected. The L1 trigger also defines Regions-of-Interest (RoI) which the HLT uses to make a more careful decision.

The L1 trigger must be able to identify the bunch crossing in which a trigger item was fired. Due to the size of the detector, the bunch crossing interval of 25 ns is much smaller than the travel time for electrical signals to the L1 trigger processors. Pipeline memories are used to buffer the read-out signals, and these place a constraint on the time from the bunch crossing to the L1 trigger decision. The maximum output rate of the L1 trigger to the HLT is 100 kHz.

The L1 τ and $E_{\mathrm{T}}^{\mathrm{miss}}$ trigger algorithms are described in detail in Ref. [82] and are summarized here. The L1 τ trigger uses deposited energy in towers in the calorimeter, and defines a RoI based on a local energy maximum among the towers. The towers around the RoI are called the isolation region, and an upper threshold is applied on the energy deposited in them. Figure 4.7 illustrates the RoI and the isolation regions used in the L1 τ trigger algorithm. The L1 $E_{\mathrm{T}}^{\mathrm{miss}}$ trigger uses sums of deposited energy in towers in the calorimeter, together with their location, to compute the x and y components of the $E_{\mathrm{T}}^{\mathrm{miss}}$.

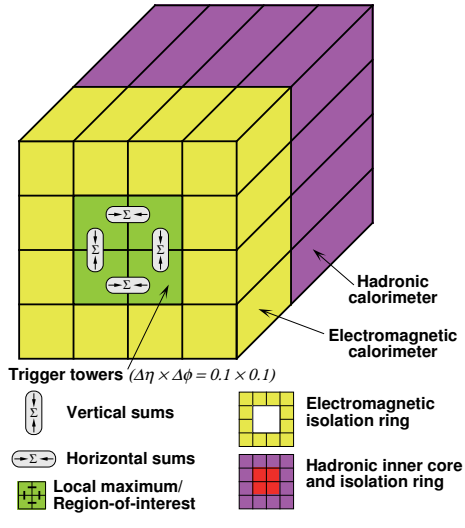


Figure 4.7. Illustration of how combinations of trigger towers are used in the τ trigger algorithm.

4.3.2 High-Level Trigger

The HLT runs reconstruction and identification algorithms, in order to find event properties that match a list of physics signatures. These signatures can be object candidates (electrons, photons, muons, τ_{had}, jets, and b-jets), topological features, or global event properties (total transverse energy and $E_{\text{T}}^{\text{miss}}$). Its purpose is to decide whether an event should be rejected or accepted for final storage.

The HLT first uses the information gathered from the L1 RoIs at full granularity, corresponding to about 10 % of the total event data. As the HLT proceeds, more information about the event needs to be reconstructed. Rejection of a specific signature occurs as early as possible, and as soon as no viable signatures remain, the whole event is rejected. The HLT is designed to process events at a rate of 100 kHz, with a maximum output rate of 1 kHz.

τ trigger

The τ trigger is one of the focuses of this thesis. Its performance is measured in the analyses described in Section 5.3, where the efficiencies in $Z \to \tau\tau$ and $t\bar{t}$ events are studied. Furthermore, the two-object τ trigger is used in the $H \to \tau\tau$ analysis described in Section 6.2. The τ trigger is described in detail in Refs. [59, 83], and is only summarized here.

In the initial stages, the τ trigger uses information from the calorimeters and about tracks in the inner detector, in the RoI. The transverse momentum is computed from calorimeter cells, while tracking is performed in two steps, with increasing precision and requirement on computing times. After this initial reconstruction, a selection based on track isolation is applied to reject backgrounds.

Full reconstruction of the τ_{had} candidate is done at a later stage, using the anti-k_t algorithm within the RoI. The BDT algorithm described in Section 5.2.2 is used to reject jets.

$E_{\text{T}}^{\text{miss}}$ trigger

Five different algorithms, with various levels of complexity, have been developed for the $E_{\text{T}}^{\text{miss}}$ trigger. The algorithms use information from calorimeter cells, topological clusters, or reconstructed jets. The topological-cluster-based algorithm is also complemented with two different methods for correcting the effects from pile-up. The $E_{\text{T}}^{\text{miss}}$ trigger is described in detail in Ref. [59].

The $H^+ \to \tau\nu$ search, described in Section 6.3, uses the $E_{\text{T}}^{\text{miss}}$ trigger with the jet-based algorithm for 2016 data, and the topological-cluster-based algorithm for 2015 data. The trigger efficiency is measured in data and applied to simulated events.

4.3.3 Data acquisition

The ATLAS data acquisition system is responsible for transporting and assembling all data, starting from the front-end electronics inside each sub-detector, through the sub-detector read-out drivers, via the read-out system, which buffers the data until requested by the HLT, and, finally, storing the events that fire the HLT to disk.

4.4 Computing and data model

4.4.1 The LHC computing model

The Worldwide LHC Computing Grid (WLCG), commonly referred to as the Grid [84], provides the computing model to ATLAS and the other experiments at the LHC. The Grid is a global collaboration, involving about 170 computing centres worldwide. It is divided into four levels [85], where for ATLAS the Tier-0 is the CERN data centre and an off-site centre located in Hungary. The Tier-0 centre is responsible for storing the raw data from the experiments and redistributing data to the 13 Tier-1 centres, one of which is the NDGF centre run by Sweden, Norway, and Denmark. They have a shared responsibility of storing raw and reconstructed data, and are also used to perform large-scale reprocessing and simulation tasks. They redistribute data to the numerous Tier-2 centres, which are typically universities and other scientific institutes. The Tier-2 centres are responsible for running the bulk of the analysis jobs launched by individual scientists and groups, and also proportionally share the production of simulated events. Tier-3 centres are local computing resources belonging to e.g. a university department. They have no formal engagement with the Grid, and usually restrict access to their members.

4.4.2 The ATLAS data model

Data

The raw data (RAW) from the event read-out is processed in two steps, resulting in two formats. The Event Summary Data (ESD) contain sufficient information to perform object identification, refitting of tracks, calibration of jets, etc. It is used for tuning reconstruction algorithms and calibrations. Analysis Object Data (AOD) contain the reconstructed events with reduced detail, and has enough information to perform most analyses.

Simulation

The production of simulated events (Monte Carlo, MC) start with the generation of the hard scattering of a physical process. This step is called

event generation and can be performed by a multitude of generator programs, e.g. POWHEG [86, 87], PYTHIA [88, 89], ALPGEN [90], and MADGRAPH [91].

The resulting EVNT files undergo detector simulation, using either the full simulation, with a GEANT4 [92] model of the detector, or ATLFAST-II [93], combining calorimeter simulation using FastCaloSim and the GEANT4 model for the inner detector. In the FastCaloSim calorimeter simulation, observables such as energy, momentum, and position are parametrized and smeared to give as realistic a response as possible without having to use the time consuming, detailed GEANT4 detector simulation. The simulation results in HITS files.

The next step involves adding the pile-up simulation and performing the digitization, in turn producing Raw Data Object (RDO) files. The trigger simulation is then performed, with a new set of RDO files as the output. These RDO files undergo the reconstruction process, resulting in ESD and AOD files, just as for data.

Analysis

The analysis data model, including both collision data and simulated events, starts from AOD files as the common data format. The AOD files may undergo several iterations of refinements, with respect to reconstruction and calibration. They can be used directly in analyses using either the ATLAS-specific Athena or the general ROOT [94] framework, but a more common workflow is to use one of the various Derived AOD (DAOD) formats.

The DAOD files are produced from AOD files with a derivation framework, where the file size is reduced through two methods. Skimming removes entire events that are not expected to be interesting in the given type of analysis, whereas slimming removes information that is not required from the remaining events.

A multitude of DAOD formats exist, targeting different physics analyses or object performance studies, which are produced and managed centrally. The size reduction minimizes the effect of event duplication across the different DAOD formats. The considerably smaller size of the DAOD files also result in faster execution of analysis jobs.

A last reduction step is usually performed on the DAOD files, which implements pre-selections for specific analyses, and can also produce outputs in different data formats. The final data analysis is usually done using the ROOT framework, and common formats include further skimmed and slimmed DAOD files, or ROOT files (flat ntuples).

4.4.3 ATLAS computing model

Roles of the tiers

The data from the HLT are distributed to the Tier-0, which stores the raw data. The typical event size for an average of 40 interactions per bunch crossing is 1 MB. With a HLT output rate of 1 kHz, the streaming throughput of raw data at Tier-0 is about 1000 MB/s. The Tier-0 in ATLAS performs a first event reconstruction on the RAW files, and produces files of the ESD and AOD formats. In case of serious congestion at Tier-0, the computing model allows for some of the RAW processing to be taken over by Tier-1 sites.

Tier-1 sites are responsible for keeping a second copy of the RAW data, and they are distinguished by being the sites where the most memory- and input/output-intense jobs are run. All central or communal workflows, such as reprocessing of data, production of simulated events, and group production, can be run on both Tier-1 and Tier-2 sites. This enables load and throughput optimization by allowing sites to run a mixture of job types in terms of input/output usage, memory consumption, and CPU load.

Other computing resources

At times when the HLT farm is not used for its main purpose, e.g. when there are no collisions in the LHC, it can be temporarily repurposed to act as a Grid site. This may also occur during collisions, to allow for efficient usage of the approximately 30 % of the farm that is idle.

In addition to Grid sites, ATLAS has also investigated the use of opportunistic resources, such as commercial or scientific cloud resources, or temporary resources at High Performance Computing (HPC) centres [95]. ATLAS has successfully used Infrastructure-as-a-Service (IaaS) cloud resources from Amazon EC2, Google Compute Engine (GCE), and Helix-Nebula. For the author's own work about using Puppet to contextualize computing resources on GCE, see Section 4.4.4.

ATLAS distributed computing environment

The ATLAS distributed computing environment consists of many parts, from the job definition interface to monitoring. JEDI (Job Execution and Definition Interface) is the system for defining, prioritizing, matching, and executing jobs. It provides the interface for running distributed analysis jobs using e.g. the `pathena` or `prun` programs. The DEfT (Database Engine for Tasks) is the interface used for larger tasks, such as the production of simulated events. PanDA is the system responsible for monitoring the status and manage the workflow of the jobs. It executes sub-jobs on computing resources using a pilot program.

Data management is handled by Rucio, which both end-users and resource administrators use to download, upload, copy, delete, and manage

datasets. When jobs run on a site, the input data can be either copied or accessed remotely. Remote access is provided via the HTTP protocol, or by XRootD through Federated XRootD Storage (FAX). The SRM and GridFTP programs are used for file transfers.

The different types and versions of softwares required to run ATLAS jobs on the Grid are distributed through a shared file system called CernVM-FS.

4.4.4 Cloud computing R&D

So-called Infrastructure-as-a-Service (IaaS) cloud services, where a user essentially rents a (virtual) computer for a period of time, have become increasingly popular over the past years. ATLAS experiences peaks in computing resource usage in times of hectic data analysis or large production campaigns. During these peaks, it may be beneficial to temporarily increase the amount of available computing resources. This can be done using IaaS cloud services, and with some monitoring, it can also be done opportunistically, i.e. using the resources at times when the cost is lowest.

Google Compute Engine (GCE) is an IaaS service run by Google. At the time of research, it was not possible to upload machine images to GCE, hence using images with the necessary software for ATLAS computing nodes pre-installed was not possible. The author has developed an alternative approach [96], where the contextualization of the machine is done on-the-fly as the machine starts.

The contextualization is performed using Puppet, a system administration software used to automate many administrative tasks. It uses declarative manifests to define the desired state of a system, and ensures that the system configuration does not drift from the said state. A set of Puppet *modules* have been created to install and configure the necessary software to run an ATLAS computing cluster on GCE.

The node configuration consists of one manager node and any number of worker nodes. The manager node runs AutoPyFactory for the creation of pilots, and retrieval of jobs from a PanDA queue, HTCondor for the job scheduling, and an XRootD redirector for data access through FAX. The worker nodes run CernVM-FS for accessing the software necessary to run ATLAS distributed analysis jobs. They also run HTCondor in a node capacity to be able to accept jobs from the scheduler, and XRootD as a file access and cacheing service. Figure 4.8 shows a schematic of a cluster configuration on GCE, and a schematic of the contextualization of a node.

The time needed for a bare instance to become a fully configured node suitable for running ATLAS distributed analysis jobs has been measured to 5-7 minutes. The instantiation of nodes can be done in parallel, and it

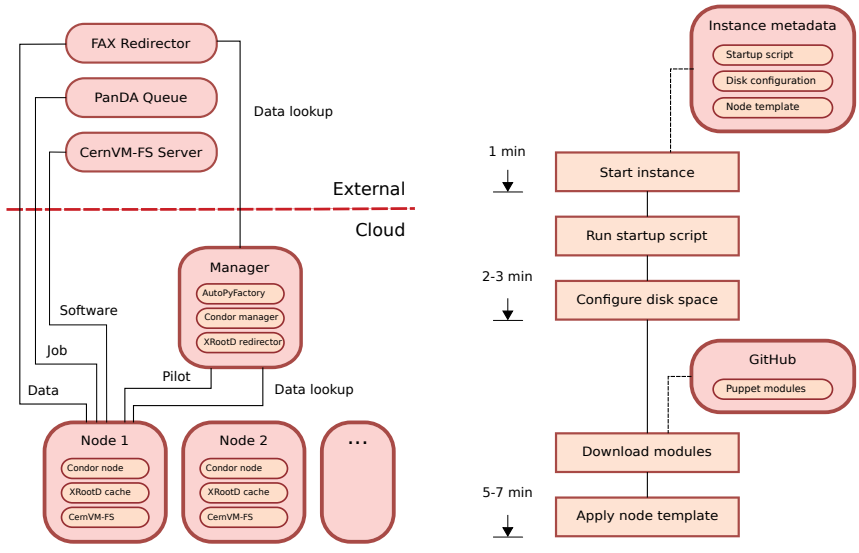


Figure 4.8. Schematic of a cluster configuration for ATLAS analysis on Google Compute Engine (left), and a typical contextualization procedure for a node in the cluster (right).

is possible to dynamically add and remove nodes from the cluster. Using an IaaS service, such as GCE, together with Puppet is found to be a viable option to temporarily increase computing resources, even when considering such short periods as a few hours.

5. Reconstruction, identification, and triggering of hadronically decaying τ-leptons

5.1 Introduction

τ-leptons offer a unique handle on Higgs boson physics both in and beyond the SM. Their relatively large mass means that they couple strongly to Higgs bosons, and their decays provide reasonably clean signatures compared to processes involving b- or top quarks. The first measurement of the Higgs boson coupling to fermions was performed in the $H \to \tau\tau$ analysis, which is covered in Section 6.2. Searches for charged Higgs bosons decaying through $H^+ \to \tau\nu$ are presented in Section 6.3.

τ-leptons have a very short (0.3 ps) lifetime [7] and typically decay within the volume of the beam pipe. They can decay leptonically into lighter leptons (muons or electrons, collectively denoted l), or hadronically into an odd number of charged, and zero or more neutral hadrons. The branching fraction for leptonic decays is about 35 %, where the fraction for individual leptons are similar as a consequence of *lepton universality*. In these decays, the lighter lepton is accompanied by two neutrinos: one of τ type (ν_τ) and one of the type of the light lepton (ν_l), i.e. $\tau \to l\nu_l\nu_\tau$.

Hadronic decays of τ-leptons occur in about 65 % of the cases and are classified depending on the number of charged particles (prongs) in the final state. The decays are composed of 1-prong decays (50 %), 3-prong decays (15 %), and in much more rare cases 5-prong (0.1 %) and 7-prong decays ($< 3.0 \times 10^{-5}$ %). The particle content of hadronically decaying τ-leptons consists mostly of charged and neutral pions ($\pi^\pm, \pi^0$), but also to a lesser extent kaons ($K^\pm, K^0, K^0_\mathrm{S}, K^0_\mathrm{L}$), ρ, η, and ω mesons, and other rare mesons. In all cases, hadronic decays of τ-leptons are accompanied by a ν_τ.

The neutrinos present in τ-lepton decays are required by the lepton number conservation. They are a source of true missing energy in the event, which means that the original energy and momentum of τ-leptons cannot be fully reconstructed. Consequently, neither can the mass of particles decaying into τ-leptons, such as the Higgs boson in $H \to \tau\tau$ decays. Several techniques exist to work around this limitation, and some of these are discussed in Section 6.2.2.

Leptonic decays of τ-leptons are reconstructed in the same way as prompt electrons or muons, and their reconstruction, identification, and

energy calibration are not discussed further. The detection of hadronically decaying τ-leptons is introduced in Section 5.2, and their reconstruction is discussed in Section 5.2.1. Precise identification, with discrimination against jets and electrons, is covered by Section 5.2.2, and their energy scale is discussed in Section 5.2.3. Finally, Section 5.3 is devoted to efficiency measurements of the τ trigger in $Z \to \tau\tau$ and $t\bar{t}$ events.

5.2 Detection, reconstruction, and identification

Hadronically decaying τ-leptons carry tell-tale signs that make them identifiable in a detector. The charged hadrons leave tracks in the inner detector, and all hadrons deposit energy in the electromagnetic and hadronic calorimeters. The result is a highly *collimated* jet with usually one or three associated tracks.

For the hadronic decays, sophisticated methods are required to discriminate against other objects. The dominant backgrounds to hadronically decaying τ-leptons are electrons (for 1-prong τ decays) and jets initiated by quarks and gluons. Electrons typically deposit most of their energy in the electromagnetic calorimeter, and are much more affected by transition radiation detectable in the TRT. Conversely, $\pi^0 \to \gamma\gamma$ decays from τ decays leave a large fraction of energy in the electromagnetic calorimeter. Since hadronically decaying τ-leptons are usually more collimated than jets initiated by quarks or gluons, many background jets can be rejected by requiring that the associated tracks are in the *core* region ($\Delta R < 0.2$ around its direction), and that no tracks are found in a surrounding *isolation* region ($0.2 < \Delta R < 0.4$).

5.2.1 Reconstructing hadroniclly decaying τ-leptons

Jets reconstructed with the anti-k_t algorithm with a distance parameter of $R = 0.4$ are used as seeds to the τ reconstruction algorithm [83, 97]. The jets are required to have $p_{\mathrm{T}} > 10\,\mathrm{GeV}$ and $|\eta| < 2.5$.

The τ_{had} candidate is not always produced in the selected primary vertex. To improve the reconstruction efficiency, the τ vertex (TV) association algorithm searches for the best match among all the primary vertex candidates in the event. The p_{T} of tracks within $\Delta R < 0.2$ of the jet seed direction are summed, and the primary vertex candidate to which the largest fraction of p_{T} can be matched is selected as the TV. The TV is subsequently used to define the direction and coordinate system of the τ_{had} candidate, as well as for track association. Figure 5.1 shows the efficiency estimated in simulated events, for correctly assigning

the τ production vertex using the default primary vertex with the highest $\sum p_{\mathrm{T}}^2$ as compared to the TV.

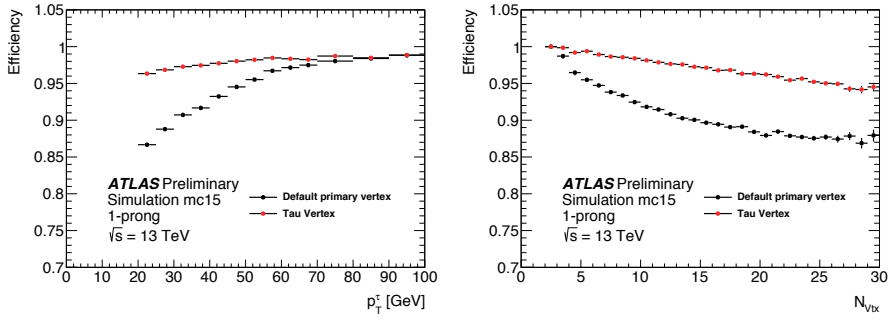


Figure 5.1. The efficiency for correctly assigning the τ production vertex by using the default primary vertex and by using the TV, as a function of the τ_{had} p_{T} (left) and the number of reconstructed vertices (right).

The three-momentum of the τ_{had} candidate is calculated in several steps. First, the centre in η and ϕ of the topological clusters of the jet seed is found. This calculation is done at the local hadronic (LC) scale [98], where a zero mass approximation is used for all constituents in the clusters. The four-momenta of all clusters in a cone $\Delta R < 0.2$ around the centre are recomputed using the TV as the origin. The sum of the four-momenta yields the direction of the τ_{had} candidate, and the momentum magnitude at the LC scale. The mass of the τ_{had} candidate is defined to be zero.

Tracks are associated with the τ_{had} candidate if found in the core region and have $p_{\mathrm{T}} > 1\,\mathrm{GeV}$. Cuts on the number of hits in the pixel and SCT sub-detectors, as well as on the transverse and longitudinal distances from the TV, are also applied.

The reconstruction efficiency for hadronically decaying τ-leptons is defined as the fraction of τ_{had} candidates that are reconstructed with the correct number of tracks, separately for 1- and 3-prong decays. The efficiency varies at different steps in the reconstruction. For instance, the efficiency for finding a jet seed for τ_{had} candidates with calibrated $p_{\mathrm{T}} > 20\,\mathrm{GeV}$ is almost 100 %. For 1-prong decays, increased p_{T} means that the decay might happen after the pixel detector, which causes the track to fail the quality requirements. Electrons from photon conversions also have a higher chance to meet the track quality criteria with higher p_{T}. If isolated tracks from such electrons coincide with the τ_{had} core region, they result in an incorrect number of charged particles. At high p_{T} the charged particles from 3-prong decays are more collimated, which might result in overlapping tracks and an underestimation of their number. On the other hand, at low p_{T} the charged particles might not leave tracks

with $p_{\mathrm{T}} > 1.0\,\mathrm{GeV}$. The reconstruction efficiency estimated in simulated events, where the reconstructed τ_{had} candidate is matched to a generated 1- or 3-prong decay, is shown in Figure 5.2.

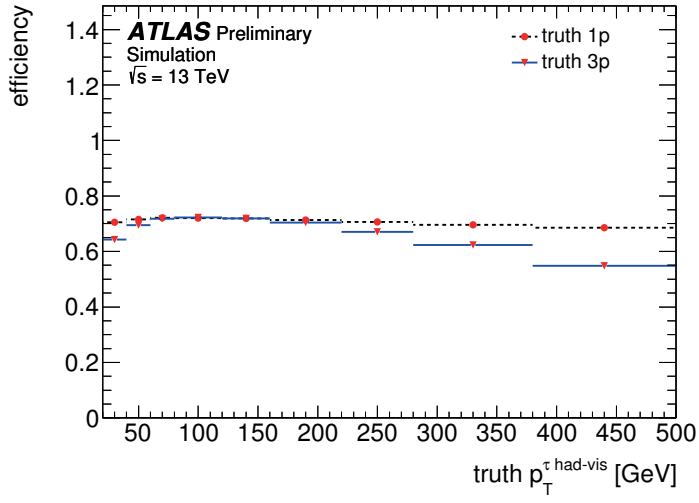


Figure 5.2. The reconstruction efficiency of 1- and 3-prong hadronic τ decays in simulated events. The efficiency is given as a function of the p_{T} of the generated visible decay products.

5.2.2 Identification of hadronically decaying τ-leptons

The reconstruction step provides very little rejection against background jets, and discrimination against these is performed in a separate identification step. Boosted Decision Tree (BDT) algorithms [99, 100] are trained separately for 1- and 3-prong τ_{had} candidates, and track- and topological cluster-based variables are used as input to these algorithms. The variables include impact parameter (IP) related variables, the fractions of energy in the calorimeter in the central region ($\Delta R < 0.1$ around the τ_{had} candidate direction), of energy of the track with the highest p_{T}, of the track p_{T} in the isolation region. Other variables are e.g. related to the number of neutral pions (π^0) in the event. Three working points are defined: *loose*, *medium*, and *tight*, corresponding to different pairs of values of identification efficiency and jet-rejection power.

The main difference between the 2012 and 2015–2016 data taking periods consists of harmonizing the input variables of the BDT algorithms, and the pile-up correction procedure, between the event reconstruction and the HLT. The average number of pile-up interactions in the event ($\langle\mu\rangle$) is used for the pile-up corrections, since the number of reconstructed

primary vertices in the event is not available in the HLT. The output from the π^0 reconstruction algorithm was also replaced with some of the input variables to this algorithm. The set of input variables used in the 2015–2016 BDT algorithms offers the same rejection power as the set used in 2012. The presence of the IBL also improves the resolution of the IP-related variables.

For the 2012 data taking, the BDT algorithms were trained with a combination of simulated $Z \to \tau\tau$, $Z' \to \tau\tau$, and $W \to \tau\nu$ events as signal, and a large sample of multi-jet data, collected using jet triggers, as background. For the 2015–2016 data taking, the BDT algorithms are instead trained with simulated $Z \to \tau\tau$ events as signal, and simulated di-jet events as background.

The combined reconstruction and identification efficiency is defined as the fraction of τ_{had} candidates that are reconstructed with the correct number of tracks, where the τ_{had} candidate fulfills specific identification criteria. It is used to define three working points: *loose*, *medium*, and *tight*. The working points are defined as p_{T}-dependent cuts on the BDT score, in order to ensure that they yield a constant efficiency independent of the p_{T} of the τ_{had} candidate. The combined efficiencies of the working points are 60 %, 55 %, and 45 % for 1-prong decays, and 50 %, 40 %, and 30 % for 3-prong decays, for the loose, medium, and tight working points, respectively. The inverse identification efficiency of jets from multi-jet events misidentified as τ_{had} candidates is shown in Figure 5.3, as a function of the τ_{had} identification efficiency.

1-prong τ decays can also be mimicked by electrons. Hence, τ_{had} candidates that geometrically overlap with an electron within $\Delta R < 0.4$ are rejected, if the electron fulfills a requirement on the likelihood identification score. The cut value on the electron likelihood score depends on the τ_{had} candidate p_{T}, and the η of the track, in order to have a constant identification efficiency of 95 % with respect to loose 1-prong τ_{had} candidates.

After the identification procedure, some τ_{had} candidates which are incorrectly reconstructed remain. These constitute important backgrounds to all analyses involving hadronically decaying τ-leptons. Various methods to estimate their contributions are described in Section 6.1. The behaviour of misidentified τ_{had} candidates in W+jets samples, simulated with ATLFAST [93], is studied in Section 6.2.3. The modelling of misidentified τ_{had} candidates using the same-sign contribution, in analyses where the signal events are sign-asymmetric, is discussed primarily in Section 5.3.4. The usage of *fake factors* to model misidentified τ_{had} candidates is described in Section 6.1.2.

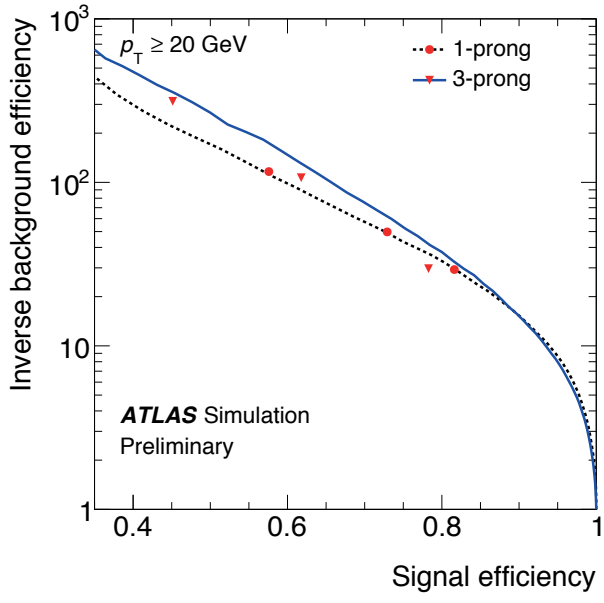


Figure 5.3. The inverse identification efficiency of jets from simulated multi-jet events misidentified as τ_{had} candidates, as a function of the τ_{had} identification efficiency. The markers indicate the *loose*, *medium*, and *tight* working points. The reconstruction efficiency is not included.

5.2.3 τ energy calibration

The energy of the τ_{had} candidate is reconstructed at the LC scale. The LC scale calibration accounts for energy losses in the calorimeter and the fraction of energy deposited outside the clusters, but is neither optimized for the narrow cone size of the core region of the τ_{had} candidate, nor for the mixture of hadrons (typically charged and neutral pions) that make up hadronic τ decays. Neither does the LC scale calibration correct for contributions from the underlying event or pile-up interactions. To bring the τ_{had} energy to the energy scale of the visible decay products, two correction functions are applied. The first correction pertains to the amount of pile-up interactions in the event, and increases linearly with the number of primary vertices. The second correction is the detector response function, which is derived as the Gaussian mean of the ratio of the LC energy, with the contribution from pile-up interactions removed, and the visible energy of the generated decay products. The detector response functions are derived from simulation, separately for 1- and 3-prong τ decays, and they are parametrized by pile-up corrected energy at the LC scale and $|\eta|$. The energy resolution, defined as the Gaussian width of the calibrated energy divided by the energy of the generated visible decay products, estimated in simulated $Z \to \tau\tau$ events is shown in Figure 5.4.

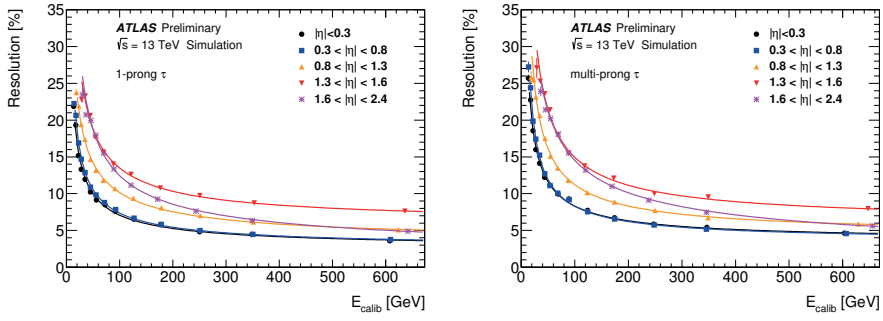


Figure 5.4. The energy resolution for 1-prong (left) and multi-prong (right) hadronic τ decays. The resolution is measured per response function, as a function of the calibrated energy.

5.2.4 Performance measurement in data

Measurements of identification and energy scale performance for τ_{had} candidates are done using a *tag-and-probe* technique. This technique relies on the presence of a muon and one hadronically decaying τ-lepton in the final state. The muon is the *tag*, which also is used to trigger the event, and it can come from leptonic decays of τ-leptons in $Z \to \tau\tau$ events. The hadronically decaying τ-lepton in the event is the *probe*, the performance of which is to be studied.

The anti-correlation of the sign of the charges of the muon and the hadronically decaying τ-lepton, as well as the knowledge about the Z boson mass, are used to reject events from the background of misidentified τ_{had} candidates from multi-jet, W+jets, Z+jets, $t\bar{t}$, and single-top-quark events. After subtracting the background from the data, the performance of the identification and energy scale of hadronically decaying τ-leptons in data can be compared to those in simulated events. Differences in the identification performance are compensated by applying *scale factors* to the τ_{had} candidates in simulated events, and by corrections to the energy scale. The values of the scale factors are optimally equal to unity, while any energy scale correction should be small.

Figure 5.5 shows the distribution of the visible mass $(m_{\text{vis}}(\mu, \tau_{\text{had}}))$, the invariant mass of the muon and the visible decay products of the τ_{had} candidate, measured with 13 TeV data corresponding to an integrated luminosity of 7.1 fb^{-1}, collected in 2016.

5.3 The τ trigger

Triggering on hadronically decaying τ-leptons is important for selecting events for many physics analyses, either as a stand-alone object or in combination with electrons, muons, or $E_{\text{T}}^{\text{miss}}$. Due to the intrinsic diffi-

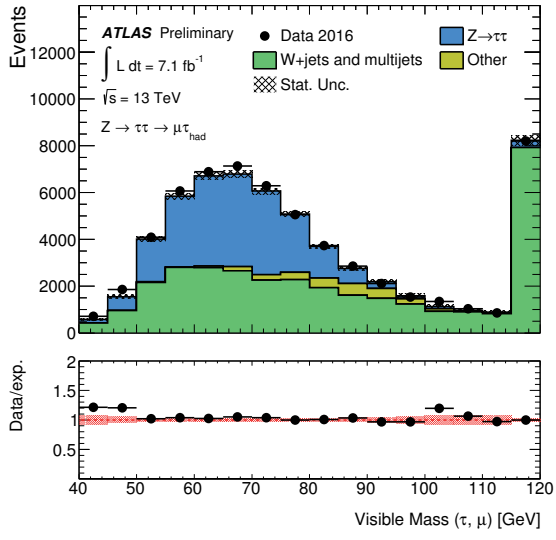


Figure 5.5. Distribution of the the $m_{\text{vis}}(\mu, \tau_{\text{had}})$, where the τ_{had} candidate fulfills loose identification criteria. Events are considered in an enriched sample of $Z \to \tau\tau$ events, selected by a muon trigger. The Z boson mass peak is visible on top of a background consisting mostly of misidentified τ_{had} candidates from multi-jet and W+jets events.

culty of correctly reconstructing and identifying hadronically decaying τ-leptons, and the large amount of jets at the LHC, the p_{T}-threshold is typically higher than for the corresponding lepton triggers. It is therefore primarily used to select events in decays where no leptons are present, or in combination with other triggers, the thresholds of which can then be lowered.

In analyses where two τ-leptons decay hadronically, a two-object τ trigger is typically used. The single τ trigger has a significantly higher p_{T}-threshold than its two-object counterpart, and events selected by this trigger can be included as a complement. The two-object τ trigger is used to select $\tau_{\text{had}}\tau_{\text{had}}$ events in the Run 1 $H \to \tau\tau$ analysis [101] described in Section 6.2.

$H^+ \to \tau\nu$ decays have a unique signature with a hadronically decaying τ-lepton and $E_{\text{T}}^{\text{miss}}$, and a combined $\tau + E_{\text{T}}^{\text{miss}}$ trigger has been specifically tailored for these decays. For the Run 1 search [31], the thresholds were $p_{\text{T}} > 27\,\text{GeV}$ or $29\,\text{GeV}$ and $E_{\text{T}}^{\text{miss}} > 40\,\text{GeV}$ or $50\,\text{GeV}$. The same trigger with thresholds of $p_{\text{T}} > 35\,\text{GeV}$ and $E_{\text{T}}^{\text{miss}} > 70\,\text{GeV}$ might be used in future searches.

5.3.1 τ trigger performance analyses

The reconstruction of hadronically decaying τ-leptons at the HLT is similar to the one used in the event reconstruction. For Run 2 the inputs to the identification algorithms are harmonized at the HLT and event reconstruction steps (see Section 5.2.2). However, the identification at the HLT is not 100 % efficient with respect to τ_{had} candidates in the event reconstruction. Two measurements of the trigger efficiency are performed. Both employ a tag-and-probe technique, where a muon acts as the tag and a τ_{had} candidate as the probe.

One measurement targets the $Z \to \tau\tau$ process and, while it provides a selection of τ_{had} candidates with high purity and statistics, it is limited in p_{T} reach. The Z boson mass of 91 GeV yields τ-leptons with $p_{\text{T}} \lesssim 45\,\text{GeV}$ at rest, and to measure efficiencies at higher p_{T}, the Z boson must be boosted.

In the $t\bar{t}$ process, each top-quark decay produces a W boson, which in turn can decay into a τ-lepton. Thanks to the larger top-quark mass of 173 GeV, the $t\bar{t}$ process provides hadronically decaying τ-leptons in a higher p_{T}-range. The second measurement targets these events, where the muon originates from $W \to \mu\nu$ or from a leptonic τ decay, while the hadronically decaying τ-lepton is a product of $W \to \tau\nu$. The $t\bar{t}$ production cross-section is measured in 13 TeV pp collisions to be $\sigma_{t\bar{t}} = 818$ $\pm 8(\text{stat})$ $\pm 27(\text{syst})$ $\pm 18(\text{lumi})$ $\pm 12(\text{beam})$ pb [102]. With data corresponding to integrated luminosities of $3.2\,\text{fb}^{-1}$ and $11.5\,\text{fb}^{-1}$, the 2015 dataset and part of the 2016 dataset used in this thesis contain about 2.5 and 10 million such pairs, respectively. The combined branching fraction for $t\bar{t} \to [b\mu\nu_{\mu}][b\tau\nu_{\tau}]$ is about 1 %.

Efficiencies and scale factors

The trigger efficiency is measured with respect to the various identification working points. In the following, medium identification criteria are required unless explicitly stated otherwise.

The efficiency is defined as the number of events that pass the tag-and-probe event selection and the specified τ trigger (PASS), divided by the number of events that pass the tag-and-probe event selection (TOT). The ratio of the signal efficiency and data efficiency is called the scale factor (SF).

The signal is composed of simulated events where a τ_{had} candidate is geometrically matched to a generated hadronically decaying τ-lepton. When calculating the efficiency in data, the backgrounds are subtracted. The scale factor is compatible with unity if the reconstruction and identifi-

cation of hadronically decaying τ-leptons are well modelled in simulation.

$$\varepsilon_{\text{sig}} = \frac{N^{\text{MC}}_{\text{true }\tau}(\text{PASS})}{N^{\text{MC}}_{\text{true }\tau}(\text{TOT})} \tag{5.1}$$

$$\varepsilon_{\text{data}} = \frac{N^{\text{data}}(\text{PASS}) - N^{\text{bkg}}(\text{PASS})}{N^{\text{data}}(\text{TOT}) - N^{\text{bkg}}(\text{TOT})} \tag{5.2}$$

$$\text{SF} = \frac{\varepsilon_{\text{data}}}{\varepsilon_{\text{sig}}}. \tag{5.3}$$

Treatment of systematic uncertainties

The systematic uncertainties considered for the efficiencies and scale factors arise from the subtraction of background events from the data, and affect $\varepsilon_{\text{data}}$. The systematic uncertainties are applied as upwards and downwards variations of a given parameter with the magnitude of 1σ, and these corrections may affect the final event yields positively or negatively. They propagate to the efficiencies through the difference in yields for the event selections with and without the trigger. The nominal efficiency is then subtracted from the efficiency variations for each systematic uncertainty, and the positive and negative contributions are summed in quadrature to form the total systematic uncertainty on the efficiency. In cases where both variations are positive or negative, the largest in magnitude is used in that direction, while the contribution in the opposite direction is set to zero.

The systematic uncertainties are either considered correlated or uncorrelated with respect to the event selections with and without the trigger. For correlated systematic uncertainties, the numerator and the denominator have the corrections applied simultaneously to form the efficiency uncertainty

$$\sigma^{\text{cor}}_{\pm} = \frac{N^{\text{data-bkg}}(\text{PASS}, \pm)}{N^{\text{data-bkg}}(\text{TOT}, \pm)} - \frac{N^{\text{data-bkg}}(\text{PASS})}{N^{\text{data-bkg}}(\text{TOT})} \tag{5.4}$$

where $\pm$ refers to the upwards and downwards systematic variations.

In the treatment of systematic uncertainties that are uncorrelated with respect to applying the trigger, the numerator and denominator are varied separately, resulting in two individual uncertainties on the efficiency:

$$\sigma^{\text{uncor, total}}_{\pm} = \frac{N^{\text{data-bkg}}(\text{PASS})}{N^{\text{data-bkg}}(\text{TOT}, \pm)} - \frac{N^{\text{data-bkg}}(\text{PASS})}{N^{\text{data-bkg}}(\text{TOT})} \tag{5.5}$$

$$\sigma^{\text{uncor, passed}}_{\pm} = \frac{N^{\text{data-bkg}}(\text{PASS}, \pm)}{N^{\text{data-bkg}}(\text{TOT})} - \frac{N^{\text{data-bkg}}(\text{PASS})}{N^{\text{data-bkg}}(\text{TOT})} \tag{5.6}$$

5.3.2 Data and simulation samples

The data used in these studies are collected with the ATLAS experiment in pp collisions at 13 TeV, and correspond to an integrated luminosity of $3.2\,\text{fb}^{-1}$ in 2015 and $11.5\,\text{fb}^{-1}$ in 2016. Only data where all sub-detectors are fully functional are considered.

Signal and background samples are produced with Monte Carlo (MC) simulation. The detector response is simulated using GEANT4 [92], and events are reconstructed with the same algorithms as data. The trigger response is emulated during reconstruction. Production of W and Z bosons in association with jets are generated with POWHEG [87] interfaced to PYTHIA8 [89] for the showering. $t\bar{t}$ and single-top-quark production are also generated with POWHEG, but interfaced to PYTHIA6 [88] for the showering. Pile-up interactions are simulated from *minimum-bias* events, and are overlaid on the generated events according to the expected multiplicity of pile-up interactions per bunch crossing, later corrected to the measured distribution.

5.3.3 Object and event selection

The object and event selection for the τ trigger performance analyses in Run 1 are described in detail in Ref. [83]. The selections for the analyses in Run 2 are similar, and are summarized here.

Combined muons with medium identification are considered. They are required to have $|\eta| < 2.5$, and $p_{\text{T}} > 22\,\text{GeV}$ (26 GeV) for 2015 (2016) data. In the signal regions, they are also required to pass the *gradient* isolation criteria [70]. When considered, electrons must satisfy medium LH identification criteria, and have $|\eta| < 2.5$ (with $1.37 < |\eta| < 1.52$ excluded) and $p_{\text{T}} > 15\,\text{GeV}$.

Jets are reconstructed using the anti-k_t algorithm and are required to have $p_{\text{T}} > 20\,\text{GeV}$ and $|\eta| < 4.5$. The JVT threshold for jets with $|\eta| < 2.4$ and $p_{\text{T}} < 50\,\text{GeV}$ is 0.64. A b-tagging algorithm is used to identify jets coming from a b-quark decay, with a 77 % (70 %) efficient working point in 2015 (2016) data. Hadronically decaying τ-leptons are reconstructed from anti-k_t jet seeds, and are required to have $|\eta| < 2.5$ (with $1.37 < |\eta| < 1.52$ excluded), $p_{\text{T}} > 20\,\text{GeV}$, and one or three associated tracks. The identification working point for the τ_{had} candidates varies with the measurement. Object overlap is resolved in the order: muons, electrons, τ_{had} candidates, and jets. See Section 4.2 for more information about particle identification and object overlap.

Events are selected by a muon trigger with a threshold of $p_{\text{T}} > 20\,\text{GeV}$ (24 GeV) in 2015 (2016). They are required to pass basic event cleaning criteria, and events with bad quality jets are rejected. Opposite-sign charges are required for the muon and the τ_{had} candidate.

The event selection for the $Z \to \tau\tau$ tag-and-probe measurement has cuts on the $E_{\mathrm{T}}^{\mathrm{miss}}$, and on the transverse mass of the muon and the $E_{\mathrm{T}}^{\mathrm{miss}}$

$$m_{\mathrm{T}} = \sqrt{2p_{\mathrm{T}}^{l} E_{\mathrm{T}}^{\mathrm{miss}} (1 - \cos\Delta\phi(l, E_{\mathrm{T}}^{\mathrm{miss}})}, \tag{5.7}$$

where l represents the muon, to reject W+jets events. The $m_{\mathrm{vis}}(\mu, \tau_{\mathrm{had}})$ is required to be compatible with the Z boson mass. The threshold on the sum of azimuthal distances between the muon and the $E_{\mathrm{T}}^{\mathrm{miss}}$, and between the τ_{had} candidate and the $E_{\mathrm{T}}^{\mathrm{miss}}$, is $\sum \cos\Delta\phi > -0.5$. The purity, defined as the fraction of events in data that come from the $Z \to \tau\tau$ process, is about 65 %.

The event selection for the $t\bar{t}$ tag-and-probe measurement has two requirements to ensure a reasonable purity of $t\bar{t}$ events. The events must contain at least two jets with $p_{\mathrm{T}} > 25\,\mathrm{GeV}$ and $|\eta| < 4.5$. Additionally, one of the jets must be b-tagged and have $|\eta| < 2.5$. The purity of the selection is about 60 %, and increases to about 70 % when requiring that the τ_{had} candidate has $p_{\mathrm{T}} > 60\,\mathrm{GeV}$.

5.3.4 Background strategies

Since the signal purity is not 100 % in either of the analyses, it is necessary to subtract the expected background events from the data. In both the $Z \to \tau\tau$ and $t\bar{t}$ tag-and-probe analyses, the backgrounds are mostly estimated with data-driven methods. In the $Z \to \tau\tau$ analysis, the background consists of a mixture of multi-jet and W+jets events, with small contributions from other Z+jets events. The $t\bar{t}$ analysis has inherently stronger rejection against multi-jet, W+jets, and Z+jets events, but suffers from misidentified τ_{had} candidates originating from quark-initiated jets in the hadronic decay of one of the W bosons in $t\bar{t}$ events.

In both analyses, the shape of the multi-jet background is taken from the same-sign (SS) data distribution, and scaled using normalization factors. The normalization factors (r_{QCD}) are derived as the ratio of opposite-sign (OS) and SS events in a multi-jet control region where the isolation criteria on the muon are inverted. Muons that are not a result of the hard interaction (e.g. coming directly from the Z or W boson decays) are often produced in association with other particles. The amount of momentum of tracks and energy deposits in the calorimeter in a narrow cone around, but not associated with the muon, is generally larger for these muons.

The background estimate for W+jets events in the $Z \to \tau\tau$ analysis uses the shape from simulated events and is normalized to the number of events in data. In order to avoid double counting, the SS contribution is

subtracted from the W+jets background. The normalization factors are derived as ratios of events in data and simulation.

In the $t\bar{t}$ analysis, the requirement of a b-tagged jet already suppresses much of the contribution from W+jets and Z+jets events. Hence, the background from quark- or gluon-initiated jets or leptons misidentified as τ_{had} candidates in W+jets and Z+jets events is less than 1 %. The simulated events from these processes are found to sometimes have large weights attached to them, which is problematic for the overall background estimation. Hence, they are assumed to be completely OS–SS symmetric, and covered by the SS data background.

In the $Z \to \tau\tau$ analysis, the small background from light leptons misidentified as τ_{had} candidates is modelled by simulation for all processes, while in the $t\bar{t}$ analysis these events are modelled by simulation for the $t\bar{t}$ and single-top-quark processes.

5.3.5 $Z \to \tau\tau$ tag-and-probe analysis

The τ trigger efficiency is measured in an enriched sample of $Z \to \tau\tau$ events, in the L1 and the HLT. The L1 trigger has a transverse energy (E_{T}) threshold of 12 GeV and an isolation requirement. The HLT trigger has a threshold of $p_{\text{T}} > 25$ GeV. The τ trigger efficiencies as measured in 13 TeV data corresponding to an integrated luminosity of 8.0 fb^{-1}, collected in 2016, are shown in Figure 5.6. The trigger reaches the efficiency plateau at $p_{\text{T}} \gtrsim 45$ GeV, and shows reasonable stability with respect to pile-up.

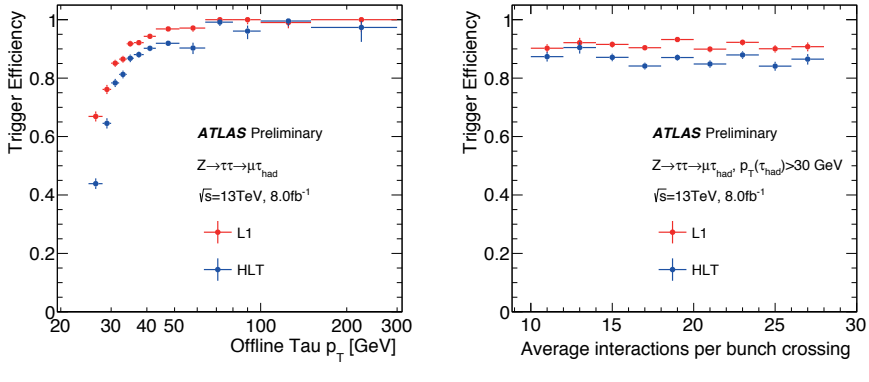


Figure 5.6. The trigger efficiency for τ_{had} candidates fulfilling medium identification criteria as a function of their p_{T} (left) and $\langle\mu\rangle$ (right), measured for the L1 trigger with $E_{\text{T}} > 12$ GeV and the HLT trigger with $p_{\text{T}} > 25$ GeV.

The HLT trigger efficiency in data is compared to that in simulated $Z \to \tau\tau$ events in Figure 5.7. It is well modelled for τ_{had} candidates with $p_{\text{T}} > 30\,\text{GeV}$, and the scale factors are compatible with unity.

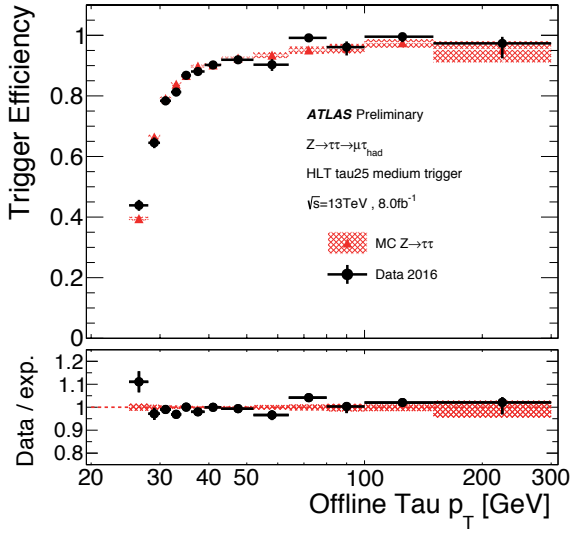


Figure 5.7. The trigger efficiency for the HLT trigger with a threshold of $p_{\text{T}} > 25\,\text{GeV}$, for τ_{had} candidates fulfilling medium identification criteria, and as a function of their p_{T}. The efficiency is measured both in data and simulated events, and the scale factor is computed as the the ratio of the two. The expected background has been subtracted from the data. Only statistical uncertainties are shown.

5.3.6 $t\bar{t}$ tag-and-probe analysis

The $t\bar{t}$ tag-and-probe analysis used for the τ trigger efficiency measurement described in the following is entirely performed by the author.

Signal events and background estimation

Simulated $t\bar{t}$, single-top-quark, W+jets, and Z+jets events, where the τ_{had} candidate is matched to a generated hadronically decaying τ-lepton, are considered as signal events.

The multi-jet control region is defined as the signal region with inverted isolation criteria for the muon. It is chosen to be as close to the signal region as possible, while retaining a high purity in multi-jet events. The inclusion of the b-tagging requirement sacrifices some purity in exchange for a larger degree of similitude with the signal region. It results in fewer events in the control region and therefore a higher statistical uncertainty on the r_{QCD} factors, but also a greater confidence in their accuracy.

r_{QCD} factors are derived separately for 1- and 3-prong τ_{had} candidates; for loose, medium, and tight identification criteria; with and without τ trigger; and in different regions in τ_{had} candidate p_{T}

$$r_{\text{QCD}} = \frac{N_{\text{OS}}^{\text{Data}} - N_{\text{OS}}^{\text{MC}}}{N_{\text{SS}}^{\text{Data}} - N_{\text{OS}}^{\text{MC}}}. \tag{5.8}$$

The r_{QCD} factors are applied to SS events in the signal region to form the SS data background

$$\text{SS data} = \sum_i r_{\text{QCD}} \times \text{SS}^{\text{SR}}, \tag{5.9}$$

where i represents the p_{T}-regions of the r_{QCD} factors.

Systematic uncertainties

The systematic uncertainties considered in the $t\bar{t}$ tag-and-probe analysis are related to the triggering by, and reconstruction and identification of muons, the identification efficiency of b-tagged jets, and the systematic and statistical uncertainties related to the r_{QCD} factors.

The uncertainties on the r_{QCD} computation have statistical and systematic components. The statistical component is computed assuming that the numbers of OS and SS events in the multi-jet control region follow the normal distribution. To derive the systematic component, the distributions of track- and calorimeter-based isolation variables are used. Their thresholds relative to the muon track p_{T} and calorimeter E_{T} are varied individually, and the envelope of the change of the r_{QCD} factor under each variation makes one component of the systematic uncertainty. The total systematic uncertainty on the r_{QCD} factor is computed by adding the two components in quadrature.

The total effect of systematic uncertainties on the weighted-average efficiency for the trigger with a threshold of $p_{\text{T}} > 25\,\text{GeV}$ is 3.2 % (0.8 %), while the effect on any single efficiency bin is 4.6 % (2.4 %), for 2015 (2016) data. The effects of individual systematic uncertainties are shown in Table 5.1.

Results

Trigger efficiencies are measured with the complete 2015 dataset corresponding an integrated luminosity of $3.2\,\text{fb}^{-1}$, and part of the 2016 dataset corresponding to an integrated luminosity of $11.5\,\text{fb}^{-1}$. Distributions of the τ_{had} candidate p_{T} are shown in Figure 5.8 and Figure 5.10, for 2015 and 2016 data, respectively. Reasonable agreement is observed, except for a large deficit in the expected distribution from simulation and data-driven methods as compared to the 2016 data. This deficit is found to

Table 5.1. *The effects of individual systematic variations on the trigger efficiency in 2015 and 2016 data. The effects are shown as relative to the weighted-average efficiency for the τ trigger with a threshold of $p_T > 25$ GeV, for τ_{had} candidates with 1 or 3 reconstructed tracks, $p_T > 60$ GeV, and which pass medium identification criteria.*

Systematic uncertainty	**2015**	**2016**
r_{QCD}	3.2 %	0.8 %
Pile-up	0.4 %	0.1 %
b-jets	< 0.1 %	< 0.1 %
Muons	< 0.1 %	< 0.1 %

originate from differences in the BDT output score for 1-prong τ_{had} candidates in data and simulated events. The yields as well as the fractions of the expected signal and backgrounds are given in Table 5.2.

Table 5.2. *Yields of events in data and expected events from simulation and data-driven methods, as well as their fractions. Events are considered in 2015 and 2016 data, where the τ_{had} candidate passes medium identification criteria, and its p_T-threshold is 25 GeV.*

	2015		**2016**	
	Events	**Fraction**	**Events**	**Fraction**
Data	5299	–	17 918	–
Signal (MC)	3034	58.1 %	9097	57.0 %
Mis-ID τ (SS data)	1462	28.0 %	4579	28.7 %
Mis-ID τ (MC)	721	13.8 %	2292	14.4 %
Total	5217	100 %	15 968	100 %

For the trigger efficiency measurement, the p_{T}-threshold on the τ_{had} candidate is increased to 60 GeV, leading to a purity of about 70 % (72 %) in 2015 (2016) data. The trigger efficiencies and scale factors for the trigger with a threshold of $p_{\text{T}} > 25$ GeV are shown in Figure 5.9 and Figure 5.11. The scale factors in 2015 data are nearly compatible with unity for the 1-prong τ_{had} candidates. The differences compared to the results from the $Z \to \tau\tau$ analysis, can most likely be explained by statistical fluctuations affecting the OS and SS data distributions. In 2016 data, the 1-prong scale factors show a clear decline towards higher p_{T}. Here, both the statistical and systematic uncertainties are tightly constrained.

The lowest τ trigger for analysis in 2015 p_{T}-threshold of 80 GeV, while in the 2016 data considered in this thesis, the threshold is 125 GeV. The efficiencies and scale factors for these triggers are shown in Figure 5.12 and Figure 5.13, respectively.

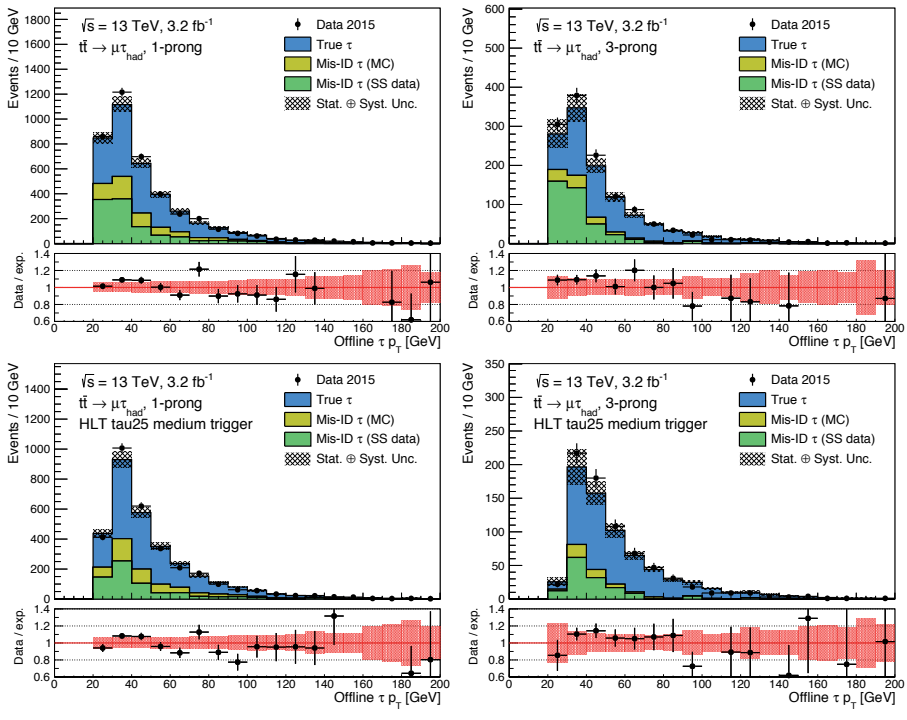


Figure 5.8. Distributions of the p_{T} for τ_{had} candidates with 1 (left) and 3 (right) reconstructed tracks. Events are considered in 2015 data, where the τ_{had} candidate passes medium identification criteria (top) and additionally fires the τ trigger with a threshold of $p_{\mathrm{T}} > 25\,\mathrm{GeV}$ (bottom).

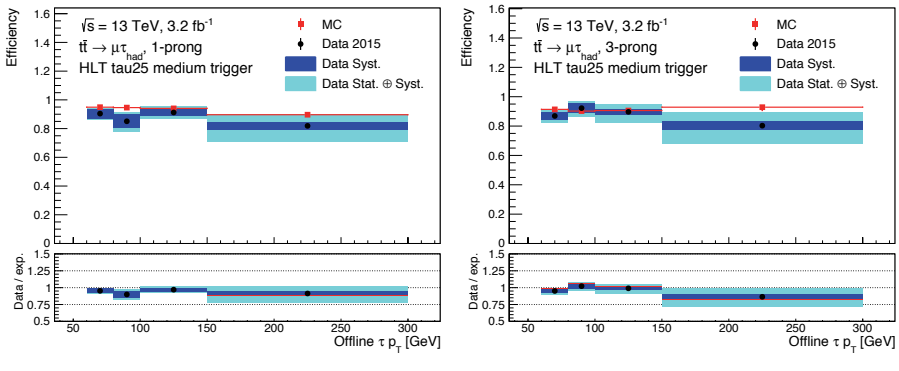


Figure 5.9. Trigger efficiency for τ_{had} candidates with 1 (left) and 3 (right) reconstructed tracks. Events are considered in 2015 data, where the τ_{had} candidate passes medium identification criteria, and has a p_{T}-threshold of 60 GeV. The expected background has been subtracted from the data.

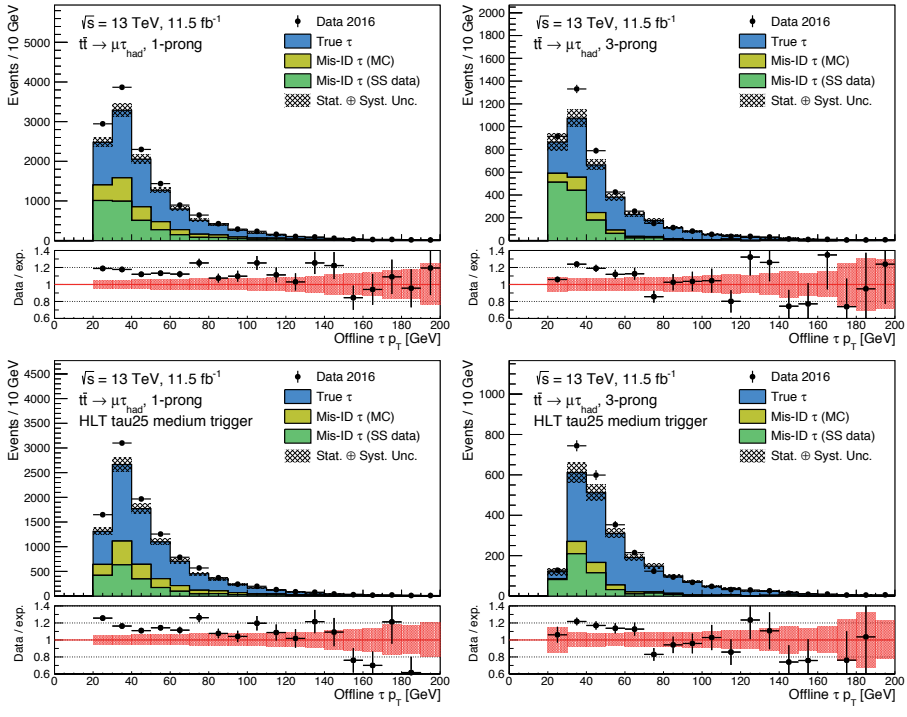


Figure 5.10. Distributions of the p_{T} for τ_{had} candidates with 1 (left) and 3 (right) reconstructed tracks. Events are considered in 2016 data, where the τ_{had} candidate passes medium identification criteria (top) and additionally fires the τ trigger with a threshold of $p_{\mathrm{T}} > 25\,\mathrm{GeV}$ (bottom).

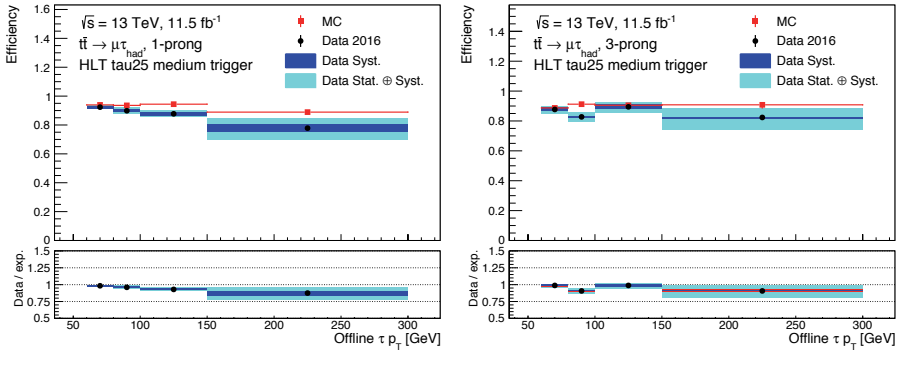


Figure 5.11. Trigger efficiency for τ_{had} candidates with 1 (left) and 3 (right) reconstructed tracks. Events are considered in 2016 data, where the τ_{had} candidate passes medium identification criteria, and has a p_{T}-threshold of 60 GeV. The expected background has been subtracted from the data.

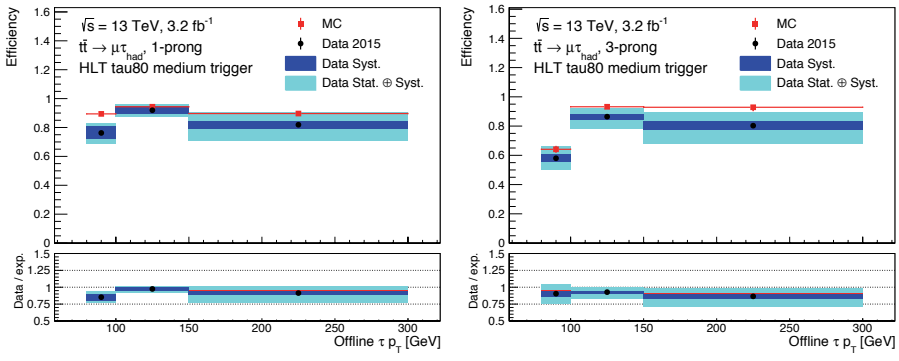


Figure 5.12. Trigger efficiency for τ_{had} candidates with 1 (left) and 3 (right) reconstructed tracks, where the trigger has a threshold of $p_{\text{T}} > 80\,\text{GeV}$. Events are considered in 2015 data, where the τ_{had} candidate passes medium identification criteria. The expected background has been subtracted from the data.

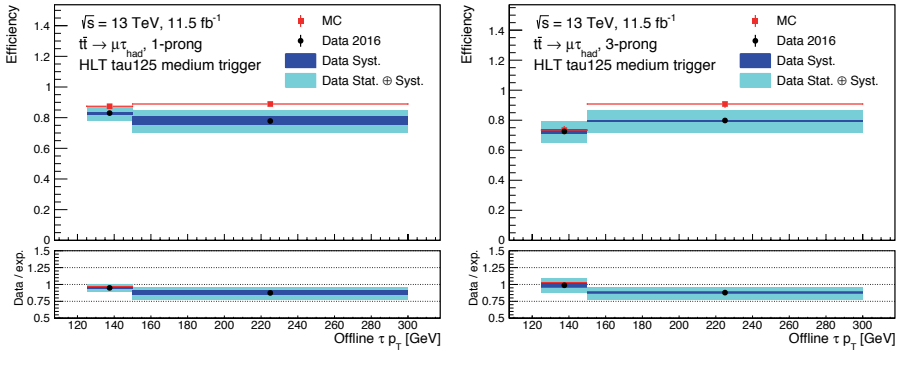


Figure 5.13. Trigger efficiency for τ_{had} candidates with 1 (left) and 3 (right) reconstructed tracks, where the trigger has a threshold of $p_{\text{T}} > 125\,\text{GeV}$. And events are considered in 2016 data, where the τ_{had} candidate passes medium identification criteria. The expected background has been subtracted from the data.

6. Higgs boson analyses with hadronically decaying τ-leptons

6.1 Analysis techniques

Analysis of data from the ATLAS experiment is a complex procedure that consists of several steps. Common to all analyses is choosing a trigger, selecting properties that define physics objects, and requirements on global event properties and kinematics.

Analyses commonly define a signal region, where the search for a signal or the extraction of a found signal is performed. The background contributions are modelled by simulated events, data-driven methods, or a combination thereof. Control regions are used to validate and constrain backgrounds, and to derive parameters for data-driven methods. The concepts of signal and control regions are described in Section 6.1.1. Modelling of backgrounds is discussed in Section 6.1.2. Discrimination between a potential signal and its backgrounds is covered in Section 6.1.3, and the statistical analysis to extract signal or set limits in Section 6.1.4.

6.1.1 Signal and control regions

The signal region is an event selection where the amount of signal is enhanced over the backgrounds. The enhancement is maximized through optimization. In cut-based analyses, the threshold on kinematic variables are scanned until an optimum is found, while in multivariate analyses, the input variables and parameters of the method are varied.

Control regions are selections that are similar but orthogonal to the signal region, and which are enriched with specific background processes. Common control regions cover events from multi-jet interactions, W+jets and Z+jets processes, and single-top-quark and $t\bar{t}$ processes. Special control regions are also used to enhance the fraction of misidentified τ_{had} candidates, typically by requiring very loose identification criteria. Such control regions are used for the *fake factor* background model (see Section 6.1.2).

6.1.2 Modelling of backgrounds

Backgrounds are preferably modelled with data-driven methods, since simulated events come with systematic uncertainties related to the event

generation, trigger emulation, detector response simulation, and object reconstruction. In some cases, the shape of the background can be taken from simulated events and the normalization from control regions in data. Control regions that are pure in background events can then be used to provide normalization factors in the signal region.

The fake factor method uses a side-band in data with looser τ_{had} identification criteria (anti-τ), which is extrapolated into the signal region to estimate the number of misidentified τ_{had} candidates. In the $H \to \tau\tau$ analysis (see Section 6.2.4), fake factors are derived separately for multi-jet events, as well as for the W+jets, $Z \to ll$ + jets, and $t\bar{t}$ processes. They are obtained from selections that are enriched in misidentified τ_{had} candidates, in separate control regions for each process, and then applied to the anti-τ events in the signal region to form the background where a quark- or gluon-initiated jet is misidentified as a τ_{had} candidate. In the $H^+ \to \tau\nu$ analysis (see Section 6.3.3), a single control region is used to obtain fake factors for all processes.

6.1.3 Signal-to-background discrimination

The background model is optimized to provide an adequate description of the background in the signal region. A signal can be extracted as the remainder of events, when the background has been subtracted. The extraction of the τ signal in the performance analyses in Chapter 5 are examples of such a procedure. In searches for new particles, a signal can be found as an excess of events over the expected background. This method is used to interpret the results from the $H \to \tau\tau$ analysis.

Using a combination of variables can yield a higher discriminating power than just one. A common MVA technique in ATLAS analyses uses BDT algorithms. A decision whether the event is more compatible with signal or background is made at each level of the tree, based on the value of an input variable. A BDT algorithm uses a collection (ensemble) of decision trees, where each individual tree is given a weight during training (boosting), indicating its relative importance in the entire training sample. The BDT score for a single event is the sum of weights of all the decision trees in the BDT algorithm for that particular event. BDT algorithms are used to provide signal-to-background discrimination in the $H \to \tau\tau$ analysis described in Section 6.2, but also to discriminate hadronically decaying τ-leptons from quark- and gluon-initiated jets in the τ_{had} identification algorithms described in Section 5.2.2.

6.1.4 Statistical analysis

Statistical analysis of data involves hypothesis testing. For searches, the null hypothesis (H_0) is usually represented by the background-only hypothesis, while the signal+background model constitutes the alternative hypothesis (H_1). These roles are reversed when setting limits. The level of agreement between data and a given hypothesis is quantified with the p-value, i.e. the predicted probability of finding data with an incompatibility greater than or equal to what is observed. The hypothesis is considered excluded if its p-value is below a certain threshold.

For signal searches, the p-value is usually converted to a *significance* Z, which corresponds to the number of standard deviations above the mean of a Gaussian distributed variable that has a probability of p in its tail. *Evidence* for a new signal is reached with $Z = 3$, while $Z = 5$ is the convention for a discovery. To exclude a signal+background hypothesis, a 95 % confidence level (CL) ($p = 0.05$ or $Z = 1.64$) is regularly used.

The *profile likelihood ratio* [103] is used to form the test statistic. The likelihood functions entering the ratio are parametrized as a function of a *signal strength* (μ) and a set of *nuisance parameters* ($\boldsymbol{\theta}$) describing the impact of systematic uncertainties on the signal and background distributions.

The likelihood function for binned analyses is defined as a product of Poisson distributions

$$L(\mu, \boldsymbol{\theta}) = \prod_{j=1}^{N} \frac{(\mu s_j + b_j)^{n_j}}{n_j!} e^{-(\mu s_j + b_j)} \prod_{k=1}^{N} \frac{u_k^{m_k}}{m_k!} e^{-u_k}. \tag{6.1}$$

Here, n_j is the number of observed events in the j:th bin in the signal region, while m_k is the corresponding number for the control regions. The signal+background model is described in the j:th bin by the expression $\mu s_j + b_j$, where s_j and b_j are the number of expected signal and background events respectively, and μ represents the signal strength. Similarly u_k is the number of expected events in the k:th bin of the control regions. $s_j(\boldsymbol{\theta})$, $b_j(\boldsymbol{\theta})$, and $u_k(\boldsymbol{\theta})$ are all functions of the nuisance parameters.

The profile likelihood ratio is defined as

$$\lambda(\mu) = \frac{L(\mu, \hat{\hat{\boldsymbol{\theta}}})}{L(\hat{\mu}, \hat{\boldsymbol{\theta}})}. \tag{6.2}$$

Here μ is the expected signal strength, where $\mu = 0$ corresponds to the background-only hypothesis, and $\mu = 1$ the nominal signal strength (e.g. for the SM Higgs boson). $\hat{\hat{\boldsymbol{\theta}}}$ is the set of nuisance parameters that maximizes the likelihood for a given μ, while $\hat{\boldsymbol{\theta}}$ and $\hat{\mu}$ is the combination that unconditionally maximizes L.

A convenient test statistic is

$$t_\mu = -2 \ln \lambda(\mu). \tag{6.3}$$

With $f(t_\mu|\mu)$ the probability density function (PDF) of t_μ, given the signal strength μ, the p-value can be defined as

$$p_\mu = \int_{t_\mu,\text{obs}}^{\infty} f(t_\mu|\mu)\, dt_\mu. \tag{6.4}$$

Two specialized test statistics are given for assessing the significance of an observed excess or setting of upper limits, respectively. The test statistic for the latter is:

$$q_0 = \begin{cases} -2 \ln \lambda(0) & \hat{\mu} \geq 0, \\ 0 & \hat{\mu} < 0. \end{cases} \tag{6.5}$$

For this test statistic a greater number of events than the background-only hypothesis corresponds to an increasing likelihood of a signal, while a deficit of events is considered compatible with the background-only model. The test statistic for determining the strength of an observed signal is:

$$q_\mu = \begin{cases} -2 \ln \lambda(\mu) & \hat{\mu} \geq \mu, \\ 0 & \hat{\mu} < \mu. \end{cases} \tag{6.6}$$

Here, a higher value of q_μ represents a greater incompatibility between the data and the signal+background hypothesis for a signal strength μ.

Confidence levels can be assigned to both the background-only and signal+background hypotheses. If the data appears to be compatible with the background-only hypothesis, it is useful to set exclusion limits on the signal+background hypothesis. The frequentist confidence level for the exclusion of the signal+background hypothesis is defined as

$$\text{CL}_{s+b} = P(q_\mu \geq q_\mu^{\text{obs}}) < \alpha, \tag{6.7}$$

where $1 - \alpha$ is the desired level of confidence. However, CL_{s+b} and the confidence level for the background-only hypothesis (CL_b) are sensitive to downwards statistical fluctuations when dealing with small sample sizes. The modified frequentist confidence level [104, 105]

$$\text{CL}_s = \frac{\text{CL}_{s+b}}{\text{CL}_b}, \tag{6.8}$$

is often used to avoid this problem. CL_s attempts to make a statement about the signal hypothesis alone, and while it is more conservative than CL_{s+b}, it is also more robust against low statistics.

By allowing that the signal strength $\hat{\mu}$ that maximizes the likelihood can take negative values, it can be modelled as a variable distributed according to the normal distribution with median μ' and standard deviation σ. The estimate of the simulated datasets can then be replaced by a single representative artificial dataset called the *Asimov dataset* [103]. It is defined such that when evaluating the values of all parameters (μ, $\boldsymbol{\theta}$) their true values are obtained. From this the Asimov likelihood (L_{A}) and the corresponding profile likelihood ratio (λ_{A}) can be found:

$$\lambda_{\mathrm{A}} = \frac{L_{\mathrm{A}}(\mu, \hat{\hat{\boldsymbol{\theta}}})}{L_{\mathrm{A}}(\hat{\mu}, \hat{\boldsymbol{\theta}})} = \frac{L_{\mathrm{A}}(\mu, \hat{\hat{\boldsymbol{\theta}}})}{L_{\mathrm{A}}(\mu', \boldsymbol{\theta})}. \tag{6.9}$$

The standard deviation of $\hat{\mu}$ then becomes

$$\sigma_{\mathrm{A}}^2 = \frac{(\mu - \mu')^2}{q_{\mu,\mathrm{A}}}, \tag{6.10}$$

where $q_{\mu,\mathrm{A}} = -2 \ln \lambda_{\mathrm{A}}(\mu)$. The distribution of $\hat{\mu}$ obtained in this way can be used to compute the expected significance of an analysis.

6.2 $H \to \tau\tau$ analyses

In order to establish the mass generation of fermions in the SM, it is important to measure the Higgs boson coupling in decays to these particles. Since the Higgs boson couples to mass, the leptons and quarks with the highest masses are the prime candidates for such measurements. The Higgs boson decay to two b-quarks is hampered by the large multi-jet background at the LHC. The Higgs boson decay to two τ-leptons has a lower branching fraction, and presents similar challenges for the hadronically decaying τ-leptons, but this is compensated by the high identification efficiency for muons and electrons in the semi-leptonic decay modes.

6.2.1 Analysis overview

In the following, the measurement of the Higgs boson coupling to fermions in decays to two τ-leptons, as detailed in Ref. [101], is presented. The full Run-1 dataset is used, with 7 TeV (8 TeV) data corresponding to an integrated luminosity of $4.7\,\mathrm{fb}^{-1}$ ($20.3\,\mathrm{fb}^{-1}$) collected in 2011 (2012).

Analysis categories

The search is conducted in three channels: the fully hadronic channel ($H \to \tau_{\mathrm{had}}\tau_{\mathrm{had}}$), the semi-leptonic channel ($H \to \tau_{\mathrm{lep}}\tau_{\mathrm{had}}$), and the fully leptonic channel ($H \to \tau_{\mathrm{lep}}\tau_{\mathrm{lep}}$), where τ_{lep} indicates a leptonic τ decay.

The search is further divided into two categories. The boosted category is sensitive to Higgs bosons with a high p_{T}, and is dominated by gluon-gluon fusion production in association with an extra jet from gluon radiation, while the vector-boson fusion (VBF) category is characterized by two extra jets with a large η-separation. Events from the production of a Higgs boson in association with a vector boson (VH) predominantly fall in the VBF category. See Section 2.1.2 for details on the Higgs boson production modes.

Trigger

The single-object electron trigger is used for the $e\tau_{\mathrm{had}}$ and $e\mu$ channels, and the single-object muon trigger for the $\mu\tau_{\mathrm{had}}$, $\mu\mu$, and $e\mu$ channels. The two-object electron trigger is used for the ee channel, and the two-object τ trigger for the $\tau_{\mathrm{had}}\tau_{\mathrm{had}}$ channel. The trigger thresholds vary to accommodate for the increasing instantaneous luminosity of the LHC under the data collection period, and the analysis level thresholds are set accordingly, to reach the efficiency plateau of the corresponding trigger.

Backgrounds

Events from the $Z \to \tau\tau$ process are the dominant background for all channels. It is largely irreducible, and a technique called *embedding* is used to model these events. Embedding uses $Z \to \mu\mu$ events from data, which can be identified with a high purity, and substitutes the muons with simulated τ decays.

Events from quark- and gluon-initiated jets misidentified as hadronically decaying τ-leptons constitute a major background in both the $H \to \tau_{\mathrm{had}}\tau_{\mathrm{had}}$ and $H \to \tau_{\mathrm{lep}}\tau_{\mathrm{had}}$ channels, while events with misidentified leptons play the same role in the $H \to \tau_{\mathrm{lep}}\tau_{\mathrm{lep}}$ channel. These backgrounds are to a large degree modelled with various data-driven methods.

Event selection

Among the event selections of the three decay modes, only a short overview for the $\tau_{\mathrm{lep}}\tau_{\mathrm{had}}$ channel is given here. In the $e\tau_{\mathrm{had}}$ channel, the electron is required to have $p_{\mathrm{T}} > 25(26)\,\mathrm{GeV}$ in $7(8)\,\mathrm{TeV}$ data, while in the $\mu\tau_{\mathrm{had}}$ channel, the muon is required to have $p_{\mathrm{T}} > 22(26)\,\mathrm{GeV}$ in $7(8)\,\mathrm{TeV}$ data. Track- and calorimeter-based isolation criteria are also applied. The τ_{had} candidate is required to have $p_{\mathrm{T}} > 20\,\mathrm{GeV}$. The lepton and τ_{had} candidates are required to have opposite-sign charges, and the reducible W+jets and $t\bar{t}$ backgrounds are suppressed by rejecting events with $m_{\mathrm{T}} > 70\,\mathrm{GeV}$ (Eq. (5.7)), and by requiring a b-tagged jet with $p_{\mathrm{T}} > 30\,\mathrm{GeV}$, respectively.

Signal-to-background discrimination
BDT algorithms are used to separate the $H \to \tau\tau$ signal from the background. Separate BDT algorithms are trained for each channel and category, based on expected signal and background distributions at 8 TeV. They are then applied to both 7 TeV and 8 TeV data. A few BDT input variables that are common to all channels include the MMC mass, which is used for both categories, the separation in pseudorapidity between two jets in the VBF category, and the centrality in the azimuthal direction of the $E_{\mathrm{T}}^{\mathrm{miss}}$ in the boosted category.

6.2.2 Mass reconstruction techniques

Due to the presence of two to four neutrinos, a complete reconstruction of the Higgs boson mass is not possible in $H \to \tau\tau$ decays. Several techniques exist to work around this limitation and produce an estimate of the Higgs boson mass that can be used to discriminate against $Z \to \tau\tau$ decays.

The collinear approximation assumes that the neutrinos are aligned with the visible decay products, and thus the fraction of missing energy associated with each τ decay can be determined. A limitation is its inability to reconstruct the $\tau\tau$ invariant mass in events where the two τ-leptons are produced back-to-back, and that it tends to overestimate the mass, which in turn leads to long tails in the $Z \to \tau\tau$ mass distribution, and hence a low degree of discrimination against these events.

The MMC technique [77] was developed to circumvent the limitations of the collinear approximation. The kinematics of the $H \to \tau\tau$ and $Z \to \tau\tau$ decays include six to eight unknown variables, corresponding to the 3-momenta of the two neutrino systems, and their masses in the case of leptonic decays. Only four equations relate these unknowns, resulting in an under-constrained system. The MMC scans the phase space consisting of:

- E_x^{miss} and E_y^{miss}, within the detector resolution,
- the angles between the τ-leptons and the neutrino systems,
- the masses of the neutrino systems (for leptonic decays),

and finds the best solution by minimizing a likelihood function in the physically allowed region. This function is defined as a product of probabilities for each point in phase space, and where the probability density functions (PDF) for the angles and masses of the neutrino system are derived in simulated $Z \to \tau\tau$ and $H \to \tau\tau$ events.

The author has investigated an alternative approach, where some of the PDFs are replaced by a kinematic fit using Lagrangian multipliers. The full kinematics of the decay is reconstructed using the corresponding matrix element of each τ decay, solving the quartic equation, and selecting

the most probable solution. While the alternative approach was found to be faster, it performed slightly worse with respect to the reconstructed Higgs boson mass resolution.

6.2.3 Validation of ATLFAST-II simulation

Events from the $W \to \ell\nu$ processes, where an extra jet in the event is misidentified as a hadronically decaying τ-lepton, are a small background in the $H \to \tau_{\text{lep}}\tau_{\text{had}}$ channel. The decay topology is very different from the $H \to \tau\tau$ decays, and only a very small amount of these events are expected to fulfill the event selection criteria. For this reason, a very large number of simulated $W \to \ell\nu$ events are required to obtain sufficient statistical precision.

The ATLFAST-II detector simulation can be used to reduce the computation time, compared to the full GEANT4 detector simulation. Since the calorimeter response is simulated through a smearing of the energy, ATLFAST-II is expected to perform worse than the full simulation for hadronically decaying τ-leptons. In particular, the simulation of misidentified τ_{had} candidates must be validated. This validation was performed by the author, and it was found that the simulation of misidentified τ_{had} candidates in ATLFAST-II is adequate. Figure 6.1 shows the p_{T} distributions of τ_{had} candidates for the two simulation methods.

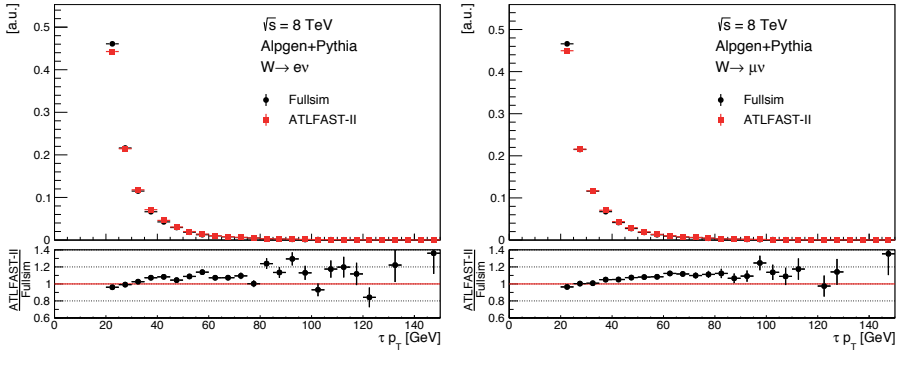


Figure 6.1. Distribution of the τ_{had} candidate p_{T} for $W \to e\nu$ (left) and $W \to \mu\nu$ (right) events, generated with ALPGEN+PYTHIA, and simulated with the full detector simulation as well as ATLFAST-II. The distributions have been scaled so that their integrals equal unity. A preselection has been applied, where events are required to have one lepton, and one τ_{had} candidate fulfilling medium identification criteria. The bottom plot shows the ratio of normalized events for the two simulation methods.

6.2.4 Estimation of misidentified τ-leptons

The *fake-factor* method is used to estimate the background contribution where a quark- or gluon-initiated jet is misidentified as a hadronically decaying τ-lepton in the $H \to \tau_{\text{lep}}\tau_{\text{had}}$ channel. The fake factors are applied to anti-τ events in the signal region, and weighted by the estimated size of the contribution from each process. The author has worked with developing the fake-factor method for the $H \to \tau_{\text{lep}}\tau_{\text{had}}$ channel in the analysis of 7 TeV data. Figure 6.2 shows the distribution of the MMC mass in the boosted and VBF categories, where the contribution from misidentified τ_{had} candidates is estimated with the fake-factor method.

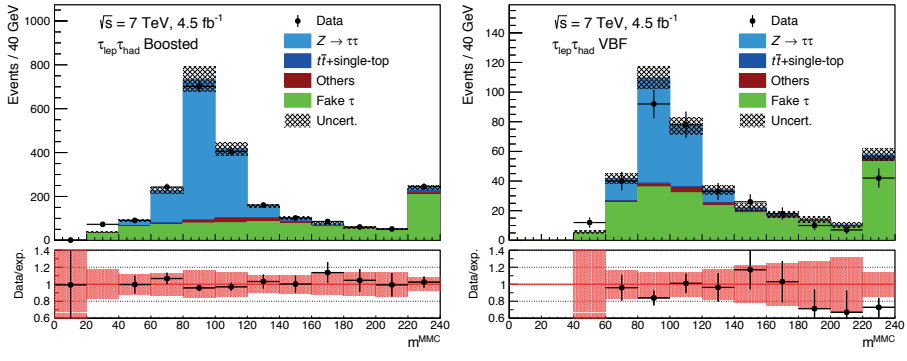


Figure 6.2. Distribution of the MMC mass in the boosted (left) and VBF (right) categories in the $H \to \tau_{\text{lep}}\tau_{\text{had}}$ channel with 7 TeV data. The bottom plot shows the ratio of events in data and the expected background. The uncertainty includes the statistical and systematic components, as obtained before the profile likelihood fit.

6.2.5 Results

The signal is extracted using a maximum likelihood fit simultaneously in the two categories of all three channels. The distributions of the BDT score in the signal regions are used for the likelihood maximization, and information from control regions helps constrain backgrounds.

Using $m_H = 125.36\,\text{GeV}$ [106], the signal strength corresponding to the best fit is

$$\mu = 1.43^{+0.27}_{-0.26}(\text{stat.})^{+0.32}_{-0.27}(\text{syst.}) \pm 0.09(\text{th.}), \tag{6.11}$$

where (th.) refers to the theoretical uncertainty on the Higgs boson production cross section, and the branching fraction to $H \to \tau\tau$. The measured signal strength corresponds to a deviation from the background-only hypothesis of 4.5σ, providing the first evidence for Higgs boson decays into τ-leptons in ATLAS.

Figure 6.3 shows the event yield as a function of $\log_{10}(S/B)$, where S/B is the signal-to-background ratio calculated for each BDT score bin in the signal region, assuming $\mu = 1.4$. Figure 6.4 shows the distribution of the MMC mass, where each event is weighted with $\ln(1+S/B)$ in order to visualize the excess over the background.

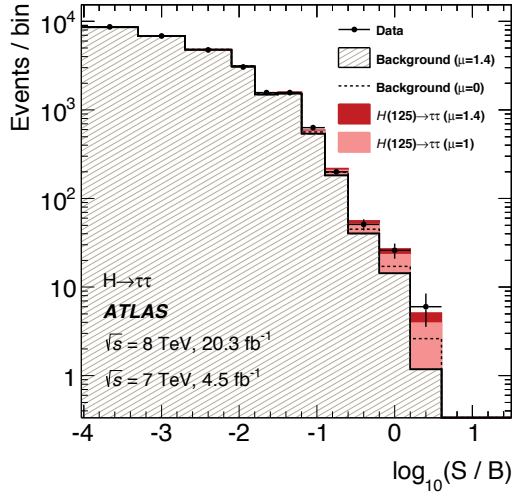


Figure 6.3. The event yield in all channels and categories as a function of $\log_{10}(S/B)$. S/B is the signal-to-background ratio calculated for each BDT score bin in the signal region. The background prediction is obtained from the maximum likelihood fit, using $m_H = 125\,\text{GeV}$ and $\mu = 1.4$. The corresponding signal hypothesis, with strength $\mu = 1.0$ or $\mu = 1.4$, is shown on top of the background prediction. The fit to the background-only hypothesis ($\mu = 0$) is shown for comparison.

The data are also divided into two topologies, separating the VBF and VH production modes from the gluon-gluon fusion, and the corresponding signal strengths (μ_{ggF}, $\mu_{\text{VBF}+VH}$) are measured. The results are shown in Figure 6.5, along with likelihood contours and the corresponding values from the SM prediction.

6.3 $H^+ \to \tau\nu$ analyses

The existence of charged Higgs bosons is predicted by 2HDM, and notably the MSSM. Due to its coupling to mass, the charged Higgs boson is predicted to decay predominantly to $H^+ \to tb$ for masses above the top-quark mass. This signature is difficult to separate from the $t\bar{t}$ background with extra heavy-flavour jets [33, 107]. For this reason, the $H^+ \to \tau\nu$ decay mode plays an important role, owing to its cleaner signature. See

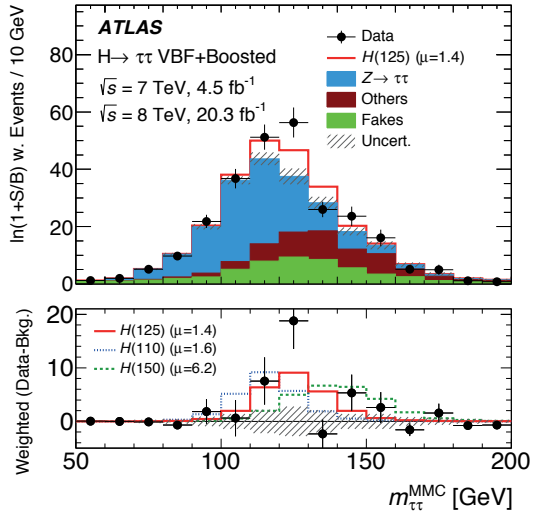


Figure 6.4. The distribution of the MMC mass in all channels and categories, where each event is weighted by $\ln(1+S/B)$. S/B is the signal-to-background ratio calculated for each BDT score bin in the signal region. The background prediction is obtained from the maximum likelihood fit, using $m_H = 125\,\text{GeV}$ and $\mu = 1.4$. The corresponding signal hypothesis with $\mu = 1.4$ is shown on top of the background.

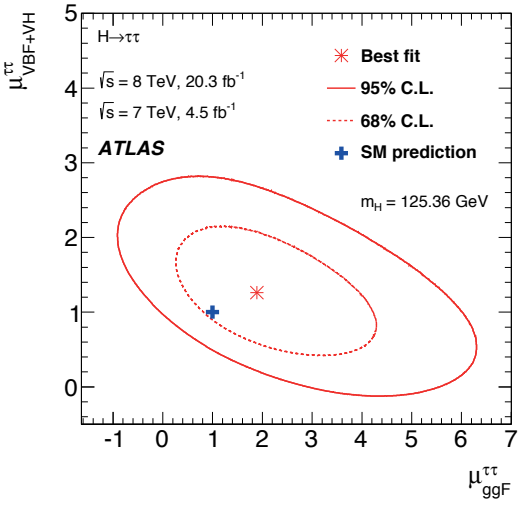


Figure 6.5. The best fit to the data of the signal strengths for the VBF+VH and gluon-gluon fusion production modes, along with its 68 % and 95 % CL contours. The fit uses the mass hypothesis $m_H = 125.63\,\text{GeV}$. The SM prediction ($\mu_{\text{ggF}} = \mu_{\text{VBF}+VH} = 1$) is also shown.

Section 2.3 for details on the charged Higgs boson production and decay modes.

6.3.1 Analysis overview

The fully hadronic mode of the $H^+ \to \tau\nu$ decay, where both the τ-lepton and the top quark decay hadronically, has the greatest branching fraction. This signature consists of a hadronically decaying τ-lepton, large amount of $E_{\mathrm{T}}^{\mathrm{miss}}$ due to the two neutrinos, at least one jet from b-quark decays, and two jets from the hadronic decay of a W boson. An analysis of this mode performed with 13 TeV data corresponding to an integrated luminosity of $3.2\,\mathrm{fb}^{-1}$, collected in 2015, is detailed in Ref. [108]. It is updated with data corresponding to an integrated luminosity of $11.5\,\mathrm{fb}^{-1}$, collected in 2016, in Ref. [109]. This analysis is summarized in the following.

Trigger

The topological-cluster-based trigger with a threshold of $E_{\mathrm{T}}^{\mathrm{miss}} > 70\,\mathrm{GeV}$ is used to select events in data collected in 2015, and the jet-based trigger with a threshold of $E_{\mathrm{T}}^{\mathrm{miss}} > 90\,\mathrm{GeV}$ is used in 2016. The trigger efficiency in the signal region is estimated from data, using the method described in Section 6.3.2.

Event selection

Events are required to have at least one τ_{had} candidate, and the highest-p_{T} candidate must pass medium identification criteria. Three or more jets with $p_{\mathrm{T}} > 25\,\mathrm{GeV}$ are required, of which at least one is b-tagged, and the threshold on the reconstructed $E_{\mathrm{T}}^{\mathrm{miss}}$ is 150 GeV to ensure a high efficiency of the trigger. Events with additional muons or electrons with $p_{\mathrm{T}} > 20\,\mathrm{GeV}$ are vetoed.

Signal-to-background discrimination

The discriminant used is the transverse mass of the τ_{had} candidate and the $E_{\mathrm{T}}^{\mathrm{miss}}$, defined as

$$m_{\mathrm{T}} = \sqrt{2 p_{\mathrm{T}}^{\tau} E_{\mathrm{T}}^{\mathrm{miss}} (1 - \cos\Delta\phi_{\tau,\mathrm{miss}})}. \tag{6.12}$$

An additional requirement of $m_{\mathrm{T}} > 50\,\mathrm{GeV}$ is applied to reject events where the $E_{\mathrm{T}}^{\mathrm{miss}}$ is incorrectly measured, due to the τ_{had} candidate being nearly aligned with the direction of the $E_{\mathrm{T}}^{\mathrm{miss}}$.

Backgrounds

The dominant background arises from event where a jet is misidentified as a hadronically decaying τ-lepton, arising from the $t\bar{t}$ process in the

low-m_{T} region and the multi-jet process in the high-m_{T} region. It is modelled with the fake factor method. Backgrounds with misidentified electrons or muons, and with true hadronically decaying τ-lepton, are modelled with simulated events and validated in control regions.

6.3.2 $E_{\mathrm{T}}^{\mathrm{miss}}$ trigger efficiency measurement

Due to the complexity involved in emulating the $E_{\mathrm{T}}^{\mathrm{miss}}$ trigger, an alternative approach is used to select events in simulated samples. The author has developed a method to measure the trigger efficiency in data, in a control region designed to select mostly events from semi-leptonic $t\bar{t}$ decays. Simulated events are then weighted by the measured trigger efficiency, based on their reconstructed $E_{\mathrm{T}}^{\mathrm{miss}}$.

The control region used to measure the trigger efficiency consists of one electron and one τ_{had} candidate, both passing loose identification criteria, as well as at least two jets with $p_{\mathrm{T}} > 25\,\mathrm{GeV}$, of which at least one is b-tagged. The events are selected with a single-electron trigger with a p_{T}-threshold of 24 GeV. The control region is designed to be similar to the signal region, while the loosened identification criteria ensures good statistical precision.

The trigger efficiency is defined as the inverse ratio between events that pass the event selection (TOT), and those additionally firing the selected $E_{\mathrm{T}}^{\mathrm{miss}}$ trigger (PASS)

$$\varepsilon = \frac{N(\mathrm{PASS})}{N(\mathrm{TOT})}. \tag{6.13}$$

The efficiency is derived in bins of the reconstructed $E_{\mathrm{T}}^{\mathrm{miss}}$, and then fitted to the error function (erf) with the following parametrization

$$F(x) = p_0 \cdot \left[1 + \mathrm{erf}\left(\frac{x - p_1}{p_2}\right)\right] + p_3. \tag{6.14}$$

This fit results in an *efficiency curve*.

The systematic uncertainties on the efficiency curve are estimated by the following variations to the event selection, and the statistical precision of the measurement:

- tightening the electron identification criteria,
- tightening the τ_{had} identification criteria,
- increasing the number of jets from two to three,
- increasing the magnitude of the statistical uncertainties by a factor of four.

The systematic variations are fitted to the error function with the same parametrization as in Eq. (6.14), and are measured as deviations from the nominal efficiency curve. Figure 6.6 shows the trigger efficiency curves, with their systematic uncertainties, measured in 2015 and 2016 data.

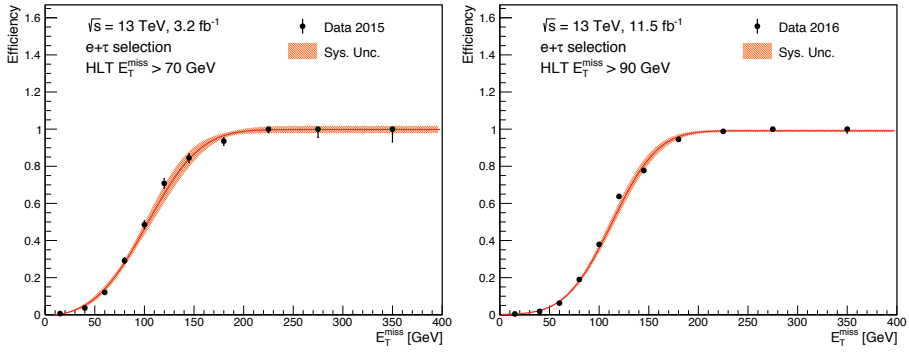


Figure 6.6. Trigger efficiency for the $E_{\mathrm{T}}^{\mathrm{miss}}$ trigger with an $E_{\mathrm{T}}^{\mathrm{miss}}$ threshold of 70 GeV, measured in 2015 data (left), and 90 GeV, measured in 2016 data (right), as a function of the reconstructed $E_{\mathrm{T}}^{\mathrm{miss}}$. The data points represent the measured efficiency, while the curve represents the fit of the data points to the error function. The systematic uncertainty is estimated from variations in the event selection and the statistical precision.

6.3.3 Estimation of misidentified τ-leptons

A fake factor method is used to estimate the background from misidentified τ_{had} candidates. It uses a single set of fake factors, measured in a control region enriched in quark- and gluon-initiated jets, to estimate misidentified τ_{had} candidates from all processes. The fake factors are parametrized by p_{T}, and measured separately for 1- and 3-prong τ_{had} candidates, and for 2015 and 2016 data.

6.3.4 Results

The profile likelihood ratio is used to test the compatibility of the data with the background-only hypothesis. The likelihood uses the m_{T} distribution in the signal region as the discriminating variable. Systematic uncertainties are included in the fit in the form of nuisance parameters. Figure 6.7 shows the distribution of the m_{T} in the signal region, after the fit to the background-only hypothesis.

No deviation from the background-only hypothesis is found, and the data is found to be compatible with the SM. 95 % CL exclusion limits are set on $\sigma(pp \to [b]tH^{+}) \times (H^{+} \to \tau\nu)$, using the CL_s procedure. The observed exclusion limits are 1.8 pb–14 fb in the range 200–2000 GeV. They are shown together with the expected exclusion limits in in Figure 6.8.

These limits are also used to exclude an H^{+} signal in the hMSSM scenario. Figure 6.9 shows the observed and expected exclusion in the $\tan\beta$–$m_{H^{+}}$ plane. At $\tan\beta = 60$, above which no reliable theoretical predictions exist, the H^{+} signal is excluded in the mass range 200–540 GeV.

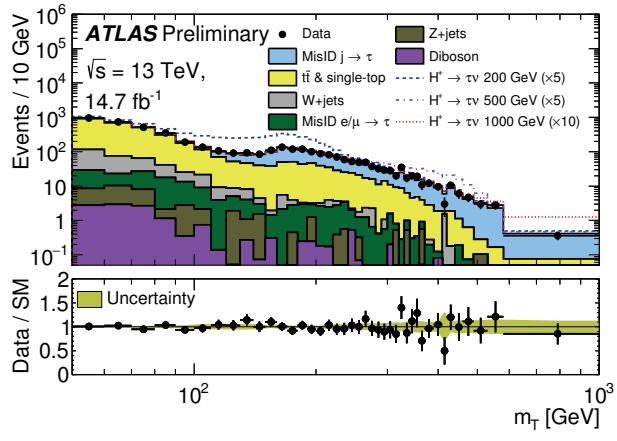


Figure 6.7. Distribution of the m_{T} in the signal region, after the fit to the background-only hypothesis. The signal for three charged Higgs bosons mass hypotheses at $m_{H^+} = 200\,\mathrm{GeV}$, $m_{H^+} = 500\,\mathrm{GeV}$, and $m_{H^+} = 1000\,\mathrm{GeV}$, scaled to 5, 5, and 10 times the cross section, predicted by the hMSSM scenario at $\tan\beta = 60$, respectively, are plotted on top of the background distribution. The uncertainty includes the statistical and systematic components, as obtained from the profile likelihood ratio fit.

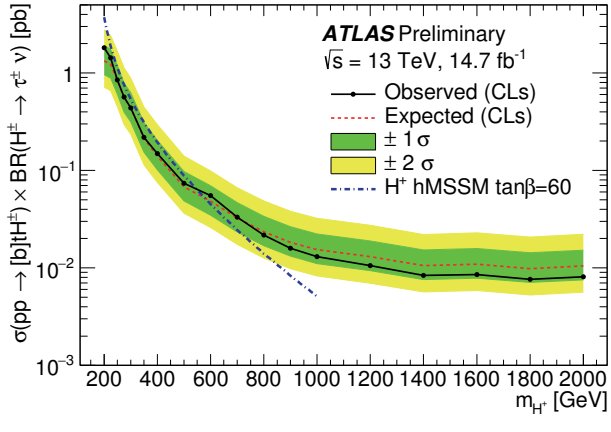


Figure 6.8. Observed and expected 95 % CL exclusion limits as a function of m_{H^+}. The cross section times branching fraction $\sigma(pp \to [b]tH^+) \times (H^+ \to \tau\nu)$, as predicted by the hMSSM scenario at $\tan\beta = 60$, is also shown.

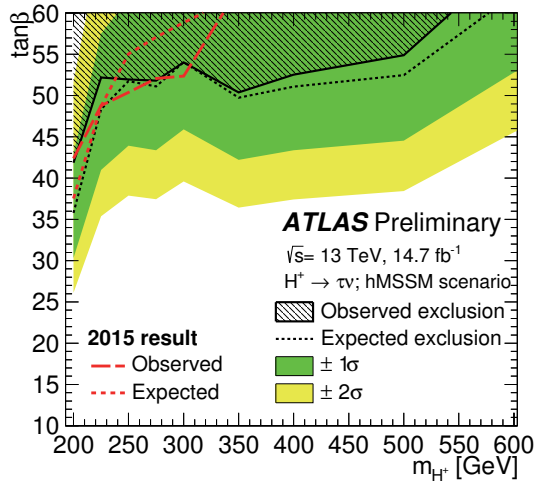


Figure 6.9. Observed and expected 95 % CL exclusion limits on $\tan\beta$, as a function of m_{H^+}, interpreted in the hMSSM scenario. The observed and expected exclusion limits using only data collected in 2015 is also shown.

7. Summary of Papers

Paper I

This paper describes a method to configure machines on the fly using Puppet. The author has used this method to configure virtual machines in Google's IaaS cloud Google Compute Engine. He has demonstrated that this method is a viable alternative to using pre-configured machine images to configure computing nodes for ATLAS analysis.

Paper II

This paper describes the measurement of the Higgs boson coupling to fermions in $H \to \tau\tau$ decays with the complete 7 TeV and 8 TeV datasets. The best-fit signal strength is $\mu = 1.4$, corresponding to an excess over the background-only hypothesis of 4.5σ, providing evidence for Higgs boson decays into a pair of τ-leptons. The author has contributed through validating W+jets samples simulated with ATLFAST-II, implementing calibrations of and recommendations for physics objects, producing end-user analysis samples, performing validation of signal and control regions, and working with data-driven background estimation methods for misidentified hadronic τ decays.

Paper III

This paper describes the commissioning of the reconstruction, identification, and energy scale of hadronically decaying τ-leptons for the 2015 data-taking period. The author has contributed through the matching algorithm that associates a reconstructed τ_{had} with its counterpart in the HLT (trigger matching).

Paper IV

This paper describes the search for charged Higgs bosons in $H^+ \to \tau\nu$ decays using 13 TeV data corresponding to an integrated luminosity of $3.2\,\text{fb}^{-1}$. No excess over the SM background is found, and the

observed 95 % CL exclusion limits on $\sigma(pp \to [b]tH^+) \times (H^+ \to \tau\nu)$ are 1.8 pb–14 fb in the range 200–2000 GeV. The author has contributed by developing a method to measure the trigger efficiency and the associated systematic uncertainties in data, and applying it to simulated events.

Paper V

This paper describes the reconstruction and identification algorithms, as well as the energy scale calibration for hadronically decaying τ-leptons in Run 2 of the LHC. The performance of these algorithms in the event reconstruction and at the HLT in 13 TeV data collected in 2015 is also presented. The paper is entirely written by the author.

Paper VI

This paper presents results from searches for charged Higgs bosons in ATLAS and CMS. The searches cover singly charged Higgs boson decays in the $H^+ \to \tau\nu$, $H^+ \to t\bar{b}$, $H^+ \to c\bar{s}$, and $H^+ \to W^+Z$ modes, as well as for doubly charged Higgs boson decays in the $\Phi^{++}\Phi^{--} \to 4l$ and $\Phi^{++}\Phi^{-} \to 3l$ modes, with 7 TeV and 8 TeV data from the Run 1 of the LHC. The first search for charged Higgs bosons with 13 TeV data in the $H^+ \to \tau\nu$ decay mode with ATLAS is also presented. The results are interpreted in various theoretical models. The paper is entirely written by the author.

Paper VII

This paper describes a search for charged Higgs bosons in $H^+ \to \tau\nu$ decays that is similar to Paper IV, however with 13 TeV data corresponding to an integrated luminosity of 14.7 fb^{-1} collected in 2015 and 2016. The observed 95 % CL exclusion limits on $\sigma(pp \to [b]tH^+) \times (H^+ \to \tau\nu)$ are 2.0 pb–8 fb in the range 200–2000 GeV.

The author has contributed by measuring the trigger efficiency and the associated systematic uncertainties using the method developed for Paper IV, for the two different triggers used for 2015 and 2016 data.

8. Conclusion

> Our revels now are ended. These our actors,
> As I foretold you, were all spirits, and
> Are melted into air, into thin air;
> And, like the baseless fabric of this vision,
> The cloud-capp'd towers, the gorgeous palaces,
> The solemn temples, the great globe itself,
> Yea, all which it inherit, shall dissolve,
> And, like this insubstantial pageant faded,
> Leave not a rack behind. We are such stuff
> As dreams are made on; and our little life
> Is rounded with a sleep.
>
> William Shakespeare
> *The Tempest, Act IV, Scene I*

This thesis focuses on the hadronic decays of τ-leptons and their application to measurements of the SM Higgs boson coupling to fermions, and to searches for charged Higgs bosons as predicted by the MSSM and other 2HDM models.

The SM is a remarkably precise theory of particle physics, which has made many successful predictions including the existence of the Higgs boson. However, it is known to be an incomplete theory, and many extensions exist that attempt to reconcile its shortcomings. SUSY, and in particular the MSSM, is one such theory that also has the appealing property of fixing many of the perceived inelegances of the SM. The MSSM Higgs sector is one example of a 2HDM, a larger class of extensions to the SM Higgs sector that are investigated in their own right.

The organization CERN is home to the largest particle accelerator in the world, the LHC, and it provides pp collisions at 13 TeV to, among others, the ATLAS experiment. At the time of writing, it has delivered collisions corresponding to $31.9\,\text{fb}^{-1}$ in 2016 alone.

The ATLAS experiment is a general-purpose detector built to study the SM, and to search for signatures of extra dimensions, new gauge bosons, additional Higgs bosons, dark matter candidates, and SUSY particles. Together with the CMS experiment, it discovered the Higgs boson in 2012. The ATLAS detector consists of an inner detector that tracks charged particles, a calorimeter system that measures hadronic and electromagnetic energy deposits, a muon spectrometer, and a magnet system providing solenoidal and toroidal magnetic fields.

The τ-lepton is the heaviest of the leptons, and the only one which can decay into hadrons. Hadronic decays of τ-leptons are reconstructed and triggered on by the ATLAS experiment. The efficiency of the τ trigger is measured in $t\bar{t}$ events, as a complement to the standard $Z \to \tau\tau$ measurement, since the p_{T}-spectrum of the τ_{had} candidates is higher.

With their high mass and relatively clean detector signature, τ-leptons offer a good handle on processes involving Higgs bosons. The SM Higgs boson coupling to fermions is measured in $H \to \tau\tau$ decays. The resulting signal strength of $\mu = 1.4$ corresponds to an excess over the background-only hypothesis of 4.5σ, providing evidence for the process. A search is also conducted for the charged Higgs boson in $H^+ \to \tau\nu$ decays. No excess is found over the SM prediction, and the observed 95 % CL exclusion limits on $\sigma(pp \to [b]tH^+) \times (H^+ \to \tau\nu)$ are 2.0 pb–8 fb in the range 200–2000 GeV

9. Sammanfattning på svenska

Lindorm solar sig på sten
Som ett sammet vit och len
Vill i barnets vagga gå
Men det ska han aldrig få
Han ska bli bunden
Uti gröna lunden

Alice Tegnér
Ute blåser sommarvind

Inom elementarpartikelfysiken studeras universums byggstenar, de fundamentala partiklar som utgör all materia, och de krafter som verkar mellan dem. Den teori som sammanfattar elementarpartikelfysiken heter standardmodellen (Figur 2.1). De fundamentala partiklarna består till exempel av upp- och nerkvarkar, som i olika kombinationer utgör protonerna och neutronerna i atomer, samt elektroner. Dessa partiklar utgör all massa[1], men de ger inte en fullständig bild av verkligheten. Både elektronerna och upp- och nerkvarkarna har tyngre släktingar i två generationer. Uppkvarkens släktingar heter charm- och toppkvark, och nerkvarkens sär- och bottenkvark, medan elektronens släktingar heter myon och tau-lepton. Dessa släktingar är instabila och sönderfaller mycket fort.

Kvarkarna reagerar med varandra via en kraft som kallas den starka kärnkraften. Den förmedlas av gluoner som ser till att protonerna och neutronerna sitter ihop, och inte faller sönder i sina beståndsdelar. Det är bara kvarkarna och gluonerna själva som känner av den starka kärnkraften.

Både kvarkarna och de laddade leptonerna bär på elektrisk laddning och påverkas av den elektromagnetiska kraften. Den förmedlas av fotoner och är allorstädes närvarande i vår vardag, där den beskriver ljuset från solen, hur elektroniken i en dator fungerar och många andra saker. Teorin om den elektromagnetiska kraften är en av de mest välstuderade inom fysiken.

Den tredje kraften som beskrivs av standardmodellen heter den svaga kärnkraften, och den orsakar bland annat radioaktiva sönderfall hos atomer. Den förmedlas av vektorbosonerna W och Z, vilka har massa till

[1]Det vill säga all massa som vi kan se. Vi vet ännu inte vad den mörka materian består av, och den utgör en mycket större del av universums totala massa.

skillnad från gluonen och fotonen. Deras existens förutsades av standardmodellen, och deras upptäckt är en av teorins största framgångar. Den svaga kärnkraften påverkar både kvarkar och leptoner.

Elektronen, myonen och tau-leptonen har också varsin väldigt lätt partner som kallas neutrino, och med dessa blir leptonerna lika många till antalet (sex) som kvarkarna. Till skillnad från de laddade leptonerna är neutrinerna elektriskt oladdade, och växelverkar bara via den svaga kärnkraften. Detta får till följd att de inte kan upptäckas i detektorer, utan bara tillkännager sig genom en avsaknad av energi som leder till en obalans i mätningarna[2]. Sammanfattningsvis kallas gruppen av kvarkar, laddade leptoner, och neutriner för fermioner, medan gluonen, fotonen, och vektorbosonerna heter bosoner. Alla partiklar har som regel också en antipartikel[3].

Standardmodellen är uppbyggd kring lagar som följer symmetrier hos de fundamentala partiklarnas egenskaper. Dessa symmetrier kräver att partiklarna saknar massa, vilket förstås är helt i kontrast med vad vi ser omkring oss. För att lösa detta problem infördes den såkallade Higgsmekanismen. Den föreskriver att grundtillståndet[4] inte är energilöst, utan är befäst med en energimängd kallad vakumenergin. Higgsmekanismen förmedlar massa till alla fundamentala partiklar, förutom neutrinerna, fotonen och gluonen som förblir masslösa. Med dess införande i standardmodellen lämnas även rum för ytterligare en boson vid namn Higgsbosonen, och den var den sista partikeln i standardmodellen som upptäcktes.

ATLAS-experimentet är ett internationellt samarbete med cirka 5000 medlemmar från 38 länder. ATLAS-detektorn är installerad i LHC (Large Hadron Collider) vid kärn- och partikelfysiklaboratoriet CERN i Genève, Schweiz. Forskningen i denna avhandling har utförts med data som samlats in av ATLAS-detektorn under åren 2011–2016.

ATLAS-detektorn kan upptäcka spår efter partiklar med hjälp av olika detektortekniker. Den inre delen av detektorn använder sig bland annat av halvledarteknik för att bestämma rörelsemängd hos laddade partiklar, medan kalorimetern är en massiv del av detektorn som har till syfte att samla upp all energi från elektroner, fotoner, och partiklar sammansatta av kvarkar (hadroner), och då framför allt pioner[5]. Den yttre delen av detektorn är specifikt skapad för att bestämma rörelsemängd hos myoner, som har relativt lång livslängd och som knappt växelverkar med kalorimetern. De nämnda partiklarna känns igen genom att de skapar olika mönster i detektorn. Tau-leptonen sönderfaller dock antingen till

[2]Energins och rörelsemängdens bevarande är grundläggande lagar inom fysiken.
[3]Med vissa undantag: Z-bosonen, fotonen, och gluonen är sina egna antipartiklar, medan det fortfarande är oklart hur neutrinernas antipartiklar ser ut.
[4]Grundtillståndet är det lägsta energitillstånd ett system kan ha.
[5]Pioner är ett samlingsnamn för elektriskt laddade och oladdade par av en upp- eller nerkvark, och en av deras antipartiklar

en elektron eller en myon och en neutrino, eller till hadroner innan de kommer fram till detektorn. De kan enbart identifieras via det senare sönderfallet.

Den här avhandlingen beskriver hadroniska sönderfall av tau-leptoner, hur de kan återskapas och identifieras, och även hur de kan användas för att välja ut händelser som är intressanta nog att spara med hjälp av ”tau-triggern”[6]. En mätning av ”tau-triggerns” effektivitet med avseende på energin hos tau-leptonens sönderfallsprodukter i händelser som till största delen består av par av topp- och antitoppkvarkar återges i avhandlingen.

ATLAS-experimentet upptäckte tillsammans med CMS-experimentet (också vid LHC) den saknade Higgsbosonen 2012, och gjorde därmed standardmodellen komplett. Elementarpartikelfysik som ämne är dock inte begränsat till att bara göra nya upptäckter, utan minst lika viktigt är att granska de upptäckta partiklarna och bestämma deras egenskaper. Vissa av dessa ges av symmetrierna i teorin, medan andra måste bestämmas på experimentell väg. Kopplingarna mellan Higgsbosonen och andra partiklar är exempel på sådana egenskaper.

En del av forskningen i den här avhandlingen består i att bestämma kopplingen mellan Higgsbosonen och tau-leptonen. Anledningen till att man väljer just tau-leptonen för denna mätning är för att den har hög massa, och Higgsbosonen sönderfaller helst till sådana partiklar. Vad beträffar kopplingen till fermioner överlag så är antalet Higgsbosoner som sönderfaller till två bottenkvarkar mycket högre, men dessa händelser är svårare att skilja ut från händelser som inte kommer från sönderfall av Higgsbosonen (så kallade bakgrundshändelser). Författaren har deltagit i forskningen för att bestämma Higgsbosonens koppling till tau-leptonen framför allt genom att på olika sätt beskriva bakgrundshändelser, så att sönderfall från Higgsbosonen kan urskiljas mot dessa.

Standardmodellen är trots sina stora framgångar inte en komplett teori över verkligheten. Den innehåller till exempel inte en beskrivning av gravitationen, som ju är en högst påtaglig kraft i vardagen. Den förklarar inte heller varför neutrinerna har massa, vad mörk matera består av, eller vad mörk energi är. Även i sig själv har den vissa egenskaper som kan betraktas som oeleganta, som exemplevis den stora skillnaden i massa mellan generationerna[7]. Det finns många förslag på hur man kan utöka standardmodellen till en större teori, där några av dessa problem får en naturlig lösning. En sådan utökning är teorin om supersymmetri, där varje partikel i standardmodellen har en superpartner av motsatt typ. För varje fermion i standardmodellen, finns en boson, och för varje boson en

[6]En väldigt stor del av händelserna i detektorn är ointressanta ur forskningssynpunkt. På grund av begränsningar i hur snabbt man kan läsa ut händelser ur detektorn och hur mycket data man har möjlighet att spara väljer man att använda en så kallad ”trigger” för att välja ut händelser som vid en första anblick verkar vara intressanta.
[7]Till exempel är tau-leptonen cirka 3500 gånger tyngre än elektronen.

fermion. En effekt av den minst invecklade supersymmetriska modellen är att det krävs ytterligare fyra Higgsbosoner för att generera massa till alla partiklar. Två av dessa har ingen elektrisk laddning, medan två är laddade. Även andra teorier utökar standardmodellen med fler Higgsbosoner, och att söka efter dessa och andra påtänkta partiklar är ett aktivt forskningsområde inom ATLAS-experimentet.

Författaren har deltagit i två eftersökningar efter laddade Higgsbosoner, där den första gjordes med data från 2015, vilken senare utökades med en mycket större datamängd från 2016. Dessa eftersökningar har skett i sönderfall till en tau-lepton och en neutrino, där neutrinon ger upphov till en stor avsaknad av energi. Denna avsaknad används som en ”trigger”, och författaren har mätt hur effektiv den är på att välja ut händelser. Resultaten visar inga tecken på att en laddad Higgsboson skulle existera, men också att det inte är ett slutgiltigt resultat, utan att det är värt att fortsätta eftersökningen med ännu mer data i framtiden.

Sammanfattningsvis har ATLAS-experimentet hjälpt oss att lägga den sista pusselbiten i standardmodellen, vilket är att betrakta som ett stor framgång för elementarpartikelfysiken. Men denna upptäckt är bara ett skrapande på ytan av den stora potential som LHC och ATLAS-experimentet besitter. LHC har under 2016 levererat mer data än under 2011, 2012 och 2015 tillsammans, och det finns en näst intill oändlig mängd nya teorier att testa, och många föreslagna nya partiklar att leta efter.

10. Acknowledgements

During my graduate studies, and during the writing of this thesis I have experienced unwavering support from both supervisors and family, something for which I will be eternally grateful. I would like to thank Arnaud Ferrari, who throughout the writing of this thesis has not only corrected my mistakes, but also provided editorial guidance which has improved the quality of the text by orders of magnitude. He has supervised my studies with the perfect balance between guidance, coercing, and freedom under responsibility. I also want to express my gratitude to Camila Rangel Smith, who, although only actively supervising me for about a year, helped me develop the mindset required of a particle physicist. I want to thank Elias Coniavitis who guided me through the first years of my studies and the crazy years of Higgs boson decays to τ-leptons analysis. I sometimes regret that we didn't have more time to discuss actual physics or other things, rather than worrying about the next common ntuple-production or fake-τ estimation. Finally, I'd like to thank Mattias, the ever-present authority of all things Grid-related, for correcting typographical errors and other mistakes in my thesis.

Other colleagues in our group and in the department have also made deep impressions, and instilled me with wisdom or given me fond memories. Thanks to Tord Ekelöf for all the inspiration, and for the best swordfish I've ever tasted. Thanks to Richard for giving expert advice on everything from details on analyses, to strategical career choices. I believe the Uppsala ATLAS group will continue to prosper in his able hands. Thanks also to Charlie Isaksson, Daniel Pelikan, and Alexander Madsen for all the help and friendly discussions during the first years of my studies. I would particularly like to thank my closest colleagues, Mikael Mårtensson, Max Isacson, and Joakim Gradin, for being friendly, funny, helpful, and professional. We've built detectors, studied machine learning, attended conferences, and thrown barbeques together, and I'm very sad that I will soon have to leave you. You are awesome. Thanks also to everyone participating in the lunchroom discussions.

Some people outside of Uppsala University deserve special mention. First of all, although I doubt he will get the chance to read this, I would like to thank my senior high school teacher in physics Krister Sjöberg. It was his words that first got me started on this path. I would like to thank Martin Flechl for providing me with a master's thesis project which eventually got me back into physics. I still don't regret it. I would

like to thank Justin Griffiths and Michael Pitt for the collaboration on the charged Higgs boson searches, Matthew Beckingham, Daniele Zanzi, and Quentin Buat for supporting me in the $t\bar{t}$ τ trigger tag-and-probe analysis, as well as Carl Jeske and Jacob Howard with whom I worked closely in the Higgs boson to two τ-leptons analysis.

I would like to thank my parents Bo and Ann-Charlott for all the emotional and financial support during the years, for granting me the freedom to do whatever I wanted with my life, and for baby-sitting Alexandra. Thanks also to aunt Anita and uncle Olle for lodgning and daily feasts during the busiest period of my thesis writing, and to my mother-in-law Cecila for lots and lots of baby-sitting. Thanks to my dear friends Gustaf and Disa, Lars, and Ingemar and Liza, who on occasion have housed and fed me during my Uppsala visits.

Words can never convey the gratitude I feel towards Louise for all the times she's taken care of home and children while I've been away, for all the encouragement she's given when I've been struck with imposter syndrome, and for always giving me good advice in difficult situations. I could not have done this without you. I love you.

References

[1] S. L. Glashow, *Partial Symmetries of Weak Interactions*, Nucl. Phys. **22** (1961) 579.

[2] S. Weinberg, *A Model of Leptons*, Phys. Rev. Lett. **19** (1967) 1264.

[3] A. Salam, *Weak and Electromagnetic Interactions*, Proceedings of the 8th Nobel symposium, Ed. N. Svartholm, Almqvist & Wiskell, 1968, Conf. Proc. **C680519** (1968) 367.

[4] G. 't Hooft and M. J. G. Veltman, *Regularization and Renormalization of Gauge Fields*, Nucl. Phys. **B44** (1972) 189.

[5] ATLAS Collaboration, *Observation of a new particle in the search for the Standard Model Higgs boson with the ATLAS detector at the LHC*, Phys. Lett. B **716** (2012) 1, arXiv: `1207.7214 [hep-ex]`.

[6] CMS Collaboration, *Observation of a new boson at a mass of 125 GeV with the CMS experiment at the LHC*, Phys. Lett. B **716** (2012) 30, arXiv: `1207.7235 [hep-ex]`.

[7] K. A. Olive et al., *Review of Particle Physics*, Chin. Phys. **C38** (2014) 090001.

[8] E. Noether, *Invariante Variationsprobleme*, Nachr. v. d. Ges. d. Wiss. zu Gottingen (1918) 235.

[9] F. Englert and R. Brout, *Broken symmetry and the mass of gauge vector mesons*, Phys. Rev. Lett. **13** (1964) 321.

[10] P. W. Higgs, *Broken symmetries, massless particles and gauge fields*, Phys. Lett. **12** (1964) 132.

[11] P. W. Higgs, *Broken symmetries and the masses of gauge bosons*, Phys. Rev. Lett. **13** (1964) 508.

[12] G. Guralnik, C. Hagen, and T. Kibble, *Global conservation laws and massless particles*, Phys. Rev. Lett. **13** (1964) 585.

[13] P. W. Higgs,
Spontaneous symmetry breakdown without massless bosons,
Phys. Rev. **145** (1966) 1156.

[14] T. Kibble, *Symmetry breaking in non-Abelian gauge theories*,
Phys. Rev. **155** (1967) 1554.

[15] MuLan Collaboration,
Measurement of the Positive Muon Lifetime and Determination of the Fermi Constant to Part-per-Million Precision,
Phys. Rev. Lett. **106** (4 2011) 041803.

[16] Y. Nambu and G. Jona-Lasinio, *Dynamical Model of Elementary Particles Based on an Analogy with Superconductivity. I*,
Phys. Rev. **122** (1961) 345.

[17] Y. Nambu and G. Jona-Lasinio, *Dynamical Model of Elementary Particles Based on an Analogy with Superconductivity. II*,
Phys. Rev. **124** (1961) 246.

[18] LHC Higgs Cross Section Working Group et al.,
Handbook of LHC Higgs Cross Sections: 3. Higgs Properties,
CERN-2013-004 (CERN, Geneva, 2013),
arXiv: 1307.1347 [hep-ph].

[19] Y. Fukuda et al., *Measurements of the solar neutrino flux from Super-Kamiokande's first 300 days*, Phys. Rev. Lett. **81** (1998) 1158, [Erratum: Phys. Rev. Lett.81,4279(1998)],
arXiv: hep-ex/9805021 [hep-ex].

[20] J. F. Gunion et al., *The Higgs hunter's guide*, vol. 80,
Brookhaven Nat. Lab., 1989.

[21] E. A. Paschos, *Diagonal Neutral Currents*,
Phys. Rev. **D15** (1977) 1966.

[22] S. L. Glashow and S. Weinberg,
Natural Conservation Laws for Neutral Currents,
Phys. Rev. **D15** (1977) 1958.

[23] S. Heinemeyer, W. Hollik, and G. Weiglein,
Constraints on tan Beta in the MSSM from the upper bound on the mass of the lightest Higgs boson, JHEP **06** (2000) 009,
arXiv: hep-ph/9909540 [hep-ph].

[24] M. Carena et al., *MSSM Higgs Boson Searches at the LHC: Benchmark Scenarios after the Discovery of a Higgs-like Particle*,
Eur. Phys. J. **C73** (2013) 2552, arXiv: 1302.7033 [hep-ph].

[25] A. Djouadi et al.,
The post-Higgs MSSM scenario: Habemus MSSM?,
Eur. Phys. J. **C73** (2013) 2650, arXiv: 1307.5205 [hep-ph].

[26] A. Djouadi et al.,
Fully covering the MSSM Higgs sector at the LHC,
JHEP **06** (2015) 168, arXiv: 1502.05653 [hep-ph].

[27] E. Bagnaschi et al.,
Benchmark scenarios for low $\tan\beta$ *in the MSSM*,
LHCHXSWG-2015-002, 2015,
URL: https://cdsweb.cern.ch/record/2039911.

[28] R. Harlander, M. Krämer, and M. Schumacher,
Bottom-quark associated Higgs-boson production: Reconciling the four- and five-flavour scheme approach, (2011),
arXiv: 1112.3478 [hep-ph].

[29] ATLAS Collaboration, *Search for a light charged Higgs boson in the decay channel* $H^+ \to c\bar{s}$ *in* $t\bar{t}$ *events using pp collisions at* $\sqrt{s} = 7$ *TeV with the ATLAS detector*,
Eur. Phys. J. C **73** (2013) 2465, arXiv: 1302.3694 [hep-ex].

[30] CMS Collaboration, *Search for a light charged Higgs boson decaying to* $c\bar{s}$ *in pp collisions at* $\sqrt{s} = 8$ *TeV*,
JHEP **12** (2015) 178, arXiv: 1510.04252 [hep-ex].

[31] ATLAS Collaboration, *Search for charged Higgs bosons decaying via* $H^\pm \to \tau^\pm\nu$ *in fully hadronic final states using pp collision data at* $\sqrt{s} = 8$ *TeV with the ATLAS detector*,
JHEP **03** (2015) 088, arXiv: 1412.6663 [hep-ex].

[32] CMS Collaboration,
Search for a charged Higgs boson in pp collisions at $\sqrt{s} = 8$ *TeV*,
JHEP **11** (2015) 018, arXiv: 1508.07774 [hep-ex].

[33] ATLAS Collaboration,
Search for charged Higgs bosons in the $H^\pm \to tb$ *decay channel in pp collisions at* $\sqrt{s} = 8$ *TeV using the ATLAS detector*,
JHEP **03** (2016) 127, arXiv: 1512.03704 [hep-ex].

[34] G. Arnison et al.,
Experimental observation of isolated large transverse energy electrons with associated missing energy at s=540 GeV,
Physics Letters B **122** (1983) 103.

[35] M. Banner et al., *Observation of single isolated electrons of high transverse momentum in events with missing transverse energy at the CERN pp collider*, Physics Letters B **122** (1983) 476.

[36] G. Arnison et al., *Experimental observation of lepton pairs of invariant mass around 95 GeV/*c^2 *at the CERN SPS collider*,
Physics Letters B **126** (1983) 398.

[37] P. Bagnaia et al.,
Evidence for $Z^0 \to e^+e^-$ at the CERN pp collider,
Physics Letters B **129** (1983) 130.

[38] G. Altarelli, T. Sjöstrand, and F. Zwirner,
Physics at LEP2: Vol. 1, (1996).

[39] G. Altarelli, T. Sjöstrand, and F. Zwirner,
Physics at LEP2: Vol. 2, (1996).

[40] D. DeCamp et al.,
Determination of the number of light neutrino species,
Physics Letters B **231** (1989) 519.

[41] L. Evans and P. Bryant, *LHC Machine*, JINST **3** (2008) S08001.

[42] ATLAS Collaboration,
The ATLAS Experiment at the CERN Large Hadron Collider,
JINST **3** (2008) S08003.

[43] CMS Collaboration, *The CMS experiment at the CERN LHC*,
JINST **3** (2008) S08004.

[44] ATLAS and CMS Collaborations,
Combined Measurement of the Higgs Boson Mass in pp Collisions at $\sqrt{s} = 7$ and 8 TeV with the ATLAS and CMS Experiments,
Phys. Rev. Lett. **114** (2015) 191803,
arXiv: `1503.07589 [hep-ex]`.

[45] K. Aamodt et al., *The ALICE experiment at the CERN LHC*,
JINST **3** (2008) S08002.

[46] H. Bohr and H. Nielsen,
Hadron production from a boiling quark soup,
Nuclear Physics B **128** (1977) 275.

[47] A. A. Alves Jr. et al., *The LHCb Detector at the LHC*,
JINST **3** (2008) S08005.

[48] G. Anelli et al.,
The TOTEM experiment at the CERN Large Hadron Collider,
JINST **3** (2008) S08007.

[49] O. Adriani et al.,
The LHCf detector at the CERN Large Hadron Collider,
JINST **3** (2008) S08006.

[50] B. Acharya et al., *The Physics Programme Of The MoEDAL Experiment At The LHC*, Int. J. Mod. Phys. **A29** (2014) 1430050,
arXiv: `1405.7662 [hep-ph]`.

[51] F. Bradamante, *The COMPASS experiment at CERN*,
Nucl. Phys. **A622** (1997) 50C.

[52] N. Abgrall et al., *NA61/SHINE facility at the CERN SPS: beams and detector system*, JINST **9** (2014) P06005, arXiv: 1401.4699 [physics.ins-det].

[53] V. Fanti et al., *The beam and detector for the NA48 neutral kaon CP violation experiment at CERN*, Nucl. Instrum. Meth. **A574** (2007) 433.

[54] B. Adeva et al., *DIRAC: A High resolution spectrometer for pionium detection*, Nucl. Instrum. Meth. **A515** (2003) 467, arXiv: hep-ex/0305022 [hep-ex].

[55] M. Hori and J. Walz, *Physics at CERN's Antiproton Decelerator*, Prog. Part. Nucl. Phys. **72** (2013) 206, arXiv: 1304.3721 [physics.atom-ph].

[56] E. Kugler, *The ISOLDE facility*, Hyperfine Interactions **129** (2000) 23.

[57] J. Kirkby et al., *Role of sulphuric acid, ammonia and galactic cosmic rays in atmospheric aerosol nucleation*, Nature **476** (2011) 429.

[58] K. Zioutas et al., *A Decommissioned LHC model magnet as an axion telescope*, Nucl. Instrum. Meth. **A425** (1999) 480, arXiv: astro-ph/9801176 [astro-ph].

[59] ATLAS Collaboration, *Performance of the ATLAS Trigger System in 2015*, ATLAS-TRIG-2016-01-001, 2016, URL: https://cdsweb.cern.ch/record/2202371.

[60] ATLAS Collaboration, *Early Inner Detector Tracking Performance in the 2015 Data at $\sqrt{s} = 13$ TeV*, ATL-PHYS-PUB-2015-051, 2015, URL: http://cdsweb.cern.ch/record/2110140.

[61] ATLAS Collaboration, *Vertex Reconstruction Performance of the ATLAS Detector at $\sqrt{s} = 13$ TeV*, ATL-PHYS-PUB-2015-026, 2015, URL: http://cdsweb.cern.ch/record/2037717.

[62] M. Capeans et al., *ATLAS Insertable B-Layer Technical Design Report*, CERN-LHCC-2010-013, 2010, URL: https://cdsweb.cern.ch/record/1291633.

[63] ATLAS Collaboration, *ATLAS Insertable B-Layer Technical Design Report Addendum*, CERN-LHCC-2012-009, 2012, URL: https://cdsweb.cern.ch/record/1451888.

[64] ATLAS Collaboration, *Electron efficiency measurements with the ATLAS detector using the 2015 LHC proton-proton collision data*, ATLAS-CONF-2016-024, 2016, URL: https://cdsweb.cern.ch/record/2157687.

[65] W. Lampl et al., *Calorimeter Clustering Algorithms: Description and Performance*, ATL-LARG-PUB-2008-002, 2008, URL: http://cds.cern.ch/record/1099735.

[66] T. G. Cornelissen et al., *The global χ^2 track fitter in ATLAS*, Journal of Physics: Conference Series **119** (2008) 032013, URL: http://stacks.iop.org/1742-6596/119/i=3/a=032013.

[67] ATLAS Collaboration, *Improved electron reconstruction in ATLAS using the Gaussian Sum Filter-based model for bremsstrahlung*, ATLAS-CONF-2012-047, 2012, URL: http://cdsweb.cern.ch/record/1449796.

[68] ATLAS Collaboration, *Electron and photon energy calibration with the ATLAS detector using LHC Run 1 data*, Eur. Phys. J. C **74** (2014) 3071, arXiv: 1407.5063 [hep-ex].

[69] ATLAS Collaboration, *Measurement of the photon identification efficiencies with the ATLAS detector using LHC Run-1 data*, (2016), arXiv: 1606.01813 [hep-ex].

[70] ATLAS Collaboration, *Muon reconstruction performance of the ATLAS detector in proton–proton collision data at $\sqrt{s} = 13$ TeV*, (2016), arXiv: 1603.05598 [hep-ex].

[71] ATLAS Collaboration, *Properties of jets and inputs to jet reconstruction and calibration with the ATLAS detector using proton–proton collisions at $\sqrt{s} = 13$ TeV*, ATL-PHYS-PUB-2015-036, 2015, URL: http://cdsweb.cern.ch/record/2044564.

[72] M. Cacciari, G. P. Salam, and G. Soyez, *The anti-k_t jet clustering algorithm*, JHEP **04** (2008) 063, arXiv: 0802.1189 [hep-ph].

[73] ATLAS Collaboration, *Jet Calibration and Systematic Uncertainties for Jets Reconstructed in the ATLAS Detector at $\sqrt{s} = 13$ TeV*, ATL-PHYS-PUB-2015-015, 2015, URL: https://cds.cern.ch/record/2037613.

[74] ATLAS Collaboration,
Tagging and suppression of pileup jets with the ATLAS detector,
ATLAS-CONF-2014-018, 2014,
URL: http://cdsweb.cern.ch/record/1700870.

[75] ATLAS Collaboration, *Expected performance of the ATLAS b-tagging algorithms in Run-2*, ATL-PHYS-PUB-2015-022, 2015,
URL: http://cdsweb.cern.ch/record/2037697.

[76] ATLAS Collaboration, *Optimisation of the ATLAS b-tagging performance for the 2016 LHC Run*, ATL-PHYS-PUB-2016-012, 2016, URL: https://cdsweb.cern.ch/record/2160731.

[77] A. Elagin et al., *A new mass reconstruction technique for resonances decaying to $\tau\tau$*,
Nucl. Instrum. Meth. **A654** (2011) 481.

[78] ATLAS Collaboration, *Performance of missing transverse momentum reconstruction with the ATLAS detector in the first proton–proton collisions at $\sqrt{s} = 13$ TeV*,
ATL-PHYS-PUB-2015-027, 2015,
URL: http://cdsweb.cern.ch/record/2037904.

[79] ATLAS Collaboration,
Expected performance of missing transverse momentum reconstruction for the ATLAS detector at $\sqrt{s} = 13$ TeV,
ATL-PHYS-PUB-2015-023, 2015,
URL: http://cdsweb.cern.ch/record/2037700.

[80] ATLAS Collaboration, *Pile-up Correction in Missing Transverse Momentum Reconstruction in the ATLAS Experiment in Proton–Proton Collisions at $\sqrt{s} = 8$ TeV*,
ATLAS-CONF-2014-019, 2014,
URL: http://cdsweb.cern.ch/record/1702055.

[81] ATLAS Collaboration,
Performance of the ATLAS Trigger System in 2010,
Eur. Phys. J. C **72** (2012) 1849, arXiv: 1110.1530 [hep-ex].

[82] E. F. Eisenhandler,
ATLAS Level-1 Calorimeter Trigger Algorithms,
ATL-DAQ-2004-011, 2004,
URL: https://cdsweb.cern.ch/record/792528.

[83] ATLAS Collaboration, *Identification and energy calibration of hadronically decaying tau leptons with the ATLAS experiment in pp collisions at $\sqrt{s} = 8$ TeV*, Eur. Phys. J. C **75** (2015) 303,
arXiv: 1412.7086 [hep-ex].

[84] I. Bird et al., *Update of the Computing Models of the WLCG and the LHC Experiments*, CERN-LHCC-2014-014, 2014, URL: https://cdsweb.cern.ch/record/1695401.

[85] WLCG, *Tier centres*, 2016, URL: http://wlcg-public.web.cern.ch/tier-centres (visited on 08/11/2016).

[86] S. Frixione, P. Nason, and G. Ridolfi, *A Positive-weight next-to-leading-order Monte Carlo for heavy flavour hadroproduction*, JHEP **09** (2007) 126, arXiv: 0707.3088 [hep-ph].

[87] S. Alioli et al., *A general framework for implementing NLO calculations in shower Monte Carlo programs: the POWHEG BOX*, JHEP **1006** (2010) 043, arXiv: 1002.2581 [hep-ph].

[88] T. Sjöstrand, S. Mrenna, and P. Z. Skands, *PYTHIA 6.4 Physics and Manual*, JHEP **0605** (2006) 026, arXiv: hep-ph/0603175.

[89] T. Sjöstrand, S. Mrenna, and P. Z. Skands, *A Brief Introduction to PYTHIA 8.1*, Comput. Phys. Commun. **178** (2008) 852, arXiv: 0710.3820 [hep-ph].

[90] M. L. Mangano et al., *ALPGEN, a generator for hard multiparton processes in hadronic collisions*, JHEP **07** (2003) 001, arXiv: hep-ph/0206293 [hep-ph].

[91] J. Alwall et al., *The automated computation of tree-level and next-to-leading order differential cross sections, and their matching to parton shower simulations*, JHEP **1407** (2014) 079, arXiv: 1405.0301 [hep-ph].

[92] S. Agostinelli et al., *GEANT4: A simulation toolkit*, Nucl. Instrum. Meth. **A506** (2003) 250.

[93] ATLAS Collaboration, *Performance of the Fast ATLAS Tracking Simulation (FATRAS) and the ATLAS Fast Calorimeter Simulation (FastCaloSim) with single particles*, ATL-SOFT-PUB-2014-01, 2014, URL: http://cdsweb.cern.ch/record/1669341.

[94] R. Brun and F. Rademakers, *ROOT: An object oriented data analysis framework*, Nucl. Instrum. Meth. **A389** (1997) 81.

[95] P. Nilsson et al., *Extending ATLAS Computing to Commercial Clouds and Supercomputers*, PoS **ISGC2014** (2014) 034.

[96] H. Öhman, S. Panitkin, and V. Hendrix,
Using Puppet to contextualize computing resources for ATLAS analysis on Google Compute Engine,
J. Phys. Conf. Ser. **513** (2014) 032073.

[97] ATLAS Collaboration, *Reconstruction, Energy Calibration, and Identification of Hadronically Decaying Tau Leptons in the ATLAS Experiment for Run-2 of the LHC*,
ATL-PHYS-PUB-2015-045, 2015,
URL: `https://cds.cern.ch/record/2064383`.

[98] ATLAS Collaboration, *Jet energy measurement with the ATLAS detector in proton–proton collisions at* $\sqrt{s} = 7$ *TeV*,
Eur. Phys. J. C **73** (2013) 2304, arXiv: `1112.6426 [hep-ex]`.

[99] L. Breiman et al., *Classification and Regression Trees*,
Chapman & Hall, New York, 1984.

[100] Y. Freund and R. E. Schapire,
A Decision-Theoretic Generalization of On-Line Learning and an Application to Boosting,
Journal of Computer and System Sciences **55** (1997) 119.

[101] ATLAS Collaboration, *Evidence for the Higgs-boson Yukawa coupling to tau leptons with the ATLAS detector*,
JHEP **04** (2015) 117, arXiv: `1501.04943 [hep-ex]`.

[102] ATLAS Collaboration, *Measurement of the* $t\bar{t}$ *production cross-section using* $e\mu$ *events with b-tagged jets in pp collisions at* $\sqrt{s}$*=13 TeV with the ATLAS detector*, (2016),
arXiv: `1606.02699 [hep-ex]`.

[103] G. Cowan et al.,
Asymptotic formulae for likelihood-based tests of new physics,
Eur. Phys. J. **C71** (2011) 1554,
arXiv: `1007.1727 [physics.data-an]`.

[104] A. L. Read, *Presentation of search results: The CL(s) technique*,
J. Phys. **G28** (2002) 2693.

[105] T. Junk, *Confidence level computation for combining searches with small statistics*, Nucl. Instrum. Meth. **A434** (1999) 435,
arXiv: `hep-ex/9902006 [hep-ex]`.

[106] ATLAS Collaboration,
Measurement of the Higgs boson mass from the $H \to \gamma\gamma$ *and* $H \to ZZ^* \to 4\ell$ *channels in pp collisions at center-of-mass energies of* 7 *and* 8 *TeV with the ATLAS detector*,
Phys. Rev. D **90** (2014) 052004, arXiv: `1406.3827 [hep-ex]`.

[107] ATLAS Collaboration,
Search for charged Higgs bosons in the $H^{\pm} \to tb$ decay channel in pp collisions at $\sqrt{s} = 13$ TeV using the ATLAS detector,
ATLAS-CONF-2016-089, 2016,
URL: https://cdsweb.cern.ch/record/2206809.

[108] ATLAS Collaboration,
Search for charged Higgs bosons produced in association with a top quark and decaying via $H^{\pm} \to \tau\nu$ using pp collision data recorded at $\sqrt{s} = 13$ TeV by the ATLAS detector,
Phys. Lett. B **759** (2016) 555, arXiv: 1603.09203 [hep-ex].

[109] ATLAS Collaboration, *Search for charged Higgs bosons in the τ+jets final state using 14.7 fb^{-1} of pp collision data recorded at $\sqrt{s} = 13$ TeV with the ATLAS experiment*,
ATLAS-CONF-2016-088, 2016,
URL: https://cdsweb.cern.ch/record/2206282.

Acta Universitatis Upsaliensis

Digital Comprehensive Summaries of Uppsala Dissertations from the Faculty of Science and Technology 1434

Editor: The Dean of the Faculty of Science and Technology

A doctoral dissertation from the Faculty of Science and Technology, Uppsala University, is usually a summary of a number of papers. A few copies of the complete dissertation are kept at major Swedish research libraries, while the summary alone is distributed internationally through the series Digital Comprehensive Summaries of Uppsala Dissertations from the Faculty of Science and Technology. (Prior to January, 2005, the series was published under the title "Comprehensive Summaries of Uppsala Dissertations from the Faculty of Science and Technology".)

Distribution: publications.uu.se
urn:nbn:se:uu:diva-304291



ACTA
UNIVERSITATIS
UPSALIENSIS
UPPSALA
2016